Photoreactive Polyorganosiloxane Nanoparticles and the Fabrication of Photocleavable Microcapsules

Dissertation

Zur Erlangung des Grades
"Doktor der Naturwissenschaften"

Am Fachbereich Chemie, Pharmazie und Geowissenschaften
der Johannes Gutenberg-Universität Mainz

Xiaofeng Yuan

geb. in Hunan, P. R. China

Mainz 2005

Die vorliegend Arbeit wurde in der Zeit vom:
August 2002 bis zum Juli 2005
am Institut für Physikalische Chemie
der Johannes Gutenberg-Universität Mainz
angefertigt.

Dekan: Prof. Dr. Peter Langguth

Tag der mündlichen Prüfung: 14 July 2005

CONTENTS

1 INTRODUCTION

Nanoscale science and engineering will lead to better understanding of nature and significant changes in industrial manufacturing, the economy, healthcare, and environmental management and sustainability. In the field of nanoscience, the design, synthesis, and characterization of surface-modified colloidal nanoparticles are of fundamental importance in controlling the mesoscopic properties of new materials and in developing new tools for nanofabrication. In addition to the interesting properties and application of colloidal nanoparticles itself, nanoparticles also become an important building block in nano- and micro-technology.

1.1 Colloids

The term colloid means "glue" in Greek, it was first introduced in 1861 by Thomas Graham to describe the "pseudosolutions" in aqueous systems of silver chloride, sulfur, and Iron(III)-hexacyanoferrate(II) (Prussian blue) which were prepared by Francesco Selmi in the mid-nineteenth century. [1, 2]

1.1.1 Characteristics of colloidal dispersions

Colloidal dispersions are composite systems consisting of a molecular fluid and particles of much larger size that are dispersed in it. The size of the colloidal particles is typically in the range between 1 nm and 1 µ m. The lower size limit stems from the requirement that the colloids are significantly larger than the solvent molecules, and the upper limit ensures that the Brownian motion of the colloidal particles is not dominated by external effects such as sedimentation under gravity. The substances in colloidal systems are usually classified as the dispersed phase and the dispersion medium (or continuous phase), respectively, and can be a solid, a liquid, or a gas. Such combinations together with large surface areas associated with the characteristic size of colloidal particles give rise to a large variety of systems, practical applications and interfacial phenomena. Table 1-1 lists the various types of colloidal systems with common examples of each.

Table 1-1 The various types of colloidal dispersions with some common examples. [3]

Disperse phase	Dispersion medium	Notation	Technical name	Examples
Solid	Gas	S/G	Aerosol	Smoke
Liquid	Gas	L/G	Aerosol	Hairspray, mist, fog
Solid	Liquid	S/L	Sol or dispersion	Printing ink, paint
Liquid	Liquid	L/L	Emulsion	Milk, Mayonnaise
Gas	Liquid	G/L	Foam	Fire-extinguisher foam
Solid	Solid	S/S	Solid dispersion	Ruby glass (Au in glass); some alloys
Liquid	Solid	L/S	Solid emulsion	Bituminous road paving; ice cream
Gas	Solid	G/S	Solid foam	Insulating foam

Classical chemistry and physics use relatively small molecules with a molecular weight up to 10000 g/mol. Polymer and colloid chemistry are using molecules with a molecular weight at least three orders of magnitude higher. On the other hand, solid state physics is interested in the properties of condensed matter. Between these two scientific areas lies the world of colloid chemistry (figure 1-1). Colloid chemistry is therefore closing the gap between molecular chemistry and solid state properties. Colloid chemists may use six orders of magnitude of molecular weight exclusively, including all the corresponding effects. Some people name this region as "mesoscopic", since the colloidal region is located in between well studied scientific length scales. Figure 1-1 "shows a whole scientific research program". The special properties and possibilities of using colloids depend on their position in between large molecules and small solids. For example, large surface areas are associated with the characteristic size of colloidal particles. It is an intrinsic property of all colloidal systems. For instance, a typical micellar solution containing 0.1M amphiphile has ca. 40000 sqr-meters of interfacial area per liter solution. This is another property that distinguishes all colloidal dispersions, the extremely large area of the interface between the two phases compared with the mass of the dispersed phase. It follows that any chemical and physical phenomena that depend on the

2

existence of an interface become very prominent in colloidal dispersions. Interface science thus underlies colloid science.
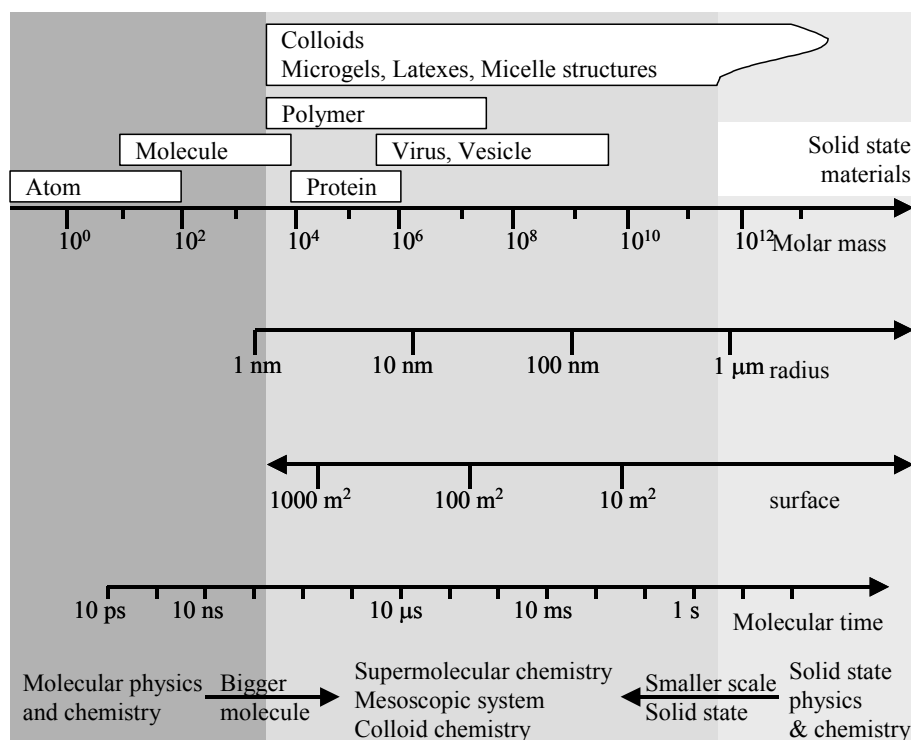
Fig. 1-1 Substance classification based on the molar mass and size[4]

A vast research is associated with the study of colloid and interface science since the discipline of 'colloids' was proposed in the 1800s[5-7]. In addition to the growth of the fundamental science itself, colloids are ubiquitous in everyday life, and may be found in substances such as hairspray, paint or in food items such as milk and mayonnaise, and therefore research performed on colloidal systems has enormous practical applications as well.

1.1.2 Colloid stability

A colloidal dispersion may be divided into two classes: lyophilic (solvent loving) and lyophobic (solvent hating) respectively, depending on the ease with which the system could be redispersed after it has been dried off. The lyophilic colloid solution is thermodynamically stable since there is a reduction in the interfacial free energy when the solute is dispersed. Owing to the high interfacial free energy, lyophobic colloids are thermodynamically unstable and tend to aggregate. This aggregation is generally undesirable and needs to be prevented.

In a stable dispersion the particle collisions do not lead to aggregation because inter-particle repulsion forces dominate. The DLVO theory [8-10]of colloid stability, developed by Derjaguin, Landau, Verwey and Overbeek during the 1940s proposes a balance of the repulsive electric double layer forces (positive by convention) and the attractive van der Waals' forces (negative by convention) that exist between all particles. These two forces were found to be of similar range and magnitude. The electrical forces increase exponentially as particles approach one another and the attractive forces increase as an inverse power of separation. As a consequence, these net forces may be expressed as a potential energy versus distance curve. A positive resultant corresponds to an energy barrier and repulsion (figure 1-2a), while a negative resultant corresponds to attraction and hence aggregation (figure 1-2b). It is generally considered that this basic theory and its subsequent modifications provide a sound basis for understanding colloid stability.

a   b
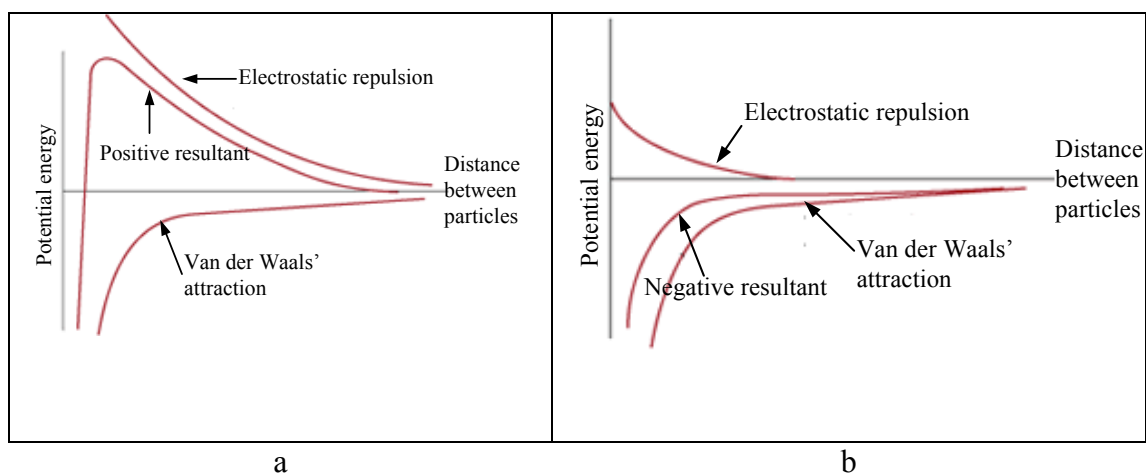
Fig. 1-2 Potential energy curve for stable and unstable dispersions

Electrostatics contributes to the stabilization of charged colloids. For neutral lyophobic colloids, the adsorption of lyophilic colloids or polymers on their surface gives rise to an additional repulsive force[11]. Macromolecules attach to the colloid surface, the loops and tails of segments extending out into the liquid phase. This **steric stabilization** comes from a combination of entropic repulsion (from the restricted configurational freedom of the adsorbed molecules when two particles collide) and osmotic repulsion (from the increased concentration of segments in the overlap region of the adsorbed layers on particle-particle contact).

Colloidal microgels are a special case of lyophility, the internal structure of a microgel is that of a swollen polymer network and can be compared with macroscopic

gels. The dye-labeled polyorganosiloxane-µ-gels that will be discussed in this thesis have a hydrophobic surface and can be redispered in non-polar organic solvents after they had been dried. In this respect they can be classified as lyophilic colloids and thermodynamically stable if there are no chemical reactions between the particles (see below).

1.1.3   Aggregation and clustering of colloids

The interaction potential between colloidal particles depends strongly on the surface chemistry of the interface between the dispersed phase and the dispersion medium and on the properties of the suspending liquid. Controlling interparticle interactions, aggregation and cluster formation is of central importance in a number of areas, ranging from cluster formation in various disease processes to protein crystallography and photonic crystals[12].

Because their behavior follows the laws of statistical mechanics, colloids are analogous to atoms but can be directly visualized. Colloids thus are regarded as "big atoms" and therefore lead to insights into fundamental understanding of condensed matter physics, ranging for example from the kinetics of crystallization to the nature of the glass state[13, 14]. Small well-defined colloidal aggregates ("colloidal molecules") have successfully been prepared by D. J. Pine et al.[15, 16], their structure ranges from sphere doublets, triangles, and tetrahedra to exotic polyhedra. This study sheds light on the optimal packing of monodisperse colloidal particles and understanding of colloidal crystallization in confined geometries, therefore offering the possibility of forming more complex colloidal phases and structures than can be realized using simple spheres.

Aggregation of nanoparticles can be induced by a variety of ways such as increase of volume fraction, introduction of an attractive interaction between particles, change of sample temperature, etc.. Here, the interaction between particles is likely the most important factor controlling the formation of clusters. Instead of the compact well-defined packing described above, in most cases aggregation and clustering lead to rather polydisperse and also quite open (low fractal dimension) structures[17]. Eventually, such clustering systems may show a sol-gel transition.

The growth of aggregates can be simulated[18-21], it usually falls into two regimes depending on the interparticle interaction potential: i) If a negligible potential barrier and a substantial minimum are present, **Diffusion limited aggregation** dominates. Every collision leads to an irreversible sticking and the aggregation rate is limited solely by the time required for two particles to encounter each other by diffusion. The aggregates may grow as long as there are particles moving around. During the diffusion of a particle through the solution it's more likely that it attaches to the outer regions than to the inner ones of the cluster. Thus, a low fractal dimension and fluffy shape of clusters is obtained; ii) On the other hand, if a significant potential barrier to aggregation is present, multiple collisions occur before the particles or smaller clusters aggregate. This is called **Reaction limited aggregation** and local rearrangement of particles within aggregates is possible in this case, thus leading to higher dimension aggregates, namely, a more uniform and compact structure.

Above all, particle clustering strongly effects the properties of colloidal dispersions and the eventual structures built from individual nanoparticles[22]. Here, we are interested in understanding the general mechanism of photoreaction induced cluster formation in more detail by employing an experimental system which allows us to control the aggregation rate and the partial reversibility of the aggregation process. Thus, properties of this colloid dispersion could be changed in a controlled way.

1.1.4 Colloid assemblies

Nanoparticle assemblies are of considerable interest for both fundamental research and applications, since they provide direct bridges between nanometer-scale objects and the macroscale world. Different methods have been developed for controlling the structure and aggregation of large numbers of colloidal particles, therefore enabling the fabrication of coatings, artificial opals, and complex ceramic bodies[6].

For instance, the crystallization of monodisperse spherical colloids under physical confinement can generate three-dimensional periodic lattices, leading to an interesting photonic bandgap structure which is responsible for the beautiful attractive color of opals[23]. The unique features associated with this new class of materials are

technologically important because they might eventually lead to the fabrication of more efficient light sources, detectors, and wave guiding structures.

A colloid assembly can also be obtained through surface directed colloid patterning[24], layer-by-layer self-assembly of colloidal nanoparticles[25], the Langmuir-Blodgett (LB) technique[26], and so on. Besides, a directed assembly technique has also been examined where colloidal spheres are constrained in space by set dimensions. A well designed template allows for the organization of spheres in well-defined structures.[16, 27] Figure 1-3 shows an example of the well-defined organization of monodisperse colloid particles in liquid emulsion droplets and effected by different droplet size, as already mentioned before.
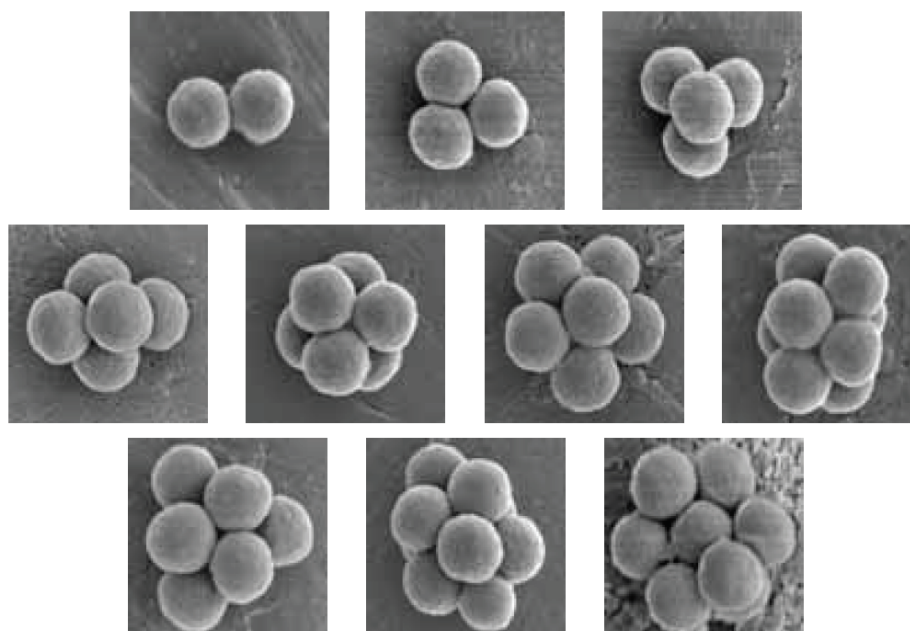
Fig. 1-3 Cluster configuration at different aggregation numbers, from Manoharan et al., Science, 301, 483(2003)

By choosing a suitable template, researchers can obtain a vast variety of structures of a colloid assembly including hollow spheres. Such hollow spheres composed of smaller colloidal particles might become important for drug delivery, catalysis, coatings, composite materials, and protecting sensitive agents such as enzymes and proteins. For example, colloidosome capsules[28] fabricated by the assembly of colloidal particles onto the interface of emulsion droplets have elastic shells whose permeability and elasticity can be precisely controlled. An alternative route to microcapsules is a layer-by-layer technique which can lead to hollow spheres

of various nano-composites[29]. In this thesis we will study the fabrication of colloidal nanoparticle-based hollow spheres using a water-in-oil-in-water emulsion template.

1.2 Microcapsules and controlled release

As mentioned, colloidal nanoparticles may lead to higher order structures, for example hollow microspheres. One of the important applications of such hollow spheres[30, 31] is their capability of encapsulating guest molecules, and the controlled release behaviour. Controlled delivery technology represents one of the frontier areas of science, which involves multidisciplinary scientific approach from the fields of chemistry, material science, engineering, pharmacology and biological science. The advantages of controlled release compared to conventional dosage forms include: delivery to the required site; delivery at the required rate; reduced dangers of overdose, or side effects; and also economic advantages by virtue of more efficient dosage at the expense of possibly more complicated fabrication. The field of the intelligent drug delivery technology has grown and diversified rapidly in recent years. In those systems the drug or a substance used as model drug were released with an on–off switching mechanism in response to a narrow change of environmental stimuli signals, such as temperature[32], pH[33], light[34], electric field[35], etc.. Concerning the intelligent drug delivery system, the preparation and applications of the stimuli-responsive materials appears to be very important.

Here we are interested in developing a new species of optically controllable microcapsules by combining a templating technique using water/oil/water emulsions with our spherical photoreactive nanoparticles. Importantly, the controlled release behaviour of these photo-addressable microcapsules will also be studied.

1.3 Goal of this work

The cluster formation of nanoscopic colloidal particles in solution as a result of interparticle attraction as well as the structure of the aggregates play a very important role concerning the properties of many technical materials, as described above. Furthermore, new and interesting supramolecular structures can be prepared via a well-defined and controlled aggregation process. Here, reversible cluster formation may open up a synthetic route to supramolecular containers with controlled release.

R-Si(OMe)₃ — **Monomer**

Nanoparticle

Hollow Microsphere

Release Test
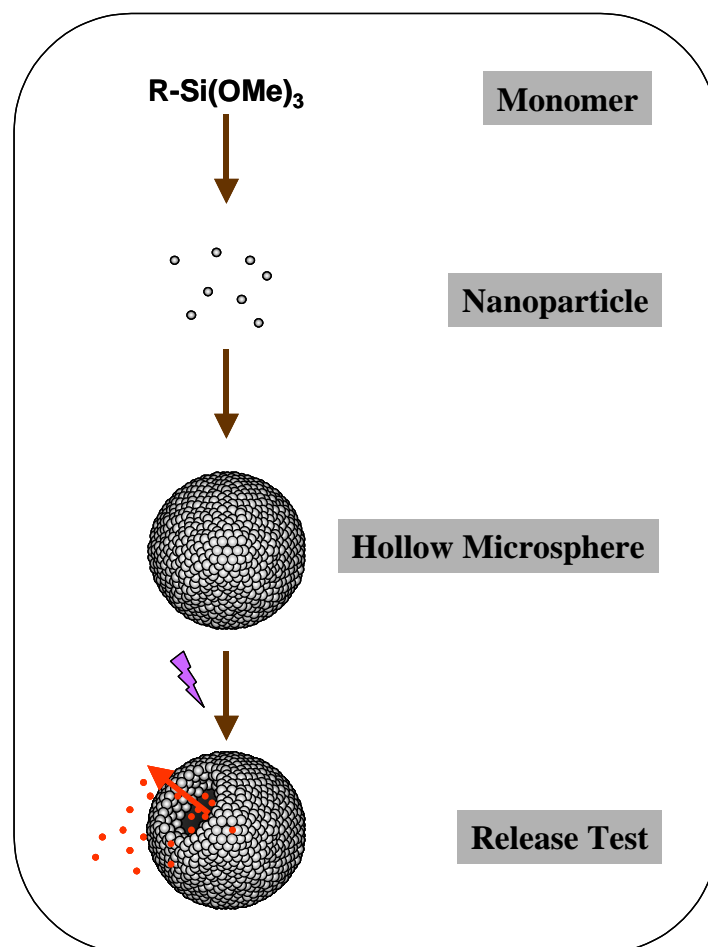
Fig. 1-4 The synthetical path towards the photocleavable microcapsule

In figure 1-4, the path from monomer to nanoparticles, and to interesting hollow microspheres is schematically described. Previously, Graf et al. have prepared highly crosslinked poly(organosiloxane) nanospheres (particle radius about 10 nm) which could be labeled chemically with a variety of organic dye molecules. They also observed the cluster formation of these photoreactive dye-labeled nanoparticles induced by inter-particle photocrosslinking[36, 37]. In this work, we will explore the possibility of a reversibility of this cluster formation based on photoreactive nanoparticles containing a different species of photolabels, and furthermore use these photoreactive nanoparticles to build photocleavable hollow microspheres which might become interesting in the application of controlled release.

9

2 METHODS

2.1 Light scattering [38, 39]

Light scattering occurs when polarizable particles in a sample are placed in the oscillating electric field of a beam of light. The varying field induces oscillating dipoles in the particles and these radiate light in all directions. This important and universal phenomenon represents the basis to answer the questions why the sky is blue and why fog and emulsions are opaque. Now, light scattering has been utilized in many areas of science to determine particle size, molecular weight, shape, thermodynamic properties, diffusion coefficients etc.

2.1.1 Static Light Scattering

In static light scattering the time average value of the scattered intensity is measured as function of the scattering angle. The weight average of the molar mass M_w, the z-average of the mean squared radius of gyration $\left\langle R_g^2 \right\rangle_z$ and the second virial coefficient of the osmotic pressure A_2 can be determined by using static light scattering. Therefore, historically, light scattering is one of the most effective methods to determine absolute molar masses and to obtain size information of polymers or biopolymers – without reference to standards.

As mentioned above the oscillating electric field of light induces oscillating dipoles within molecules and these therefore radiate light in all directions. The wavelength of the scattered light is identical with the wavelength of the incident beam. Therefore the trace of light within a strong scattering medium can be observed as a weak shining beam (Tyndall effect). Tyndall explored this phenomenon systematically in 1871 and he observed that this effect is much more pronounced using blue light as compared to red light.

Some years later Rayleigh started to explore light scattering. With the assumption of disorderly distributed molecules in space he found – applying the Maxwell theory of electrodynamics – that the so called Rayleigh ratio of scattered intensity and primary beam intensity is given by:

$$R(\theta) = \frac{Ir^2}{I_0} = \frac{8\pi^2}{\lambda_0^4} \sum_{k=1}^{\infty} N_k \alpha_k^2 (1 + \cos^2 \theta) \tag{2-1}$$

with :

$R(\theta)$:   Rayleigh ratio as a function of scattering angle θ

I :   Intensity of the scattered light

I_0 :   Intensity of the primary beam

r: Distance between detector and scattering volume

λ_0:   Wavelength of the primary beam in vaccum

N_k: Number of scattering centers

α_k: Polarizability of the scattering center k

θ: Angle between primary and scattered beam

Using vertically polarized light of a laser, the scattering intensity (of small particles) is independent of the scattering angle and the so called polarization term $(1+\cos^2 \theta)$ equals 2.

The measured scattered intensity is depending on the experimental apparatus. To obtain the absolute scattered intensities, several pure liquids are measured using special experimental setups[38]. These liquids (e.g. toluene or benzene) are utilized as calibration standards and with their help the absolute scattering intensities of other liquids and solutions are determined. For the measurement of the Rayleigh ratio of any solution the following formula has to be applied:

$$R(\theta) = \frac{I_{solution}(\theta) - I_{solvent}(\theta)}{I_{s\tan dard}(\theta)} \cdot I_{abs} \qquad (2\text{-}2)$$

With : I_{abs} : Absolute scattering intensity of the standard.

All specific parameters of the scattering apparatus (e.g. distance r of sample-detector, size of the scattering volume, primary beam intensity of the laser) are therefore eliminated.

Einstein and Smoluchowski developed the fluctuation theory. Here, the fluctuation of the polarizability in a liquid or a solution is described as a function of fluctuations of the density and fluctuations of the concentration due to thermal movement of the molecules. Scattering can only occur if there are differences of the refractive index of a small volume compared to its neighborhood.

For small particles we can write:

$$R(\theta) = \frac{4\pi^2}{\lambda_0^4 N_L} \left\{ \rho \cdot n_0^2 \left[\frac{dn}{d\rho}\right]^2 RT\beta + \left[n_0 \frac{dn}{dc}\right]^2 RT \frac{M_0}{\rho_0} \frac{c}{\left[\frac{-d\Delta\mu}{dc}\right]} \right\}$$ (2-3)

With :

N_L: Avogadro constant

ρ, ρ_0 :   Density of the solution and solvent

n, n_0 :   Refractive index of solution and solvent

R: Universal gas constant

T: Absolute temperature in Kelvin K

β: Isothermal compressibility

M_0:   Molar mass of the solvent

c :   Concentration of the solute material

$\Delta\mu$:   Difference of the chemical potential of solution and solvent

$\left[\dfrac{dn}{dc}\right]$:   Refractive index increment due to concentration changes

$\left[\dfrac{dn}{d\rho}\right]$:   Refractive index increment due to density changes

In Equation (2-3) there are two contributions to the Rayleigh ratio: the first term describes the contribution of density fluctuations, the second term the contribution of concentration fluctuations in the solution. For dilute solutions it is assumed that the contribution of the density fluctuations of solution and solvent are the same. Therefore the scattering of the dissolved substance is given by:

$$R(\theta) = R(\theta)_{solution} - R(\theta)_{solvent} = \frac{4\pi^2 n_0^2}{\lambda_0^4 N_L} \left[\frac{dn}{dc}\right]^2 \frac{RTM_0 c}{\rho_0 \cdot \left[\frac{-d\Delta\mu}{dc}\right]}$$ (2-4)

The change of the chemical potential with concentration can be described as a change of the osmotic pressure with concentration:

$$\left[\frac{d\Delta\mu}{dc}\right] = \frac{M_0}{\rho_0}\left[\frac{d\Pi}{dc}\right] \tag{2-5}$$

with Π: Osmotic pressure

Use of a series expansion of the osmotic pressure with respect to concentration yields:

$$\left[\frac{d\Pi}{dc}\right] = RT\left[\frac{1}{M} + 2A_2c + 3A_3c^2 + \cdots\cdots\right] \tag{2-6}$$

with A_2, A_3 : Virial coefficients of the osmotic pressure

Introducing Equation (2-5) and (2-6) in Equation (2-4) yields:

$$\frac{Kc}{R(\theta)} = \left[\frac{1}{M} + 2A_2c + 3A_3c^2 + \cdots\cdots\right] \tag{2-7}$$

with $K = \frac{4\pi^2 n_0^2}{\lambda_0^4 N_L}\left[\frac{dn}{dc}\right]^2$: Optical constant

M: Molar mass of the dissolved material

Equation (2-7) is only valid for small particles which are randomly distributed in space, and therefore behave like point dipoles. And for polymers with dimensions in the range of the wavelength of the light applied (particles larger than $\lambda/20$) interference of the scattered light emitted from one single particle occurs.

For large particles the dependence of the scattered intensity is expressed by the form factor $P(q)$. For the calculation of $P(q)$, it has to be considered that due to thermal (Brownian) motion a particle adopts all possible orientations in space in a very short time (less than 1 µs). Therefore an average value of all possible orientations and distances is measured. Theoretically, the following expressions are derived:

$$P(\vec{q}) = \frac{1}{N^2}\sum_1^N\sum_1^N\left\langle\exp\left(i\vec{q}\vec{r}_{ij}\right)\right\rangle \tag{2-8}$$

with

$$q = |\vec{q}| = \frac{4\pi n}{\lambda_0}\sin\left(\frac{\theta}{2}\right) : \text{Norm of the scattering vector}$$

N: Number of scattering centers within a particle

$\vec{r}_{ij} = \vec{r}_i - \vec{r}_j$:   Distance of scattering centers i and j

n: Refractive index of the solvent

Integration over all possible orientations from $\varphi = 0$ to 2π and $\theta = 0$ to π yields:

$$P(q) = \frac{1}{N^2} \sum_{1}^{N} \sum_{1}^{N} \left\langle \frac{\sin(qr_{ij})}{qr_{ij}} \right\rangle \text{ with } i < j \tag{2-9}$$

Equation (2-9) depends only on the distances between the scattering centers within a single particle. For small values of the scattering vector q, the form factor P(q), which only depends on shape and size of the particle, can be rewritten as a polynomial series:

$$P(q) = 1 - \frac{q^2}{3! N^2} \sum_{1}^{N} \sum_{1}^{N} \left\langle r_{ij}^2 \right\rangle + \cdots \text{ (break off after the 2nd term)} \tag{2-10}$$

The mean squared radius of gyration is defined by:

$$\left\langle R_g^2 \right\rangle = \frac{1}{N} \sum_{i}^{N} \left\langle \vec{r}_i^2 \right\rangle = \frac{1}{2N^2} \sum_{i}^{N} \sum_{j}^{N} \left\langle r_{ij}^2 \right\rangle \tag{2-11}$$

with $\vec{r}_i$: Distance vector of scattering center i from the center of mass of the particle comparing eqs. (2-11) and (2-10) yields for monodisperse particles:

$$P(q) = 1 - \frac{1}{3} q^2 \left\langle R_g^2 \right\rangle + \cdots \tag{2-12}$$

Therefore, using the relationships $\frac{1}{1+x} \cong 1 - x$, or $\frac{1}{1-x} \cong 1 + x$, we can rewrite eq. (2-7) into the famous Zimm Equation:

$$\frac{Kc}{R(\theta)} = \frac{1}{M_w} \left[1 + \frac{1}{3} q^2 \left\langle R_g^2 \right\rangle_z \right] + 2 A_2 c + \cdots \tag{2-15}$$

By plotting $\frac{Kc}{R(\theta)}$ as a function of $q^2 + kc$, we can extrapolate as two linear relations $c \rightarrow 0$ and $q^2 \rightarrow 0$. From the intercept of both the c dependence as well as the q^2 dependence we can calculate the average molar mass M_w, and from the slopes we get

the z-average of the mean squared radius of gyration $\left\langle R_g^2 \right\rangle_z$ (from q^2 dependence) and the second virial coefficient A_2 of the osmotic pressure (from c dependence).

2.1.2 Dynamic Light Scattering

Whereas in static light scattering the time average of the scattering intensity is measured, in dynamic light scattering the fluctuations of the scattering intensity due to Brownian motion of the particles are correlated by means of an intensity-time autocorrelator. The correlator monitors the scattering intensities in small time intervals τ over a total observation time $T = N\tau$ with N the total number of small possible time intervals τ. The autocorrelation function $g_2(t)$ is then calculated as

$$g_2(t) = \left\langle I(0) \cdot I(t = n \cdot \tau) \right\rangle \qquad \text{n} = 1, 2, 3, \ldots\ldots, \text{N} \tag{2-16}$$

From $g_2(t)$ the correlation function of the electric field $g_1(t)$ is derived by

$$g_1(t) = \left(\frac{g_2(t) - A}{A} \right)^{1/2} \tag{2-17}$$

with A an experimentally determined baseline, i.e.

$$A = \lim_{t \to \infty} g_2(t) = \left\langle I \right\rangle^2 \tag{2-18}$$

In this limit the intensities $I(t = 0)$ and $I(t = \infty)$ are not correlated, i.e.

$$\left\langle I(t = 0)I(t = \infty) \right\rangle = \left\langle I(t = 0) \right\rangle \left\langle I(t = \infty) \right\rangle = \left\langle I \right\rangle^2 \tag{2-19}$$

Since $\quad \lim_{t \to \infty} g_2(t) = \left\langle I \right\rangle^2 \tag{2-20}$

the intensity correlation function decays from $\left\langle I^2 \right\rangle$ to $\left\langle I \right\rangle^2$.

For scattering centers undergoing Brownian motion it is the Fourier transformation of the van Hove space time correlation function which expresses the probability that one particle moves a distance ΔR within a time interval t. This function $G(\Delta \vec{R}, t)$ is given by a Gaussian distribution of mean squared displacements ΔR^2:

$$G(\Delta\vec{R},t) = \frac{2\pi}{3}(\Delta R^2(t))^{\frac{3}{2}} \exp\left(-\frac{3\Delta R^2(t)}{2\langle\Delta R^2(t)\rangle}\right) \tag{2-21}$$

$$g_1(q,t) \cong \int G(\vec{R},t)\cdot\exp(i\cdot\vec{q}\cdot\vec{R})d\vec{R} \tag{2-22}$$

$$g_1(t) = \exp(-q^2\cdot\frac{\langle\Delta R^2\rangle}{6t}\cdot t) = \exp(-q^2\cdot D\cdot t) \text{ with } \langle\Delta R^2\rangle = 6\cdot D\cdot t \tag{2-23}$$

The diffusion coefficient we measure is a z-average value, and applying the Stokes-Einstein equation we can calculate the hydrodynamic radius of a corresponding sphere:

$$R_h = \left\langle\frac{1}{R_h}\right\rangle_z^{-1} = \frac{kT}{6\pi\eta_0 D_z} \tag{2-24}$$

with k the Boltzmann factor, T the temperature in K and η_0 the viscosity of the solvent.

2.2 UV Curing

The experimental procedure that induces the chemical reaction of molecules by using Ultraviolet (UV) light in the suitable range is called UV curing. In general, UV light ranges from 10 - 400 nm. (Figure 2-1) Because of its relatively short wavelength, the high energy of UV light is able to initiate photoreactions of molecules. The advantage of UV Curing against conventional methods like heat is obvious: faster cure speeds, lower reaction temperature, less odour, etc..
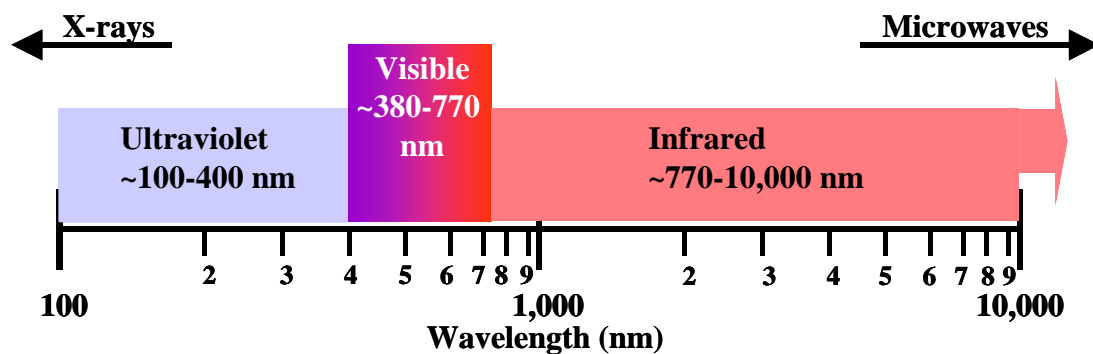

Fig. 2-1 The optical portion of the electromagnetic spectrum

Good UV Curing requires a powerful UV lamp with variable wavelengths. Depending on the application, the radiation of the lamp has to meet specific needs. For example, the radiation of a mercury lamp is around 230-320 nm, iron halide lamp emission is 300-450 nm, lead doped lamp emission is 360-370 nm, and a xenon lamp offers spectra with radiation in the visible range as well as in IR and near UV range. The Hg-Xe Lamp in our lab is a combination of a mercury and xenon lamp, which provides a very broad spectrum from far ultraviolet to infrared, and the output can be as high as 200 watt. Figure 2-2 is the spectral distribution of the light emitted by this Hg-Xe lamp.

Wavelength Nanometer	Percent Output
230-280	0.7
280-330	2.0
330-380	10.0
380-430	6.1
430-480	7.9
480-530	4.0
530-580	18.6
580-630	10.1
630-680	2.7
680-730	2.7
730-780	2.0
780-830	2.9
830-880	2.6
880-930	5.4
930-980	3.1
980-1030	7.4
1030-1080	7.4
1080-1130	1.0
1130-1180	1.0
1180-1230	0.7
1230-1280	6.7
1280-2500	6.7
	100.0
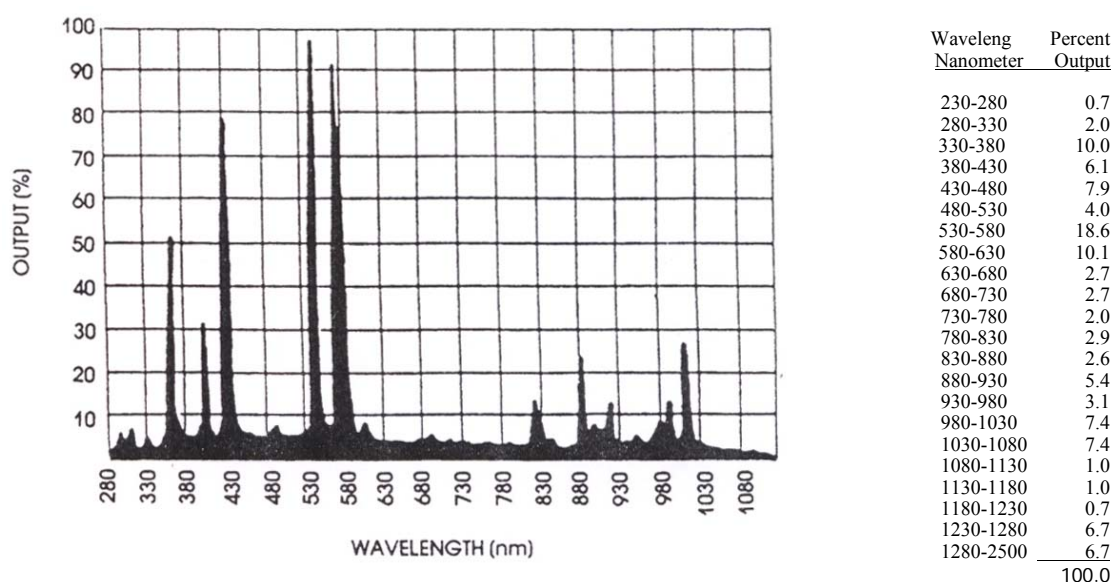
Fig. 2-2 Spectral distribution of the light emitted by Hg-Xe lamp used for irradiation.

To find an optimized experimental condition, a suitable range of UV light has to be selected. For this purpose, an optical filter is usually employed. Filters operate by absorption or interference. Colored glass filters are doped with materials that selectively absorb light by wavelength, and obey Beer-Lambert's law. The peak transmission is inherent to the additives, while bandwidth is dependent on thickness. Sharp-cut filters act as long pass filters, and are often used to "subtract out" long wavelength radiation. Interference filters rely on thin layers of dielectric materials to cause interference between wavefronts, providing very narrow bandwidths. Any of these filter types can be combined to form a composite filter that matches a particular photochemical or photobiological process.

2.3 Microscopy

Microscopy is one of the most important inventions in the history of science: an instrument that enables the human eye, by means of a lens or combinations of lenses, to observe enlarged images of tiny objects. It made visible the fascinating details of "worlds within worlds". From simple light microscopy to light confocal microscopy, to electron microscopy, until the invention of scanning probe microscopy, microscopy became a very important experimental technique in chemistry, physics and bioscience.

2.3.1 Optical Microscopy

The basic optical microscope consists of an objective and an eyepiece as well as a light source. It is in principle a simple lens system for magnifying small objects. The first lens, called the objective, has a short focal length (a few mm), and creates an image of the object in the intermediate image plane. This image in turn can be looked at with another lens, the ocular or eyepiece, which can provide further magnification. Optical microscopy can be employed as bright field microscopy where a transparent or translucent specimen is either naturally colored or stained and appears dark against a bright, white background, or as dark field microscopy in which case the specimen (transparent or semi-transparent) is a bright object against a dark, usually black, background. With some special technology, more advanced optical microscopy like confocal microscopy can be obtained.

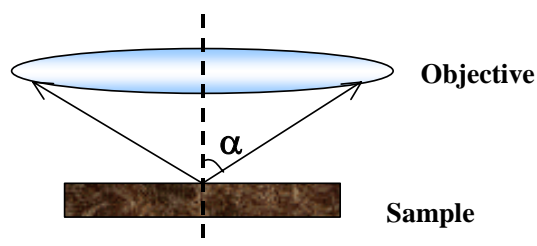**Fig. 2-3** Scheme for the focus length of the optical microscopy objective

The magnification of classical optical microscopy depends on the focus length of the objective and eyepiece[40] (see figure 2-3), and the resolution is given as *0.61λ/(n·sin(α))*, with *n* the refractive index of the medium between objective and object, and *α* the angle of the incident beam (see figure 2-3). Since the refractive

index of air is around 1 and $\alpha < 90^o$, the maximum lateral resolution of optical microscopy is about half the optical wavelength (≈ 350 nm). Therefore the application of classical optical microscopy is limited.

2.3.2 Fluorescence Confocal Microscopy

Confocal microscopy (CM)[41] is a special technique of light microscopy in which the inspected region of the specimen is a small (submicron) voxel (=3D pixel). As shown in figure 2-4, signals from nearby voxels are suppressed by a special (confocal) optical setup. An important element of this setup is a pinhole in the image plane. The point source of light, the inspected voxel and the pinhole are confocal. Light coming from the neighborhood of the inspected voxel is blocked from reaching the detector. This feature improves the resolution of CM especially in z-direction as compared to an ordinary microscope.
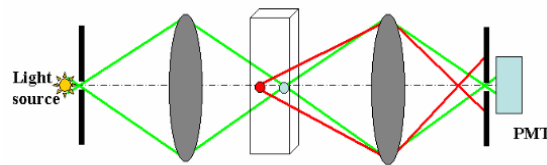

Fig.2-4 Simplified scheme for the principle of confocal microscopy.

Fluorescence CM (FCM)[42] is a version of CM in which the inspected specimen is doped with a high-quantum-yield fluorescent dye that strongly absorbs at the wavelength of the exciting laser beam. Excited dye molecules fluoresce at somewhat longer wavelengths. The difference between the fluorescence and absorption wavelengths is called the Stokes shift. If the Stokes shift is sufficiently large, the exciting and fluorescence signals can be efficiently separated by optical filters so that only the fluorescence light can reach the detector. If the specimen is heterogeneous, the concentration of the fluorescent probe is coordinate-dependent, which results in a high-contrast image. The FCM technique makes it possible to visualize features in living cells and tissues; it is successfully applied in flow cytometry and even for single molecule detection. In essence, the traditional FCM technique visualizes the concentration (density) distribution of fluorescence probes in

the sample. Figure 2-5 is the schematic picture of the fluorescence confocal microscope Leica TCS SP2 which was used to investigate the emulsion sample stained by fluorescent quantum dots in this thesis.
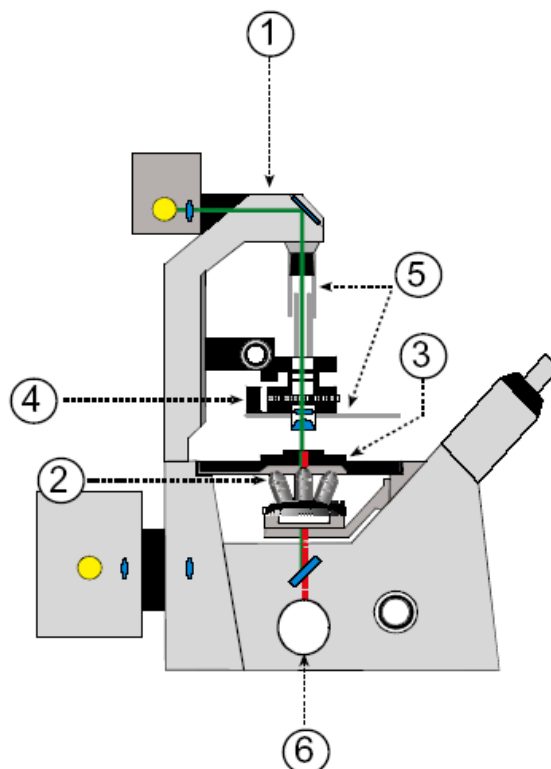
Fig. 2-5 Schematic picture of fluorescence microscope Leica TCS SP2. (1: Inverse microscope stand, 2: Objectives, 3: Microscope specimen stage, 4: Condenser, 5:Aluminum disc as beam collector, protective sleeve between condenser and transmitted light detector, 6: Connection for scan head.)

2.3.3 Electron Microscopy [43, 44]

The introduction of the electron microscope in the 1930's is a great breakthrough for microscopy. Co-invented by the Germans Max Knoll and Ernst Ruska in 1931[43], Ernst Ruska was awarded half of the Nobel Prize for Physics in 1986 for his invention. (The other half of the Nobel Prize was divided between Heinrich Rohrer and Gerd Binnig for the STM[45].) In this kind of microscope, electrons are sped up in vacuum until their wavelength is extremely short (only one hundred-thousandth that of visible light). Beams of these fast-moving electrons are focused on a cell sample and are absorbed or scattered by the cell's parts so as to form an image on an electron-sensitive photographic plate.

The invention of electron microscopy benefited from the development of quantum mechanics when it became clear that microscopic particles such as atoms, electrons and neutrons in some cases behave like waves. Both views, the classical picture of a particle characterized by a momentum p, and that of a wave with a wavelength λ, are only two different complementary viewpoints of the same physical object. Both quantities are related by the de Broglie relation $\lambda = h/p$, where h is the planck constant. Some experiments are better understood in terms of the particle approach, others are better described in the wave picture.

To understand the resolution of electron microscopes and later diffraction techniques the wave approach is more instructive. The resolving power of electron microscopes is substantially better than that of a light microscope, since the wavelength of the electrons, given by the de Broglie relation

$$\lambda = \frac{h}{p} = \frac{h}{\sqrt{2 m_e E_{kin}}} \qquad (2\text{-}25)$$

is smaller. Here, m_e is the electron mass, and E_{kin} is their kinetic energy. In an electron microscope the electrons get their kinetic energy by an applied electric potential of 1 - 400 kV. This leads to wavelengths of 0.4 –0.02 Å. Electron beams can be deflected by electromagnetic fields. This allows the construction of electron optics be using electromagnetic lenses. A broad overview can be found in reference[46].

The electron microscope exists in two basic modifications: the transmission electron microscope (TEM) and the scanning electron microscope (SEM). In transmission electron microscopy, an electron beam is transmitted through the sample. All electrons have the same energy and thus the same wavelength because they are accelerated by the same voltage. The scattered electrons are projected onto a phosphorous screen or an imaging plate to obtain the image. With the addition of energy dispersive X-ray analysis (EDXA) or energy loss spectrometry (EELS), the TEM can also be used as an elemental analysis tool, capable of identifying the chemical elements within areas less than 0.5μm in diameter.

In scanning electron microscopy (SEM), a finely focused electron beam scans across the surface of the sample and generates secondary electrons, backscattered electrons, and characteristic X-rays. These signals are collected by detectors to form

images of the sample displayed on a cathode ray tube screen. Features seen in the SEM image could be analyzed for elemental composition by using EDS (Energy Dispersive X-ray Spectroscopy) or WDS (Wave-length Dispersive Spectroscopy).

If pushed to the limit, electron microscopes can make it possible to view objects as small as the diameter of an atom. Most electron microscopes used to study biological material can "see" down to about 10 angstroms--an incredible feat, for although this does not make atoms visible, it does allow researchers to distinguish individual molecules of biological importance. In effect, EM can magnify objects up to 1 million times. Nevertheless, all electron microscopes suffer from a serious drawback. Since no living specimen can survive under their high vacuum, they cannot show the ever-changing movements that characterize a living cell. The invention of scanning probe microscopy nicely solved this problem.

2.3.4 Atomic Force Microscopy (AFM)

The atomic force microscope (AFM) is a member of a new class of microscopes termed the scanning probe microscopes (SPM). The first of the probe instruments to be developed was the scanning tunnelling microscope (STM) which earned its inventors, Gerd Binnig and Heinrich Rohrer, the Nobel Prize in physics in 1986 [47].
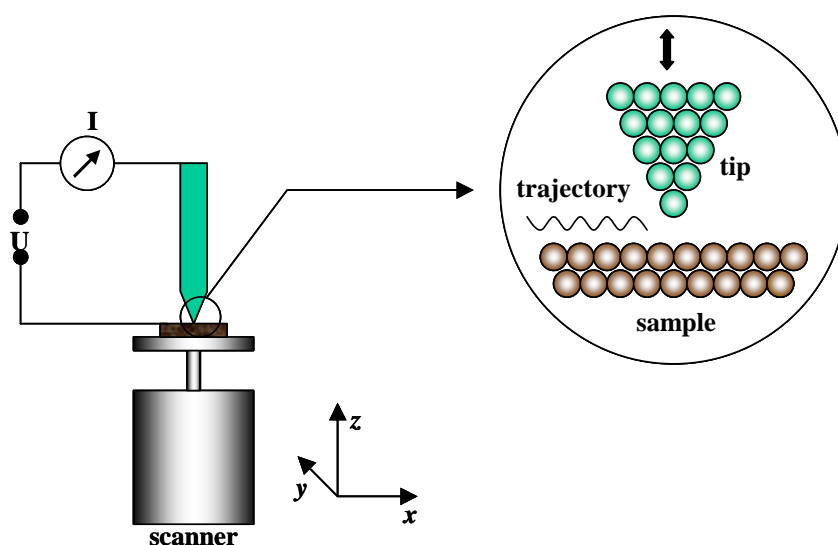

Fig. 2-6 Schematic representation of a conducting STM tip over a sample adsorbed onto a conducting substrate.

22

In STM (Figure 2-6), a small, yet sharp, metallic probe is positioned a few nanometers above a sample adsorbed onto a very flat conducting substrate. To scan the surface the tip is pushed toward the sample until the electron clouds of each gently touch. The application of a voltage between the tip and the sample causes electrons to flow through a narrow channel between the respective electron clouds. This flow is called the tunnelling current. Since the density of an electron cloud descends exponentially with distance, the tunnelling current is extremely sensitive to the increasing distance between the tip and the surface. A change in the distance by an amount equal to the diameter of a single atom causes the tunnelling current to change by a factor of as much as 1000. It is this sensitivity that is the key to the operation of the STM.

Piezoelectronics provides the answer to positioning the tip. Compression of a sample of material that has piezoelectric properties generates a potential difference across the material. Conversely, the application of electrical signals across piezoelectric materials can be used to control the expansion or contraction of these materials to a high degree of accuracy. This effect is used to position, and also scan, the conducting probe of the STM over the surface of the sample. Rather than simply monitoring the tunnel current during a scan, it is usually more convenient to control the vertical displacement of the probe by means of a feedback circuit designed to maintain a constant tunnelling current. The motions of the probe can then be amplified so as to visualize the surface features of the sample. Maintaining a constant tunnelling current makes it possible for the probe to 'lift over' rather than 'crash into' samples deposited on the conducting substrate.

The application of the STM is naturally restricted to conducting or semi-conducting samples. In 1985 Binnig, together with Calvin Quate and Christopher Gerber, introduced the atomic force microscope (AFM), a scanned-probe device that does not need a conducting specimen[47]. Like all other scanning probe microscopes, the AFM utilises a sharp probe moving over the surface of a sample in a raster scan. In the case of the AFM, the probe is a tip on the end of a cantilever which bends in response to the force between the tip and the sample (Figure 2-7a).

A very sharp tip has a terminal radius often less than 100 Å, it is located at the free end of a ~ 100 μm long cantilever that has got an elastic modulus that can reach tenths of N/m. Forces of a few piconewton between the tip and the sample surface

cause deflections of the cantilever in the angstrom spatial scale. A laser beam is reflected from the back of the cantilever onto a position-sensitive photodetector (PSD). As the cantilever bends, the position of the laser beam on the detector shifts. The PSD itself can measure displacements of light beams as small as 10 Å. The ratio of the path length between the cantilever and the detector to the length of the cantilever itself produces a mechanical amplification. As a result, the system can detect sub-angstrom vertical movements of the cantilever tip. The measured cantilever deflections enable the computer to generate a map of the surface topography. This apparatus is called also Scanning Force Microscope, which is a suitable name in particular for studies carried out in a micrometer and sub-nanometer scale. As a first approximation the forces contributing to the deflection of an AFM cantilever are the Van der Waals and repulsive forces. A typical force vs. distance curve, which is the negative gradient of the energy, is plotted in figure 2-7b. Two distance regimes are highlighted: 1) the contact regime; and 2) the non-contact regime. In the contact regime, the cantilever is held less than a few angstrom from the sample surface, and the interatomic force between the cantilever and the sample is repulsive. In the non-contact regime, the cantilever is held on the order of tens to hundreds of angstrom from the sample surface, and the interatomic force between the cantilever and sample is attractive (largely a result of the long-range van der Waals interactions).
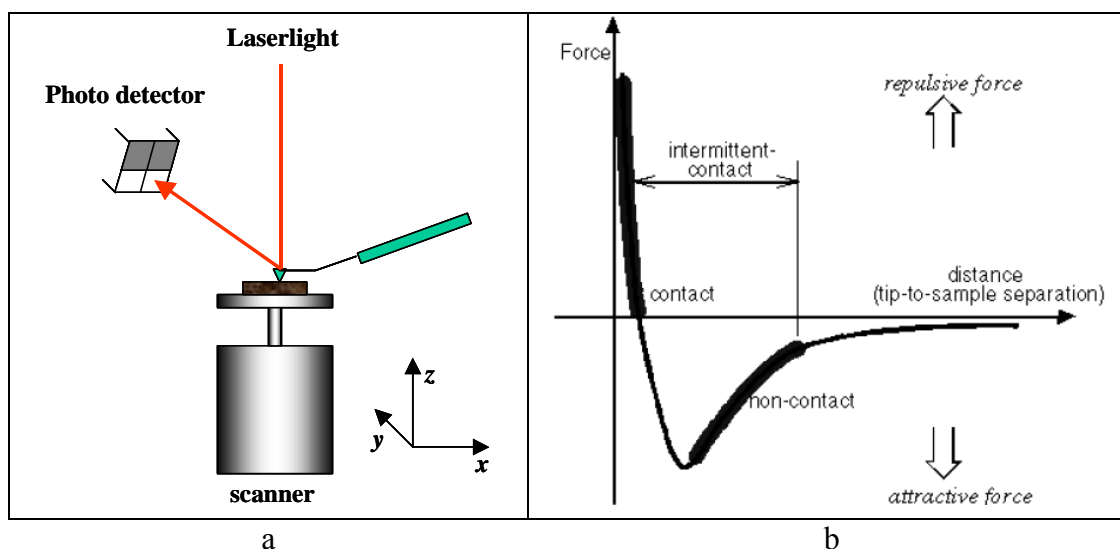

a   b

Fig. 2-7 a): Schematic representation AFM: b): Typical force-distance curve between tip and sample surface.

Three measurement modes are generally used in scanning force microscopy: contact mode, non-contact mode and tapping mode. **Contact mode** allows the tip and sample surface to come into close distance as the scanning proceeds, "contact" represents the repulsive regime of the inter-atomic force curve. The sensitivity of this distance-constant mode provides sub-angstrom vertical resolution in the image. In order to overcome the problem of the friction component during scanning in contact mode as well as to minimize the forces exerted from the tip on the sample and the effect of the capillary forces, alternative modes have been invented where the AFM cantilever vibrates near (on the order of tens to hundreds of angstroms) the surface of a sample. **Non-contact mode** is a method where the cantilever is oscillated above the sample surface at a distance that it is no longer in the repulsive regime but in the attractive regime of the inter-atomic force curve. This mode does not suffer from tip or sample degradation effects that are sometimes observed after taking numerous scans with contact AFM. Unfortunately, the lateral resolution that can be reached is only a few nanometers, which is lower than in the contact mode. **Tapping Mode** is similar to non-contact mode, except that for TM-AFM the vibrating cantilever-tip is brought closer to the sample so that at the bottom of its travel it just barely hits, or "taps" the sample. Some samples are best handled using tapping mode instead of contact or non-contact mode. In general, it has been found that tapping mode is more effective than non-contact mode both for imaging larger scan sizes, which may include greater variations in sample topography, and for the slightly higher resolution that can be achieved due to the stronger tip-sample interaction forces that are sampled.

In this thesis, all samples were measured with a multimode AFM (Digital Instrument) in air environment in Tapping Mode using the E-scanner in a range of scan lengths from 10 μm to 0.3 μm.

2.4 UV-Vis Spectroscopy

UV-vis spectroscopy is the quantitative measurement of the absorption of near-ultraviolet and visible light by a sample. Ultraviolet and visible light possess enough energy to promote outer electrons to higher energy levels. UV-vis spectroscopy therefore detects and records the electronic transitions of molecules as they absorb light in the UV and visible regions of the electromagnetic spectrum. Any species with an extended system of alternating double and single bonds will absorb

UV light, and some chromogenic materials also absorb visible light, making UV-vis spectroscopy applicable to a wide range of samples.

UV-vis spectra are very useful for quantitative concentration measurements. Here, the concentration of an analyte in solution can be determined by measuring the absorbance at some wavelength and applying the Beer-Lambert law:

$$A = \log \frac{I_0}{I} = \varepsilon \cdot c \cdot d \qquad (2\text{-}26)$$

with I, I_o: intensity of light after it passes through the sample and initial light intensity.

ε : molar extinction coefficient

c : molar concentraion

d : optical path length

For solutions of the same chromophore, ε and d remain unchanged, and we get:

$$\frac{c}{c_0} = \frac{A}{A_0} \qquad (2\text{-}27)$$

With the help of a reference sample of known concentration (c_0), an unknown concentration (c) of the sample can be determined by measuring its UV absorption.

2.5 Fluorescence Spectroscopy

The emission of light from any substance is called luminescence. About 200 years ago, Sir G. G. Stokes studied the quinine compound and found that the emitted light has a longer wavelength than the light absorbed, an effect which is called stokes' shift. Stokes' paper appeared in 1852[48], and around 70 years later, A. Jablonski and others developed a modern theoretical understanding of Stokes' observation[49].

Luminescence is divided into two types, depending on the nature of the ground and the excited states. In a singlet excited state, the electron in the higher energy orbital has the opposite spin orientation of the second electron in the lower orbital. These two electrons are said to be paired. In a triplet state these electrons are unpaired, that is, their spins have the same orientation. Return to the ground state from an excited singlet state does not require an electron to change its spin orientation. However, a change in spin orientation is needed for a triplet state to return to the singlet ground state. Fluorescence is the emission which results from the return of a paired electron to the lower orbital. Such transitions are quantum mechanically

"allowed" and the emission rates are typically near 10^8 sec^{-1}. These high emissive rates result in fluorescence lifetimes near 10^{-8} sec or nsec, with the lifetime the average period of time a fluorophore remains in the excited state. Phosphorescence is on the other hand the emission which results from a transition between states of different spin multiplicity, generally a triplet excited state returning to a singlet ground state. Such transitions are not allowed and the emissive rates are slow. Typical phosphorescent lifetimes range from milliseconds to seconds, depending primarily upon the importance of deactivation processes other than emission.

The absorption and emission of light are nicely illustrated by the energy level diagram suggested by A. Jablonski. (Figure 2-8)
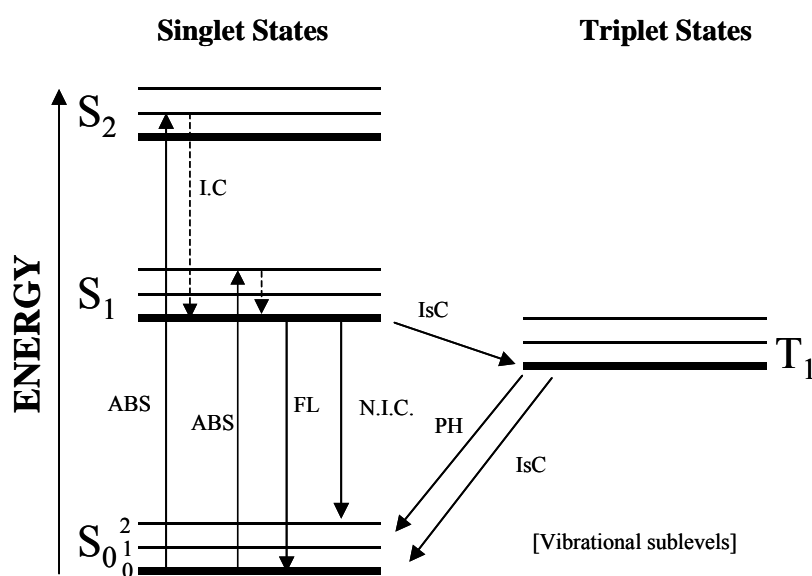
ABS - Absorbance	I.C. - Internal Conversion
S 0.1.2 - Singlet Electronic Energy Levels	N.I.C.- Nonradiative Internal Conversion
FL - Fluorescence	IsC - Intersystem Crossing
T 1 - Corresponding Triplet States	PH - Phosphorescence

Fig. 2-8 Jablonski Diagram

In the diagram the electronic singlet states S_0, S_1 and S_2 along with three vibrational energy levels are shown. In the ground state the molecule will be in the lowest vibrational level of S_0, since at room temperature the higher vibrational levels are in general not populated. The magnitude of the absorbed energy decides which vibrational level of S_1 (or S_2) becomes populated. This process occurs in about 10^{-15} sec, a time too short for significant displacement of nuclei. During 10^{-12} sec the molecule relaxes to the lowest vibrational state of S1, a process called internal conversion. Since emission typically occurs after 10^{-9} s, the molecule is fully relaxed

at the time of emission. Hence, as a rule, emission occurs from the lowest vibrational level of S1 (Kasha's rule) and the fluorescence spectrum is generally independent of the excitation wavelength. After emission the molecule returns to the ground state, possibly via vibrational relaxation. This completes the simplest case of fluorescence: excitation, internal conversion, emission and relaxation. The energy lost to the surroundings, due to vibrational relaxation and internal conversion, is the reason why a Stokes' shift is observed.

Molecules in the S_1 state can also undergo conversion to the first triplet state T_1 (intersystem crossing). Emission from T_1 is termed phosphorescence, and generally is shifted to longer wavelengths (lower energy) relative to the fluorescence. Transition from T1 to the ground state is forbidden, and as a result the rate constant for such emission is several orders of magnitude smaller than those of fluorescence. Substances which display significant fluorescence generally possess delocalized electrons formally present in conjugated double bonds. Fluorescence spectral data are generally presented as emission spectra, a plot of emission against wavelength for any given excitation wavelength. A fluorescence spectrometer is the instrument used to record either emission or excitation spectra of the fluorophore. Figure 2-9 is a simplified sketch of a fluorescence spectrometer.
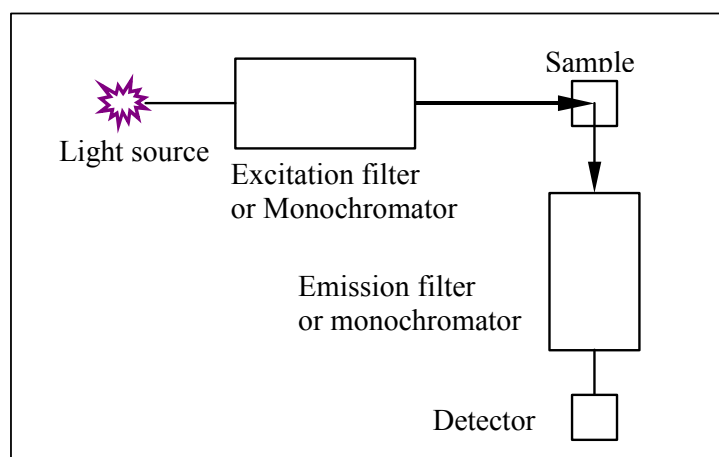

Fig. 2-9 Schematic diagram of a fluorescence spectrometer.

An ideal spectrofluorometer should contain:

1. The light source with a constant photon output at all wavelengths.
2. The monochromator which not only lets pass photons of all wavelengths with equal efficiency and independent of polarization, but also select photos of a certain wavelength.

3. The detector (photomultiplier tube) which detects photons of all wavelengths with equal efficiency.

The fluorescence is detected with photomultiplier tubes and quantified with the appropriate electronic device. The output is usually presented in graphical form and may be stored in a computer memory.

Fluorescence spectra and quantum yields (I_e/I_0, with I_0 the intensity of the light absorbed by a sample and I_e the intensity of the light emitted from the sample.) are generally more dependent on the environment than absorption spectra and extinction coefficients. Interactions between a fluorophore and other species in the surrounding environment can produce environment-sensitive fluorescence, this special effect was used in this thesis to study the release behaviour of microcapsules.

2.6 GPC and FFF

2.6.1 GPC (Gel Permeations Chromatography)

Gel Permeation Chromatography, also known as Size Exclusion Chromatography (SEC), is an important relative method to determine the molecular weight and molecular weight distribution of macromolecules[50, 51].

SEC is a special application of the High Performance Liquid Chromatography (HPLC). The separation of polymer molecules is based on a size exclusion mechanism. When a polymer solution passes through a column, filled with a porous gel material (stationary phase) at certain pressure and flow rate, there will be three cases: i) large molecules can only pass through the interstitial volume (dead volume of the packing) and can not penetrate into the pores of the packing material, therefore leave the column first all at the same volume called the upper exclusion limit (total exclusion), above which the different sizes of the larger particles can not be resolved; ii) If the molecules are very small, they completely enter the pores and leave them without separation, this is the lower limit of the range of separation and called the separation threshold (total permeation); iii) Molecules of medium size cannot enter the narrowest pores and only partially permeate the stationary phase. At their disposal is a volume between the total permeation and the dead volume, which is dependent on the molecular size.

In contrast to light scattering or membrane osmosis, SEC is a relative method for the determination of molar masses and therefore needs calibration. As direct experimental data, the concentration of the eluted solution against time is detected by measuring the refractive index or UV-vis absorption. The molar mass M_i of each fraction must be determined by means of calibration standards which have to be characterized by an absolute method of molar mass determination (light scattering, osmosis).

Molar masses and molar mass distributions can only be determined quantitatively if the calibration standards and the unknown sample are chemically identical, i.e. consist of identical monomers and, in case of polymers, exhibit the same chain architecture. The reason for this restrictive condition is that the hydrodynamic volume is different for different standard modification of polymers although they have the same molar mass. Wherefore, the conventional calibration method, where the logarithm of molecular weight is plotted against elution volume, does not yield a universal curve for all the polymers. In this case, alternative calibration is required.

In 1967, Benoit[52] showed that the calibration for polymers of different types can be merged into a single line when plotted as $\log([\eta] \cdot M)$ versus retention volume. According to Einstein's viscosity law one can write:

$$[\eta] = \frac{2.5}{\rho} = \frac{2.5 \cdot N_A \cdot V_h}{M} \quad \text{which yields: } V_h = const. \cdot [\eta] \cdot M$$

where $[\eta]$ the intrinsic viscosity, V_h the hydrodynamic volume and M the molecular weight, N_A the Avogadro constant. Plotting $\log([\eta] \cdot M)$ vs. V_h yields a common curve for different kinds of polymers. Here V_h determines retention in the chromatographic columns, and thus proportional to elution volume V_e, therefore the plot of $\log([\eta] \cdot M)$ vs. V_e represents a universal calibration independent of the shape of the polymers.

2.6.2 Asymmetrical Flow Field –Flow Fractionation (AF-FFF)

Field-Flow-Fractionation (FFF) is analogous to chromatography, while the separation is achieved by an external physical field (Flow field, thermal field, electrical field, magnetic field, …) instead of a stationary phase, which acts perpendicular to a sample in a laminar flow[53, 54]. The external cross-field causes particles (or dissolved macromolecules) to partition among velocity streamlines that

are formed by the parabolic velocity profile in the carrier fluid (Figure 2-10). The velocity profile is close to zero near the walls of the channel and reaches a maximum at the center of the channel. If an external cross-field is applied, particles or macromolecules are forced or focused into different velocity streamlines, depending on the nature of interaction with the external field (gravitational, thermal, electrical, magnetic,…). Different interaction with the field results in different positions in the channel and thus in different elution velocities. Particles with smallest interaction with the field are in zones with higher flow velocity and are eluted first. The detection system of FFF is similar to that of SEC. Compared to SEC, FFF is a versatile separation technique with good resolution. Both charged and interacting systems can be characterized. However, interactions with the inner sample cell wall (membrane, see below) cannot completely be excluded.
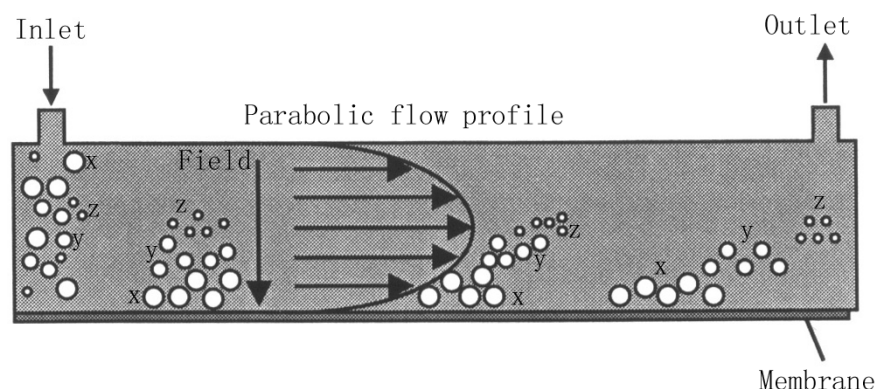

Fig. 2-10 Mechanism of an FFF separation of components x, y and z across the parabolic flow profile resulting in different flow velocities of x,y and z[4].

Asymmetrical Flow Field-Flow Fractionation (AF-FFF)[55] is a special mode of FFF which is notable for a channel that has one permeable wall at the bottom (membrane) so that the solvent can leave the channel and thus generates a crossflow. The advantage of the asymmetrical channel design in AF-FFF is the possibility to focus the sample into a very sharp band prior to separation, resulting in higher separation resolution and improved accuracy of particle size measurement.

3 DYE-LABELED POLY(ORGANOSILOXANE) NANOPARTICLES

Colloidal nanoparticles have attracted a great deal of attention because of their potential applications in optics, electronics, engineering and bioscience. Further advances of such nanoparticles require fine-tuning of the size structure, composition, spatial assembly of individual constitutes and their surface. Compared to most common polymers, polyorganosiloxanes are thermally stable and transparent to UV radiation. Importantly, they are also environmental friendly and in many cases biocompatible[56]. Baumann et al developed a synthesis procedure to prepare redispersible polyorganosiloxane-μ-gels, which nicely combine the chracteristics of nanoparticles and polyorganosiloxanes. This unusual combination of polyorganisiloxane and nanoparticle brings many interesting properties to this material. [57, 58]In this chapter, we discuss the synthesis approach for dye-labeled polyorganosiloxane-μ-gels based on the standard procedure suggested by Baumann et al.[57] and Graf et al.[36]. A photosensitive dye was coupled onto the surface of the microgel for further study.

3.1 Polyorganosiloxane μ-gels

A microgel (μ-gel) is an **intramolecularly crosslinked macromolecule** which is dispersed in normal or colloidal solutions.[59] The size of our μ-gels is usually in the range of nanometers, so more appropriately they should be called **nanogels**. The IUPAC commission on Macromolecular Nomenclature recommended **micronetwork** as a term for μ-gels[60] and defined it as **a highly ramified macromolecule of colloidal dimensions**. Simply spoken, a μ-gel is a monodisperse, strictly spherical micronetwork in the size range from 5-100 nm.

Polymerization in microemulsion has developed into a powerful technique for the preparation of strictly spherical micronetworks[61]. The final size of the polymerized particles is governed by the ratio of surfactant to monomer concentration[62, 63]. In this thesis, we studied the preparation of special dye-functionalized polyorganosiloxane-μ-gels synthesized through the polycondensation of trialkoxysilanes in aqueous solution with surfactant. We obtained strictly spherical micronetworks of around 10 nm radius and narrow molar mass distribution. However,

these particles prepared in aqueous dispersion are not redispersable in water after they have been dried due to inter-particle condensation through reactive chemical groups on the particle surface. To solve this problem, an "endcapping"[58] procedure was introduced to remove the active chemical groups through their reaction with a monofunctional silane so that the interparticle condensation can be prevented and the polyorganosiloxane-μ-gels can be redispersed in non-polar organic solvents.

In the following part, the basic features of the process leading to polyorganosiloxane-μ-gels are discussed.

3.1.1 Hydrolysis and Condensation of Alkoxysilane

The polycondensation process of alkoxysilane usually contains two steps, hydrolysis and condensation. Both steps usually occur in a one-pot process. The first step is the hydrolysis of alkoxysilane catalyzed by acids or bases. (3-1)

$$R'_nSi(OR)_{4-n} \xrightleftharpoons[H_2O/RT]{catalyst} R'_nSi(OH)(OR)_{3-n} + ROH \tag{3-1}$$
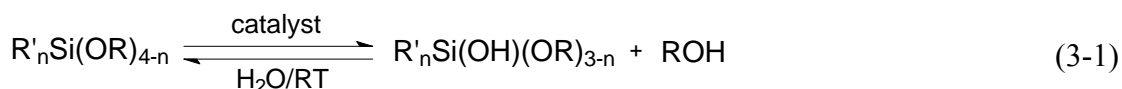
n = 0,1,2,3

R' = alkyl, aryl, vinyl, chloralkyl, etc.

R = methyl, ethyl, propyl, phenyl, Glycomonomethylether, etc.

Catalyst = acid or base

The second step is the condensation of alkoxysilane into polysiloxane, which has two forms: homofunctional condensation of silanols and heterofunctional condensation involving the silanol group and another functional group. If the hydrolysis is much faster than the condensation and an excess of water is used, the silane is fully hydrolyzed into silanol and homofunctional condensation happens between two silanols. (3-2) If the functional groups are less active in the hydrolysis step, heterofunctional condensation between silanol and another functional group is favored. (3-3,4)

$$2R'_nSi(OH)_{4-n} \xrightleftharpoons{} R'_nSi(OH)_{3-n}OSiR'_n(OH)_{3-n} + H_2O \tag{3-2}$$

$$R'_nSi(OH)_{4-n} + R'_nSi(OR)_{4-n} \xrightleftharpoons{} R'_nSi(OH)_{3-n}OSiR'_n(OR)_{3-n} + ROH \tag{3-3}$$

$$R'_nSi(OH)_{4-n} + HOSi\text{-surface} \rightleftharpoons R'_nSi(OH)_{3-n}OSi\text{-surface} + H_2O \qquad (3\text{-}4)$$

The nature of the catalyst and in particular the pH of the reaction medium has a very pronounced effect on the hydrolysis and the condensation reactions and therefore on the structure of the resulting polymer network. Under acidic conditions (pH < 5) the hydrolysis rate of alkoxysilanes is high relative to the rate of condensation. This leads to a less tightly crosslinked structure. In contrast, a basic environment tends to promote a dense-cluster growth due to a higher condensation rate with respect to hydrolysis (hydrolysis is the rate-limiting step), and colloidal particles are produced[57].

3.1.2 Polycondensation of alkoxysilanes in μ-emulsion

Normal emulsion polymerization is sometimes referred to as 'macroemulsion' polymerization because of the large size of monomer droplets (hundreds of microns) compared to those of a 'microemulsion' (tens of nanometers). Microemulsions (μ-emulsions) are a convenient medium for preparing microgels in high yields and rather uniform size distribution. The name for these special emulsions was introduced by Shulmann et al.[61]. In general a microemulsion may be considered as a thermodynamically stable colloidal solution in which the disperse phase has diameters from 5 to 100 nm.

In a microemulsion solution, each micelle behaves like a separate micro-continuous reactor which contains all the components, i.e. monomer and catalysts from the aqueous phase. Analogous to the latex particles in emulsion polymerization, microgels (μ-gels) formed by emulsion polymerization are distributed in the total available volume, which means μ-gels formed from microemulsion have diameters from 5 to 100 nm. Unlike emulsion polymerization, during the microemulsion polymerization there exist no monomer droplets but only micelles containing monomers and the reaction mixture is optically transparent and in an equilibrium state. The final size of the polymerized μ-gel is basically decided by the Fleet Ratio S:

$$S = \frac{m_{surf}}{m_p} \qquad (3\text{-}5)$$

with m_{surf} and m_p the masses of surfactant and polymer, respectively[63, 64].

Polycondensation of alkoxylsilane in microemulsion appeared to be more complicated. Baumann et al. systematically studied the mechanism of polycondensation of alkoxysilane in microemulsion and the dependence of particle size on the fleet ratio S[65]. Although seemingly analogous to classical polymerization in microemulsion, according to their results polycondensation in microemulsion is obviously different in the growth mechanism of nanoparticles as well as the stabilizing mechanism.

In this thesis, the synthesis of polyorganosiloxane-μ-gels followed the standard procedure introduced by Baumann et al[57]. The polycondensation of alkoxylsilanes was carried out in a surfactant aqueous solution at room temperature, NaOH was used as catalyst to obtain densely compact micronetworks with ~10 nm radius. In this base catalyzed microemulsion polycondensation, benzyldimethyl[2-[2-(p-1,1,3,3-tetramethyl-butyl-phenoxyl)-ethoxy]ethyl]-ammoniumchloride (Fig. 3.1) was used as the surfactant.
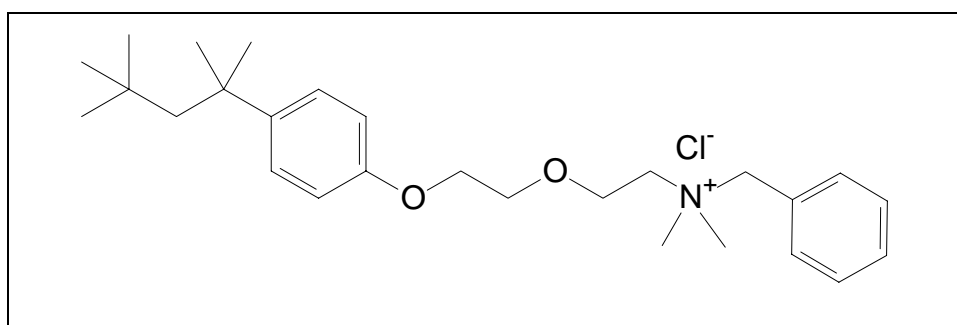

Fig. 3-1 Benzethoniumchloride for polycondensation in microemulsion

This surfactant has two basic elements: a bulky hydrophobic alkyl tail and a very big hydrophilic head group. And benzethoniumchloride can also form a vesicle structure in water, the hydrodynamic radius of this vesicle is around 40 nm[65].

Alternatively to basic catalysts, polycondensation of alkoxysilanes can also be catalyzed by acid. In an acid catalyzed aqueous polycondensation in microemulsion, the surfactant dodecylbenzolsulfonic acid (DBS) itself works as the catalyst.

The degree of functionality of the monomers plays an important role in the degree of crosslinking of the micronetworks and thus influences the final density of the nanoparticles. For silicate particles prepared from the tetraalkoxysilane tetraethoxylsilane (TEOS)[66, 67], the density of the particles can be as high as 2 g/cm^3,

while the density of polyorganosiloxane-μ-gels[57] prepared from trimethoxysilane is around 1 g/cm^3, and the density of the swollen polyorganosiloxane-μ-gels prepared from the mixture of trialkoxysilane and dialkoxysilane can be as low as 0.05 g/cm^3 in solution[57]. Due to the high cross-linking density, the glass transition temperature of silicate particles is so high that it is never reached before decomposition, so they are called "glass beads". Because of its adjustable cross-linking density, the glass transition temperature of Polyorganosiloxane-μ-gels can be varied in a broad range, thus leading to a greatly broadened spectrum of physical properties and potential applications. For instance, a "soft" polyorganosiloxane micronetwork with T_g as low as -115 °C behaves at room temperature like an elastomer[68].

For our particles, we used only trimethoxysilanes as monomer. After polycondensation of trimethoxysilane through a standard co-hydrolysis/condensation procedure (Figure 3-2a,b), the reactant forms a dense compact 3-D network (Figure 3-2c), which, with the help of micelles as template in a microemulsion system, grows into a nanoscopic spherical micronetwork.
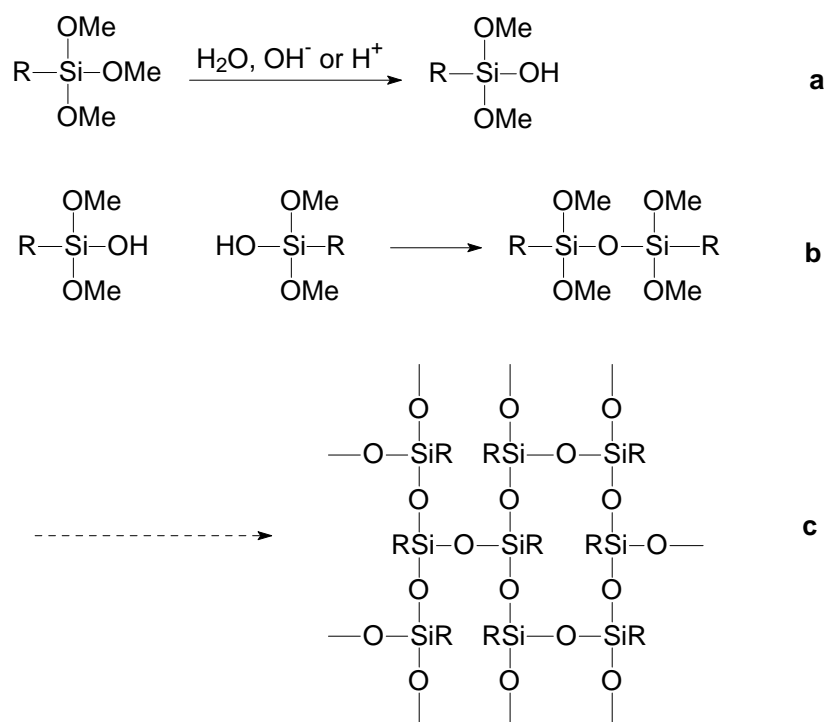

Fig. 3-2 polyorganosiloxane micronetwork formed through the polycondensation of trimethoxysilane. R can be a methyl or chlorobenzyl group.

The aqueous dispersion of the microgels can be stored for a long time without any change of particle size. However, precipitation of the particles irreversibly yields an insoluble material that, under favourable circumstances, could be redispersed as large polydisperse aggregates several hundred nanometers in size.

3.1.3   Redispersible Polyorganosiloxane-μ-Gels

Here I will discuss the procedure of synthesizing a redispersible polyorganosiloxane-μ-gel, which means the particles in aqueous dispersion can be precipitated, dried, and redispersed as single nanoparticles in most organic solvents and monomers like toluene, tetrahyofuran, cyclohexane, chloroform, styrene, and methylmethacrylate. This is achieved by a special "endcapping" procedure previously developed by Baumann et al.[57].

Without this procedure, the particles cannot be redispersed because the aggregation of nanoparticles causes irreversible precipitation. The reason for the aggregation of nanoparticles is the alkoxy group (Si-OR) or silanol group (Si-OH) on the particle surface. (Fig 3.3-1) These groups are chemically reactive. In the presence of catalyst and water, condensation will happen between two particles thus inducing the irreversible aggregation of nanoparticles. In an aqueous dispersion, nanoparticles are stabilized by a surfactant, which prevents the reactive groups of different particles from reacting with each other. During precipitation, this surfactant shell is removed and the distances between particles are very small, so interparticle condensation happens immediately.

To suppress this inter-particle condensation, the particle surface has to be "inerted". This can be realized by the "endcapping" procedure, which is to convert all reactive Si-OH or Si-OR group into "inert" Si-O-SiR'$_3$ groups, with R' typically being a methyl group.

The "endcapping" procedure is schematically described in figure 3-3. After the first step, the microgel can be precipitated and freed from surfactant. Because the reactive groups cannot be totally removed by "endcapping" in the aqueous dispersion, these polyorganosiloxane-μ-gels are still not redispersible after drying. This calls on a second "endcapping": the wet precipitate of microgels was redissolved in toluene and another monofunctional silane was added to further endcap the particle surface. Based

on the standard procedure according to Baumann et al, we used Hexamethyldisilazan (HMN) as the organic phase "endcapping" reagent.

After this second "endcapping" the polyorganosiloxane-μ-gels were then precipitated and dried. The resulting white powder can be stored in a dry state for a long time and redispersed as single particles in different kinds of organic solvents. These redispersible polyorganosiloxane-μ-gels are strictly spherical and have a very narrow size distribution, the particle size varies from 5 nm to 20 nm[57].
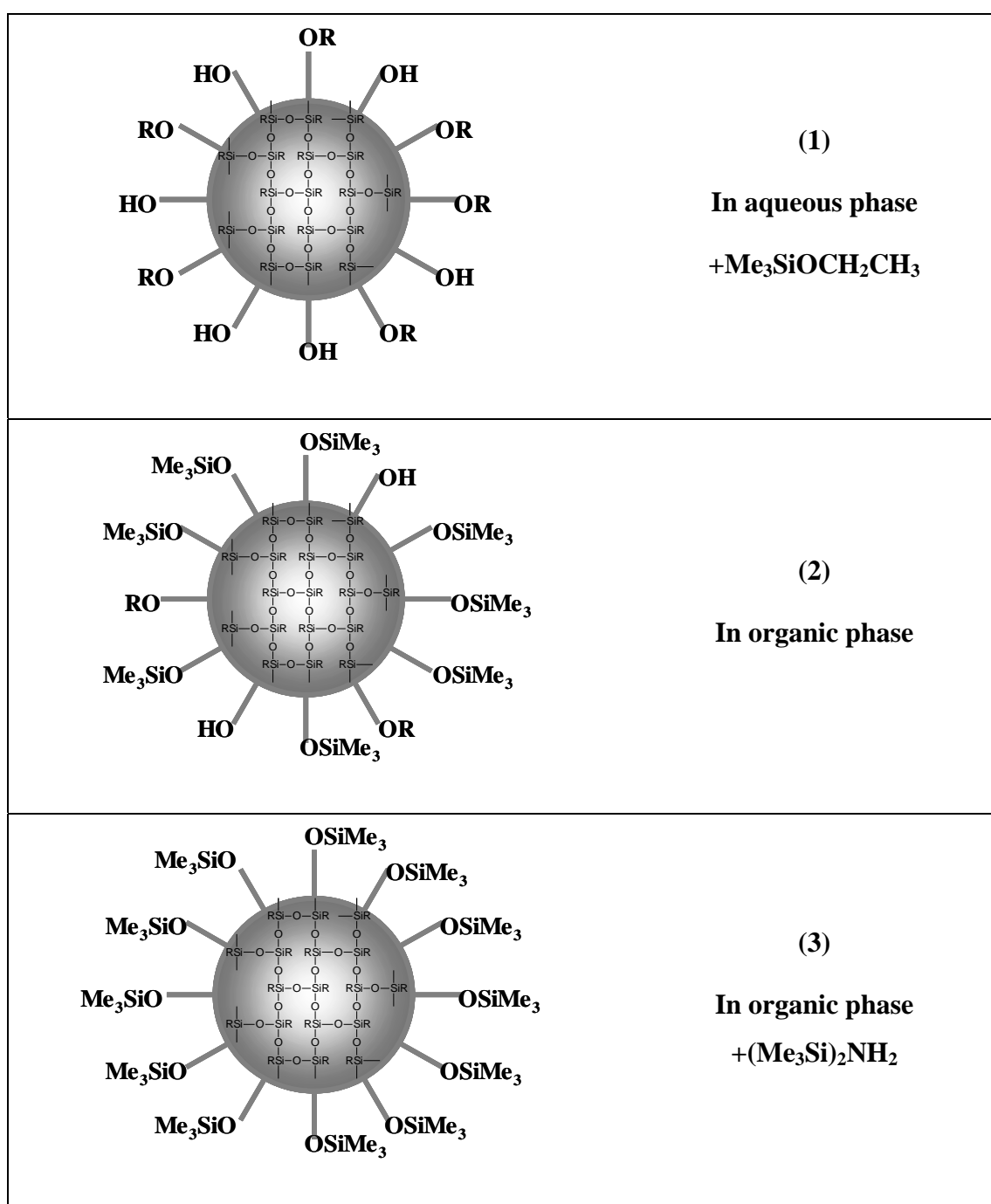
Fig. 3-3 Scheme for the "endcapping" procedure

3.2 Dye-labeled Polyorganosiloxane-μ-gels

The possibility of simple chemical modification is the major advantage of these polyorganosiloxane-μ-gels. A variety of functional groups Si-X (X = H, CH$_3$, CH=CH$_2$, CH$_2$CH=CH$_2$, (CH2)$_3$-OOCCH=CH$_2$, (CH$_2$)$_3$SH, phenyl-CH$_2$Cl) maybe introduced into polyorganosiloxane-μ-gels, using commercially available trimethoxysilanes as comonomers. The surface of polyorganosiloxane-μ-gels may be easily modified using functional monomers as endcapping reagents. In addition, the cross-linking density can be adjusted by co-condensation with dialkoxysilane. Functionalization of polyorganosiloxane-μ-gels can introduce some interesting properties to the nanoparticles. For example, Baumann et al. prepared elastomeric polyorganosiloxane micronetworks by co-condensation of trialkoxysilane and dialkoxysilane[68], Lindenblatt et al. synthesized polystyrene-graft-polyorganosiloxane microgels which showed good compability with polymers[69], Graf et al. introduced different dye molecules into the nanoparticles and studied the behavior of dye-labeled polyorganosiloxane microgels as optical nanoscopic tracers[36], Roos et al. prepared gold-doped microgels using the functionalized polyorganosiloxane microgels as molecular reactors[70, 71], and Emmerich et al. successfully made a hollow organosilicon micronetwork with potential application as drug carriers or dye dispersant[71, 72].

The degree of functionality for a fully functionalized polyorganosiloxane-μ-gel can be very high. In the extreme case, each monomer unit may bear one functional group, and a typical micronetwork 10 nm in size with M$_w$ = 2×10^6 g/mol may contain in the order of 30,000 functional groups[68]. This means the degree of functionality of the nanoparticles can be adjusted in a very broad range.

In this thesis we studied the photochemical properties and the potential applications of dye-labeled polyorganosiloxane-μ-gels. For this purpose, we needed to prepare well defined nanoparticles with a controllable content of photoreactive dye molecules. Figure 3-4 schematically describes the synthesis path of the dye-labeled nanoparticles.

This procedure starts from the poly co-condensation of methyltrimethoxysilane and (chlorobenzyl)trimethoxysilane in surfactant aqueous solution. Sodium hydroxide was used as catalyst to induce the hydrolysis and condensation reaction. The

nanoparticles formed were stabilized in aqueous solution by both surfactant and the hydroxyl groups on the surface. Since the hydroxyl groups and some unreacted methoxy groups left on the surface are still chemically reactive, they will cause interparticle crosslinking and hence the irreversible aggregation of nanoparticles. So it is necessary to remove all the reactive Si-OH or Si-OMe groups by the special "endcapping" reactions described before.
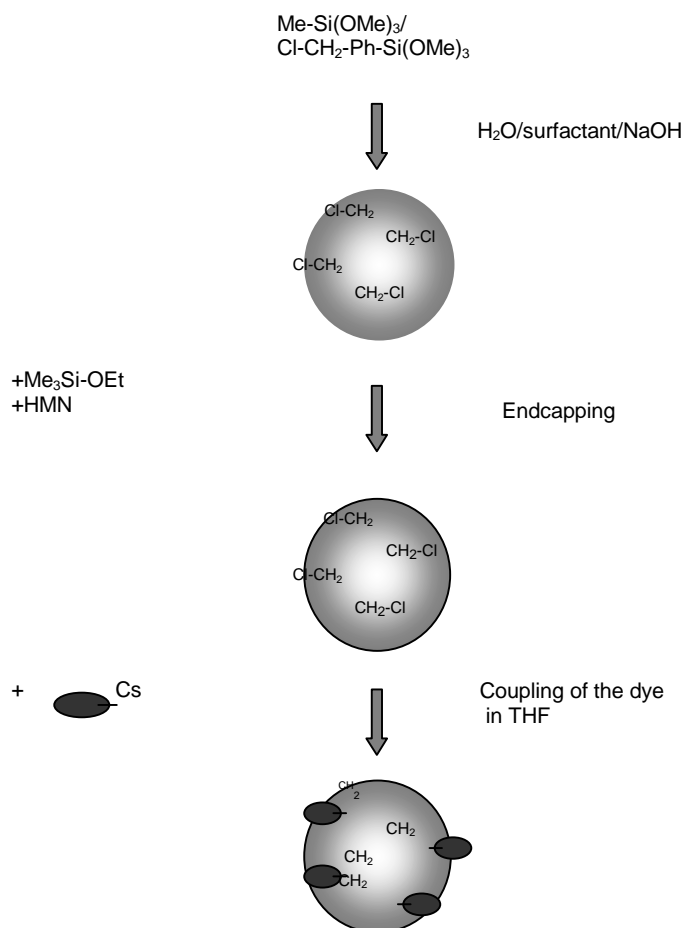

Fig. 3-4 Synthesis path of dye-labeled poly(organosiloxane) nanoparticles, starting with co-condensation of a mixture of methyltrimethoxysilane and (chlorobenzyl)trimethoxysilane. The chloromethyl functions are used to chemically attach dye labels to the particles by an esterification reaction.

Following this procedure, the functional group chlorobenzyl will distribute within the whole nanoparticle including the inner parts, thus the density of dye molecules on the particle surface is difficult to be determined. For the further application, we need the dye-labeled nanoparticle to be photoreactive: it should

undergo inter-particle photodimerization and thus induce cluster formation. Since only dye molecules on the particle surface are effective to induce such cluster formation, we need to introduce the dye preferably on the particle surface. So we modified the previous synthesis path of the polyorganosiloxan-μ-gel developed by Graf et al.. The modified path towards non-functional core-functional shell μ-gels is described in the following picture.
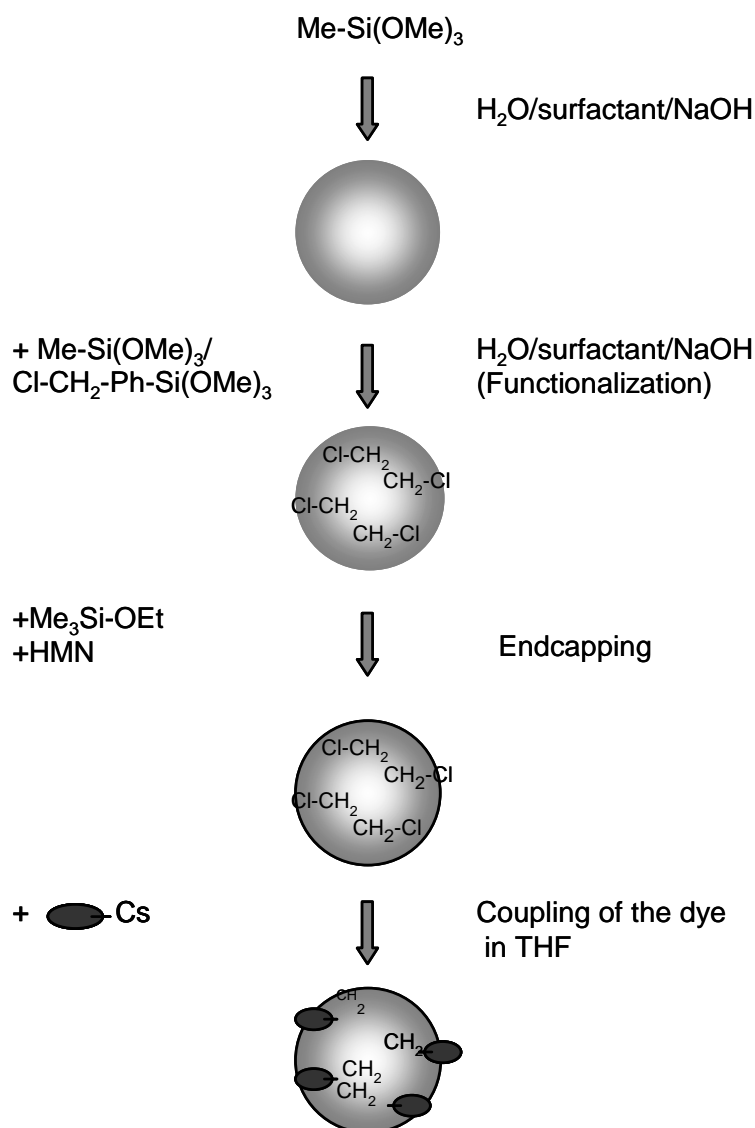

Fig. 3-5 Synthesis path of dye-labeled poly(organosiloxane) nanoparticles, starting with the polycondensation of methyltrimethoxysilane. The (chlorobenzyl)trimethoxysilane was added in the second step to direct the chloromethyl functions mainly to the surface of the particles. The chloromethyl functions are used to chemically attach dye labels to the particles by an esterification reaction.

41

This modified procedure starts from the polycondensation of trimethoxymethylsilane in surfactant aqueous solution with sodium hydroxide as catalyst. After the poly(trimethoxymethylsilane) nanocore was formed, a mixture of trimethoxymethylsilane and trimethoxychloromethylphenylsilane (details see experimental part, chapter 8.2.1) was added. This is to direct the chloromethyl group mainly to the surface of the particle, thus to form a thin shell with functional groups. The nanoparticles then undergo two steps of "endcapping" as described before. The advantage of the modified procedure also includes: i) reduce the consumption of precious trimethoxychloromethylphenylsilane; ii) since it is easier to obtain well-defined and monodisperse nanoparticles through the synthesis of pure trimethoxymethylsilane, the first synthesis step using pure trimethoxymethylsilane leads to higher quality nanoparticles.

Based on Graf's procedure (Figure 3-4) and the modified procedure (Figure 3-5), we obtained chlorobenzyl functionalized polyorganosiloxane-µ-gels Cl-B1 and Cl-B2 (Table 3-1), respectively. The resulting particles (Cl-B2, see table 3-1) with well controlled size and narrow size distribution are shown to be spherical by both AFM and TEM (Figure 3-6). Both of chlorobenzyl nanoparticles (Cl-B1 and Cl-B2, see table 3-1) show identical morphology and size distribution concluded from AFM or TEM image.
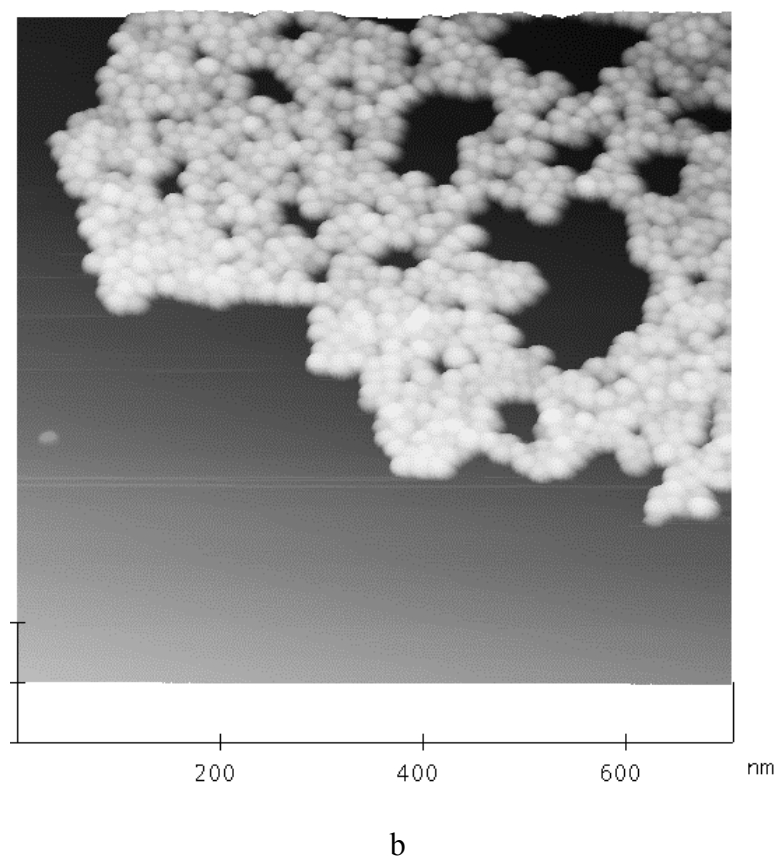

a

b
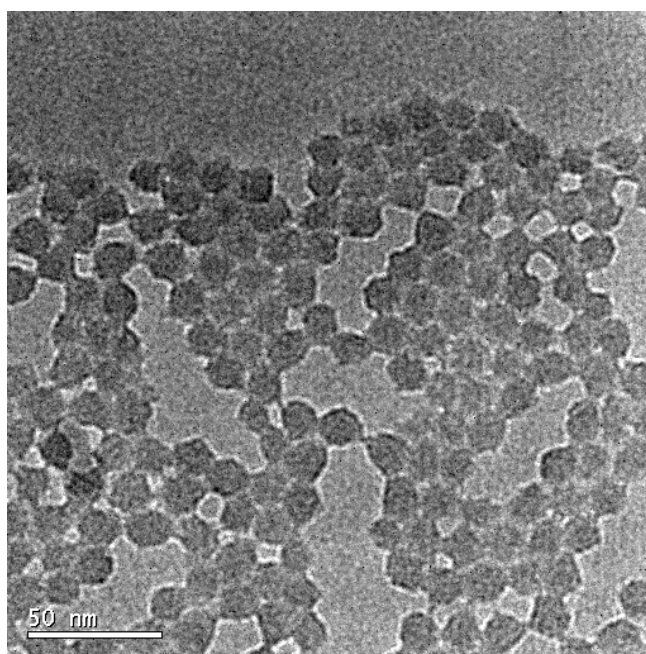
Fig. 3-6 TEM (a) and AFM (b) image of chlorobenzyl functionalized polyorganosiloxane-μ-gels (Cl-B2)

In both the AFM and TEM image, the particle diameter observed is around 20 nm, which is compatible with the results from dynamic light scattering. Molecular weight and hydrodynamic size of the nanoparticles were characterized by Light Scattering, the molecular weight distribution was detected by GPC. Because of the introduction of the chlorobenzyl group, the functionalized polyorganosiloxane shows UV absorption at λ_{max} = 224 nm in cyclohexane solution (Figure 3-7a). With the help of a calibration curve obtained from standard solutions of the monomer (chlorobenzyl)trimethoxysilane (see UV absorption spectrum in figure 3-5b), the chlorobenzyl content of the polyorganosiloxane-μ-gels can be determined by using UV-Vis spectrometry. (Table 3-1)
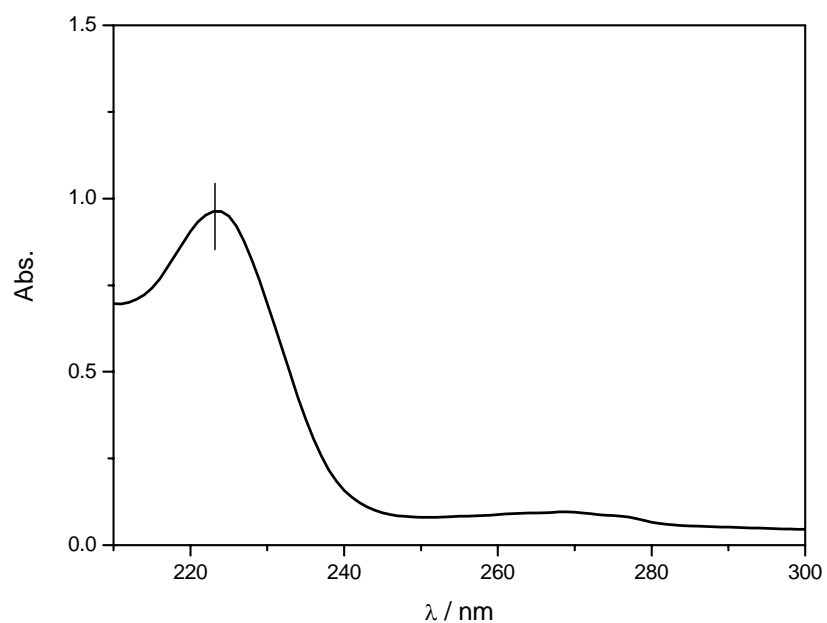
Fig. 3-7a UV Spectrum of chlorobenzyl functionalized polyorganosiloxane-μ-gels in cyclohexane. (optical path length is 10 mm)
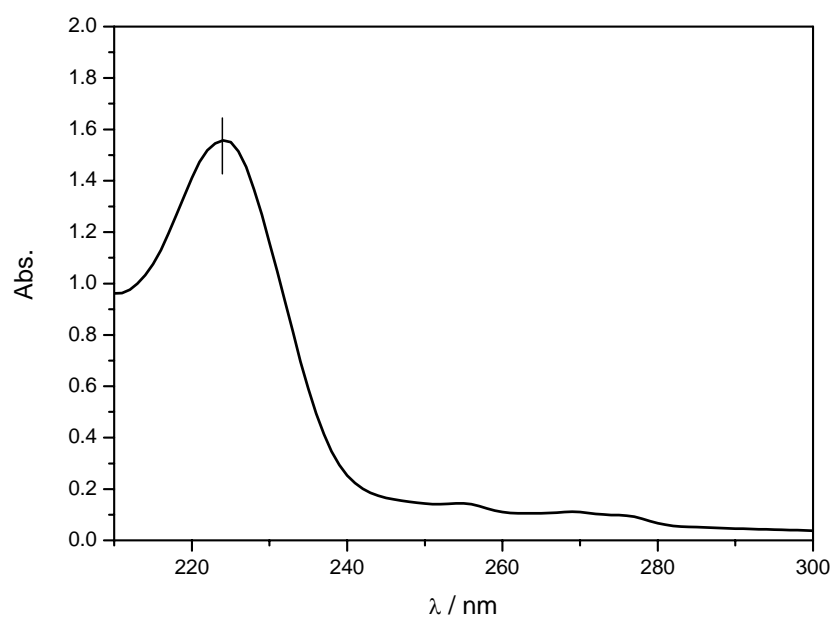

Fig. 3-7b UV Spectrum of (chlorobenzyl)trimethoxysilane in cyclohexane. (optical path length is 10 mm)

Table 3-1 Characteristics of the chlorobenzyl-functionalized microgels

Sample No.	R_h (nm)	M_w (10^{-6} g/mol)	M_w/M_n	Cl-B content (groups/particle)
CI-B1	9.8	2.3	1.10	2.23×10^3
Cl-B2	9.6	2.0	1.06	0.33×10^3

The dye labels (figure 3-8) are chemically coupled onto the functionalized microgels by an esterification of the cesium salt of the chromophores with chlorobenzyl groups of the microgel in tetrahydrofuran solution. Due to their interesting photodimerization reaction, we have chosen coumarin 343, (7-coumaryloxy) acetate (**coumarin**) and p-nitro cinnamate (**cinnamate**) to label the nanoparticles. Because the chlorobenzyl groups are mainly distributed on the surface of the nanoparticles, the dye labels are coupled onto the surface of the particles accordingly.

a): Coumarin 343

b): (7-coumaryloxy)acetate

c): p-nitrocinnamate
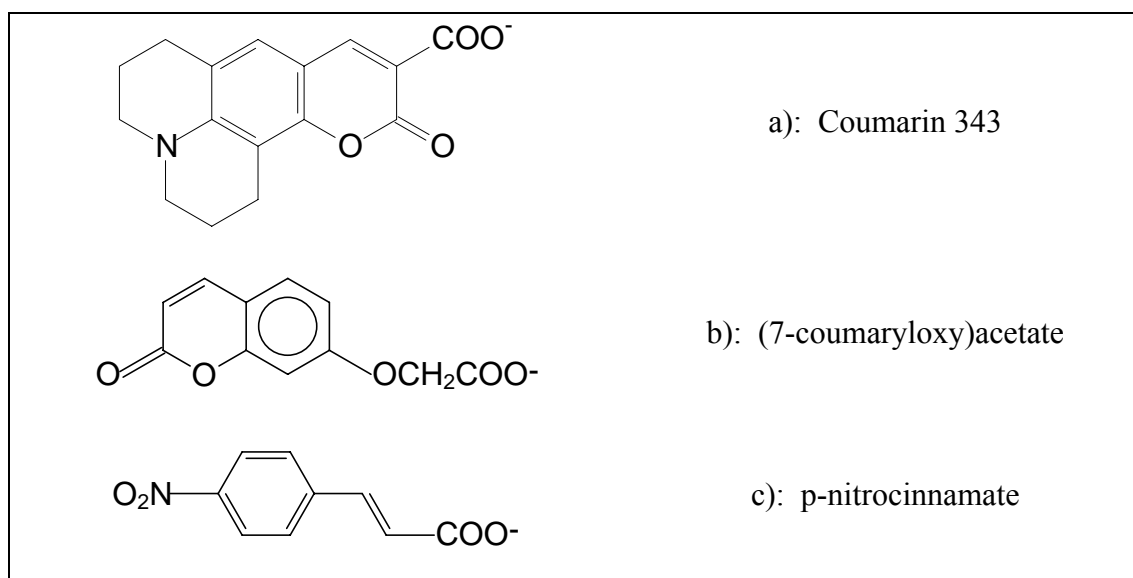
Fig. 3-8

3.2.1 Coumarin 343 labeled polyorganosiloxane-μ-gel

The photolabel coumarin which shows dimerization upon irradiation with UV light has been widely used. Coumarin 343 labeled polyorganosiloxan-μ-gels have already been studied by Graf et al. and interesting photoinduced cluster formation was observed. We also chose coumarin 343 as the first dye and tried to explore the

possibility of reversible cluster formation of coumarin labeled particles. Before the labelling reaction, the cesium salt of coumarin 343 was obtained by reacting the commercially available coumarin 343 acid with stoichiometric amount of cesium carbonate. Then the dye was attached to the polyorganosiloxane nanoparticles through esterification of the cesium salt with chlorobenzyl groups of the microgel in tetrahydrofuran solution.
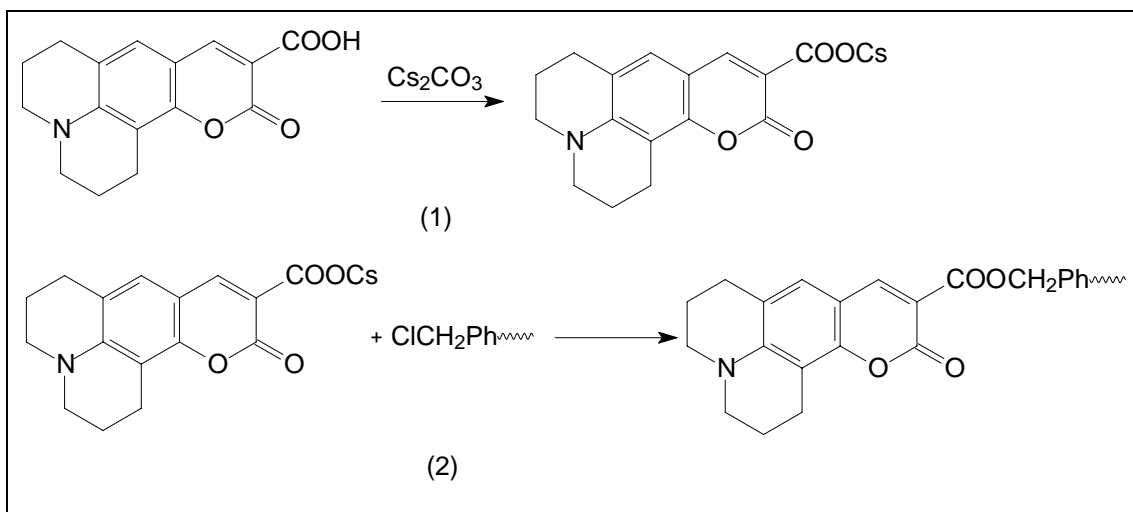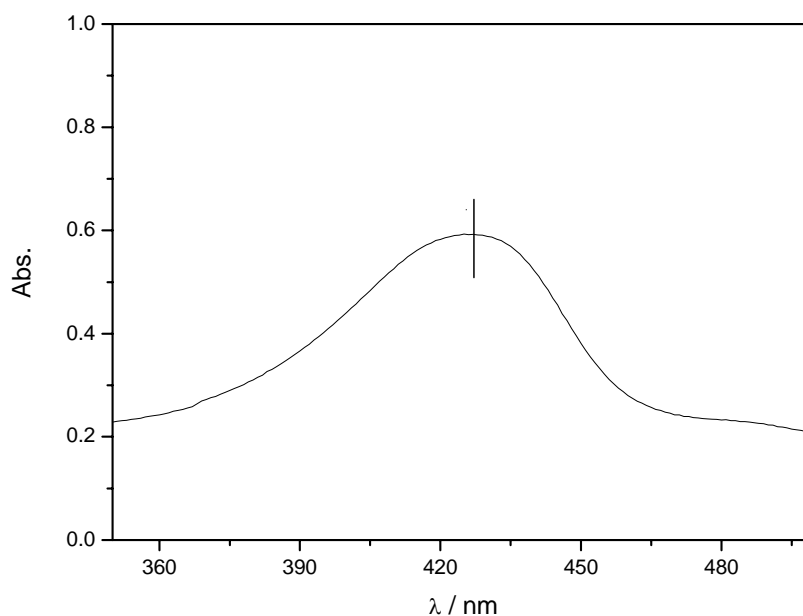

Fig. 3-9

Fig. 3-10a UV/vis-absorption spectrum of coumarin 343 labeled poly(organosiloxane) nanoparticles in THF. (Optical path length: 10mm).

The UV-vis absorption spectrum in figure 3-10a shows the UV absorption peak (λ_{max} = 429 nm) of coumarin labeled nanoparticles. The dye content of the coumarin 343 labeled microgels was determined by comparison of their absorption in solution with the absorption of standard solutions of a model compound (Benzyl ester of coumarin 343) using UV-vis spectrometry. The UV absorption spectrum of the model compound (benzyl ester of coumarin 343) and of coumarin 343 labeled particles are almost identical (see figure 3-10a,b). Therefore, the molar extinction coefficients of Ethyl (7-coumaryloxy)acetate and coumarin labeled particles should be identical within experimental error.
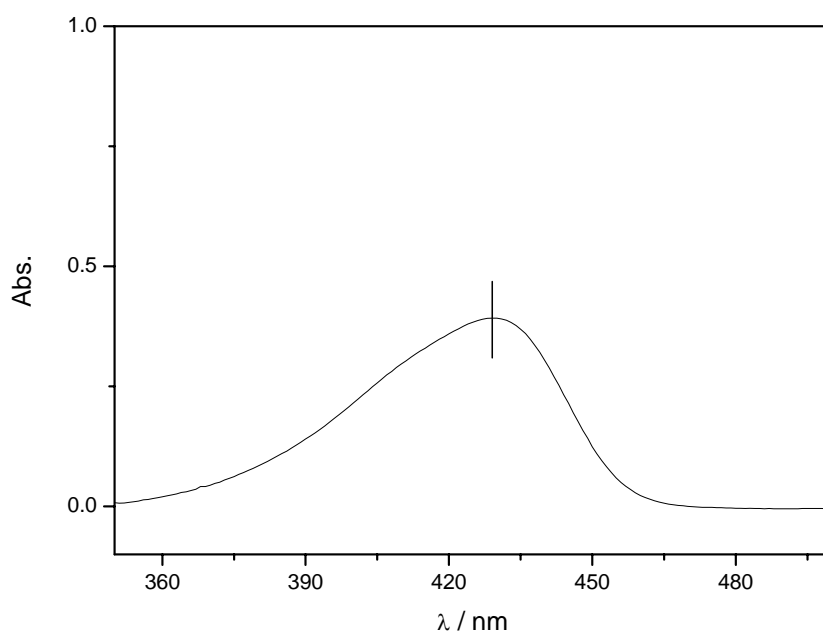

Fig. 3-10b UV/vis-absorption spectrum of benzyl ester of coumarin 343 in THF. (Optical path length: 10mm).

Table 3-2 gives the hydrodynamic radius and the label content of the coumarin 343 labeled polyorganosiloxane nanoparticles. The labeled particles have a higher hydrodynamic radius compared to the none-labeled precursors, which was attributed to the particle aggregation caused by undesired and unavoidable photodimerization during the handling of dye-labeled samples (e.g. precipitation process and weighing process).

Table 3-2 Characteristics of the coumarin labeled microgels

Sample No.	chlorobenzyl microgels	R_h (nm)	No. of labels per particle/ No. of Cl-B per particle
Cou343p	Cl-B2	15	170/330

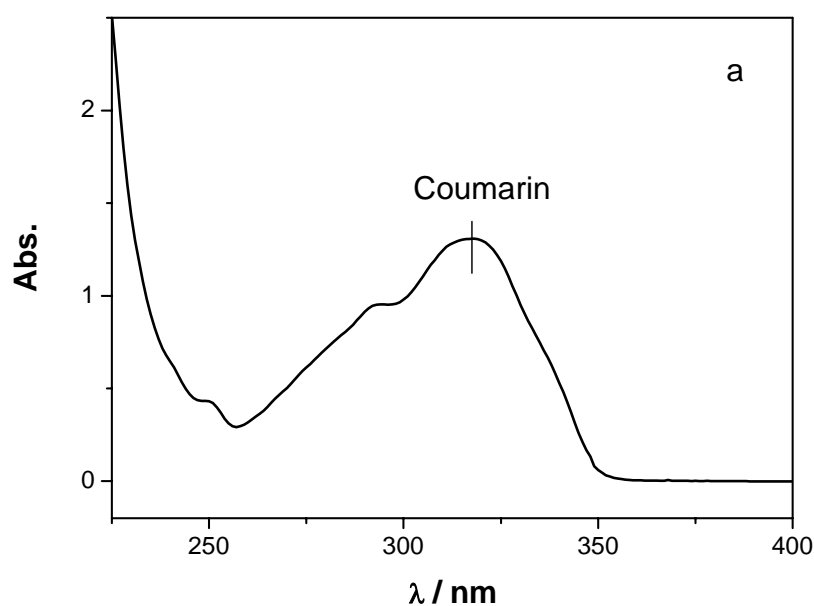### 3.2.2   **Coumarin labeled polyorganosiloxane-μ-gels**

Since our goal is to realize a reversible photoinduced cluster formation, chemical dyes which undergo reversible photodimerization are extremely interesting to us. Chujo et al and Chen et al reported the reversible photodimerization of (7-coumaryloxy)acetate (**coumarin**), which inspired us to label our polyorganosiloxane-μ-gels with this coumarin and find out the resulting photochemical properties.

Fig. 3-11

48
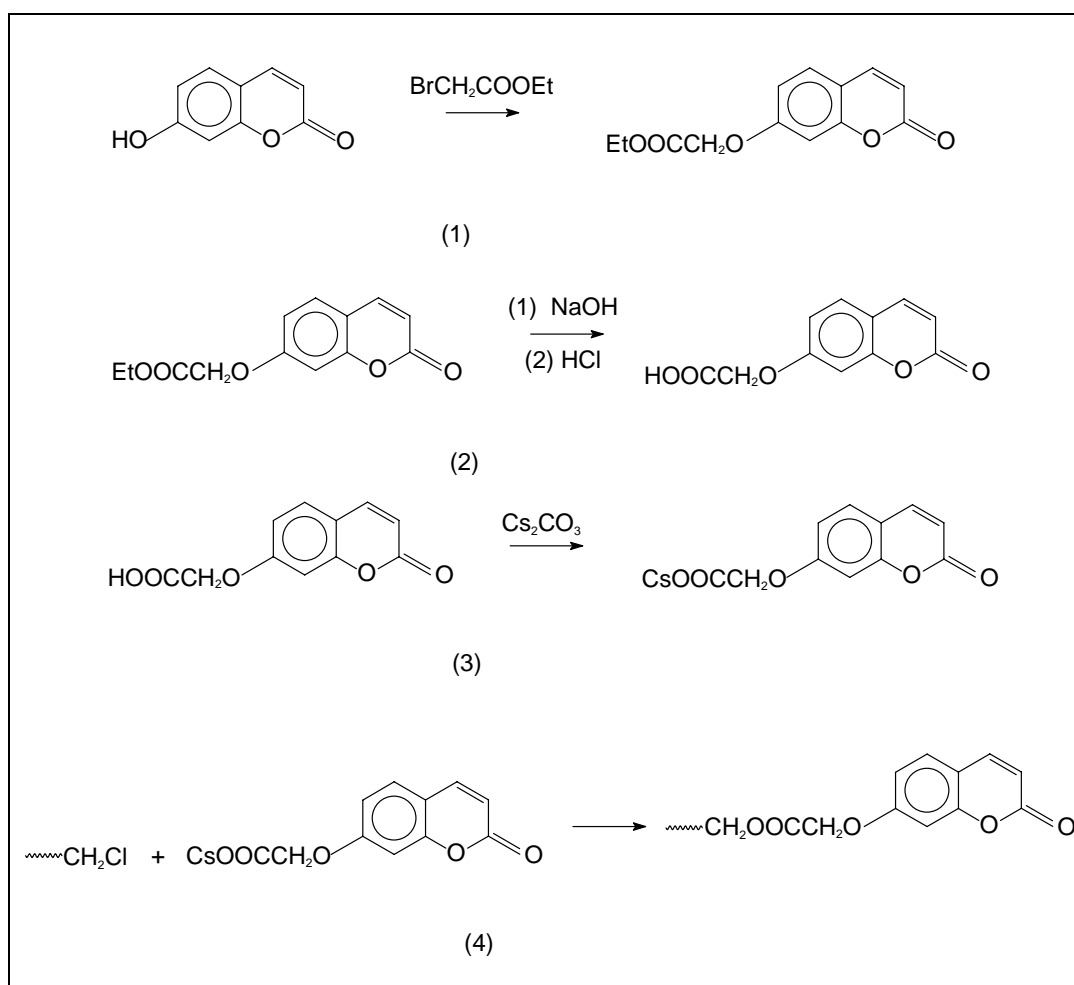
The synthesis of (7-coumaryloxy)acetate labeled particles is shown in figure 3-11: First the commercially available 7-hydroxycoumarin was reacted with ethyl bromoacetate to form ethyl (7-coumaryloxy)acetate. Second, the ester was cleaved to obtain (7-coumaryloxy)acetic acid. In the third step, the cesium salt of this dye was obtained by reacting the carboxylic acid with stoichiometric amount of cesium carbonate. The last step was to couple the dye onto the organosilicon particle through the standard procedure of esterification of the cesium salt of (7-coumaryloxy)acetate with chlorobenzyl groups of the microgel in tetrahydrofuran solution.

After 1st, 2nd and 3rd step, the chemical products were identified by using NMR to make sure the desired chemical structure was obtained (experimental part 8.2.2.2).

The UV-vis absorption spectrum in figure 3-12a shows the UV absorption peak (λ_{max} = 318 nm) of coumarin labeled nanoparticles. The dye content of the coumarin labeled microgels was determined by comparison of their absorption in THF solution with the absorption of standard solutions of the model compound Ethyl (7-coumaryloxy)acetate using UV-vis spectrometry. Ethyl (7-coumaryloxy)acetate has an almost identical UV absorption spectrum (see figure 3-12b) as coumarin labeled particles. Therefore, the molar extinction coefficients of Ethyl (7-coumaryloxy)acetate and coumarin labeled particles should be identical within experimental error.
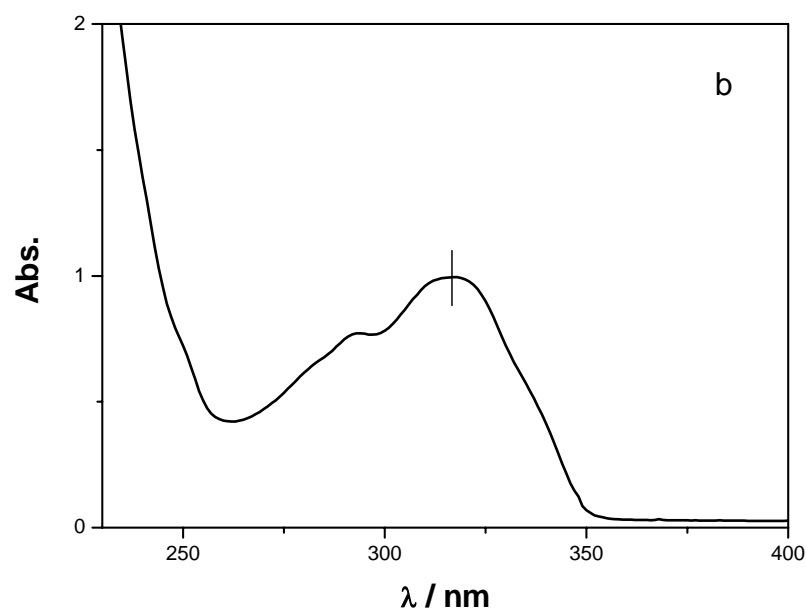
Fig. 3-12b UV/vis-absorption spectrum of a:) coumarin labeled poly(organosiloxane) nanoparticles and b:) Ethyl (7-coumaryloxy)acetate in THF. (Optical path length: 10mm).

Table 3-3 Characteristics of the coumarin labeled microgels

Sample No.	chlorobenzyl-microgels	R_h (nm)	No of labels per particle/ No. of Cl-B per particle
Cou0303	C1-B2	10.4	136/330

The hydrodynamic size of the coumarin labeled particles was measured by dynamic light scattering. The hydrodynamic radius and label contents of the coumarin labeled polyorganosiloxane nanoparticles are given in Table 3-3. The similar size of the functionalized particle before and after dye-labelling shows that no considerable aggregation happened during the labelling reaction.

3.2.3 Cinnamate Labeled polyorganosiloxane

Cinnamate is another photoreactive dye which received much attention. The revesible photodimerization of p-nitrocinnamate was reported by Zheng et al[73]. Since p–nitrocinnamate acid is commercially available, the synthesis procedure of cinnamate labeled microgels is relatively simple. (Figure 3-13)
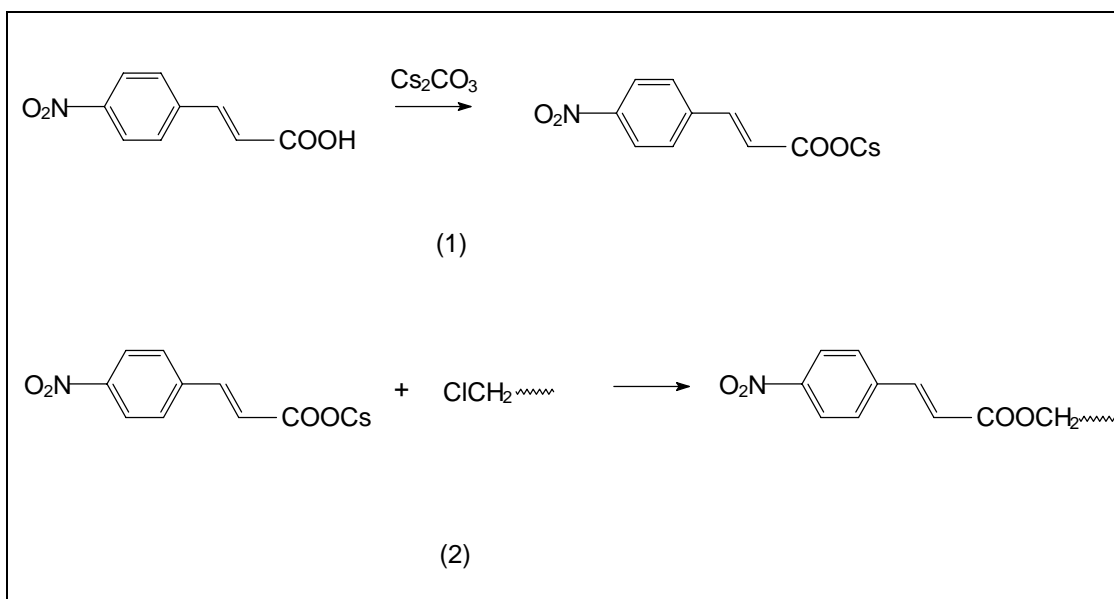
Fig. 3-13

The first step of this synthesis is to obtain the cesium salt of p-nitro cinnamate by reacting the p-nitrocinnamate acid with stoichiometric amount of cesium carbonate. This transfer of p-nitrocinnamate acid to its cesium salt was confirmed by NMR (experimental part 8.2.2.1).

Then the dye was coupled onto the polyorganosiloxane nanoparticles through esterfication of the cesium salt p-nitrocinnamate with chlorobenzyl groups of the microgels in tetrahydrofuran solution. By reacting the chlrobenzyl functionalized nanoparticles (Cl-B1 or Cl-B2, depending on the required dye content) with different amounts of p-nitrocinnamate cesium salt (see experimental part 8.2.2), we obtained cinnmate labeled polyorganosiloxane nanoparticles with different dye contents shown in Table 3-4.

The UV absorption peak of cinnamate labeled nanoparticles (Figure 3-14) is $\lambda_{max} = 302$ nm. Instead of using UV-standard-spectra as before, the dye content of these cinnamate-labeled particles was measured by elemental analysis of nitrogen because the synthesis and purification of model compound p-nitrocinnamate benzyl ester is difficult. Dynamic light scattering was used to measure the hydrodynamic radii of the labeled particles. The results show that at high dye content, the particles have a higher hydrodynamic radius compared to the non-labeled precursors, which was attributed to the particle aggregation caused by undesired and unavoidable

51

photodimerization during the handling of dye-labeled samples (e.g. precipitation process and weighing process). At lower dye content, this undesired photodimerization was negligible, and the particle size basically remained unchanged. (Table 3-4)
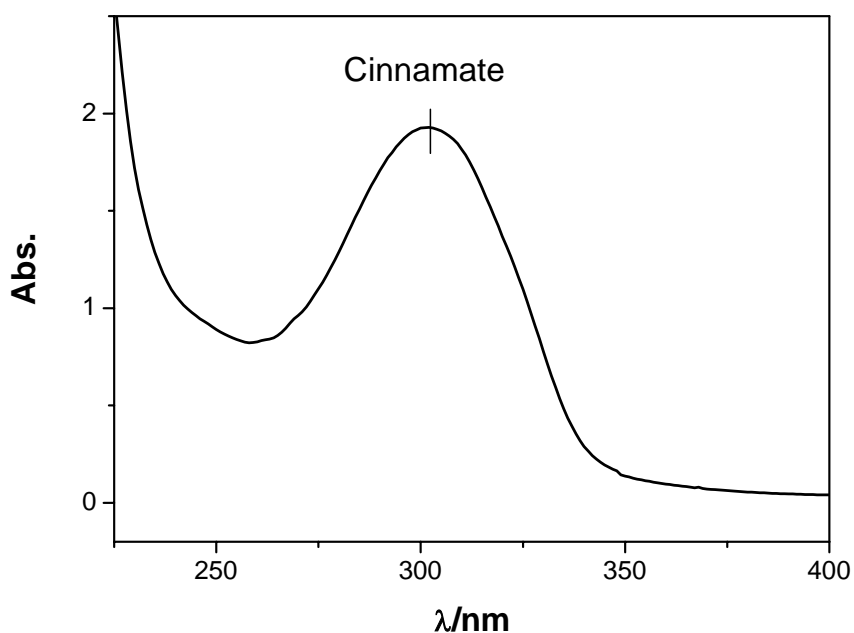

Fig. 3-14 UV-vis absorption spectrum of cinnamate labeled poly(organosiloxane) nanoparticles in THF (C=1g/l). (Optical path length: 10mm).

Table 3-4 Characteristics of the cinnamate labeled microgels

Sample No.	chlorobenzyl-microgels	R_h (nm)	No of labels per particle
Cin01	Cl-B1	18.2	505
Cin02	Cl-B1	15.3	400
Cin03	Cl-B1	15.1	220
Cin04	Cl-B2	10.4	150

52

4 REVERSIBLE CLUSTER FORMATION INDUCED BY INTERMOLECULAR PHOTODIMERIZATION OF NANOPARTICLES

The formation of clusters of nanoscopic colloidal particles in solution as a result of interparticle attraction as well as the structure of these aggregates play a very important role concerning the properties of many technical materials. On the other hand, controlled cluster formation, for instance using reversible photoinduced aggregation as presented in this paper, could also be used to adjust the properties of the colloidal dispersion itself. In addition, new and interesting supramolecular structures can be prepared via a well-defined and controlled aggregation process.

Here, it should be noted that the formation of colloidal clusters in practice is a rather complicated process which is not yet perfectly understood. Also, most cluster formation processes lead to rather polydisperse and also quite open (= low fractal dimension) structures. In case of an irreversible diffusion-controlled aggregation mechanism, the fractal dimension of the clusters ($M(R) \propto R^{f}$, where f is the fractal dimension, $M(R)$ the total mass of the cluster and R the cluster size[74, 75], f = 3 for compact three-dimensional objects) is f < 2.0. Computer simulations of the aggregation of compact spherical particles even yielded much lower fractal dimensions 1.25 < f < 1.5[76]. This corresponds to a rather non-compact structure of the aggregates. On the other hand, reversible aggregation which allows for the rearrangement of particle positions within a formed cluster results in a much more compact structure. Here, computer simulations predict fractal cluster dimensions of about 2.4[20]. Also, according to some simulations partially reversible cluster formation mechanisms seem to lead to much more uniform aggregates in contrast to the irreversible process[22]. We therefore conclude that reversible cluster formation indeed should provide a synthetical route to well-defined rather compact supramolecular structures built from individual nanoparticles. Here, it would be highly desirable to arbitrarily control the rate of cluster formation and the reversibility for a given system. This is quite simple to realize in a computer "experiment"[19], but not at all as easy in a real chemical system.

Some interesting practical examples for reversible aggregation processes of nanoscopic molecules already are found in the literature. For example, particles with a surface modified by DNA show particle aggregation in solution upon addition of the complementary RNA[77]. Further, this aggregation can be reversed by simply changing the sample temperature. Alternatively, the aggregation process can be controlled by employing a suitable reversible photoreaction. Whereas to our knowledge no such examples exist for compact spherical nanoparticles, there are found some papers treating the reversible photo-crosslinking of polymer chains: the reversible 2+2 cycloaddition of the photolabel coumarin has been used to form a gel of crosslinked polyacrylate chains[78]. The gel formation could be reversed by irradiating the sample with UV-light of shorter wave length than used for the gel formation. In a similar way, interpenetrating network structures of coumarin-labeled poly(2-methyl-2-oxazolin) and a polycondensate of tetramethoxysilane have been prepared[79]. Reversing the photodimerisation, the poly(2-methyl-2-oxazolin)–network could be broken up, and dissolution of the single polymer chains lead to the formation of a nano-porous SiO_2-polycondensate. Finally, we would like to mention that also C60-fullerene in its protonated state has been used as a reversible photocrosslinker, as has been demonstrated successfully for fullerene-labeled polyvinylalcohol[80]. In contrast to these interesting examples, our goal is the preparation of reversibly crosslinked supramolecular aggregates from compact nanospheres. Here, we are not only interested in understanding the general mechanism of cluster formation in more detail by employing an experimental system which allows us to control the aggregation rate and the reversibility. We also want to explore the suitability of our new system as an opto-chemical switch, i.e. upon irradiation with uv-light the properties of a colloidal dispersion (e.g. optical transparence, electric conductivity, viscosity etc.) can be adjusted in a well-defined way.

Previously, in our group has been found a way to prepare highly crosslinked poly(organosiloxane) nanospheres (particle radius about 10 nm) which could be labeled chemically with a variety of organic dye molecules[36]. For particles labeled with coumarin 343, the authors have found the formation of clusters of radius much larger than 100 nm if a solution of the particles was irradiated with uv-light[37]. This was the first work showing the formation of colloidal clusters as a result of an optically controlled aggregation process. Unfortunately, the cluster formation of this

previous system proved to be irreversible. Therefore, as presented in this thesis we have prepared two new types of poly(organosiloxane) nanospheres with photolabels which, according to literature, should definitely undergo a reversible photodimerization[73, 81] (see chapter 3).

Clusters have been formed by irradiation of the particles in dilute THF or toluene solution, using irradiation time and irradiation wavelength regime as adjustable parameters. By quantification of the cluster size with dynamic light scattering, we will show that our new system indeed is capable of photo-reversible cluster formation.

4.1 Reversible Photodimerization [82-85]

The chemistry of photodimerization extends back to 1867, when the first synthetic photodimer was obtained by the German chemist Fritzsche[86, 87], who observed the formation of an insoluble substance when a benzene solution of antharacene was irradiated with sunlight. The dimeric nature of the photoproduct was established in 1891 by molecular weight determination, and the correct structure (Figure 4-1) was proposed before the turn of the century by Charles Linebarger[88]. This structure was verified by recent three-dimensional X-ray crystal structure data. Remarkably, this dianthracene can regenerate to anthracene upon melting, which indicated the reversibility of this dimerization.
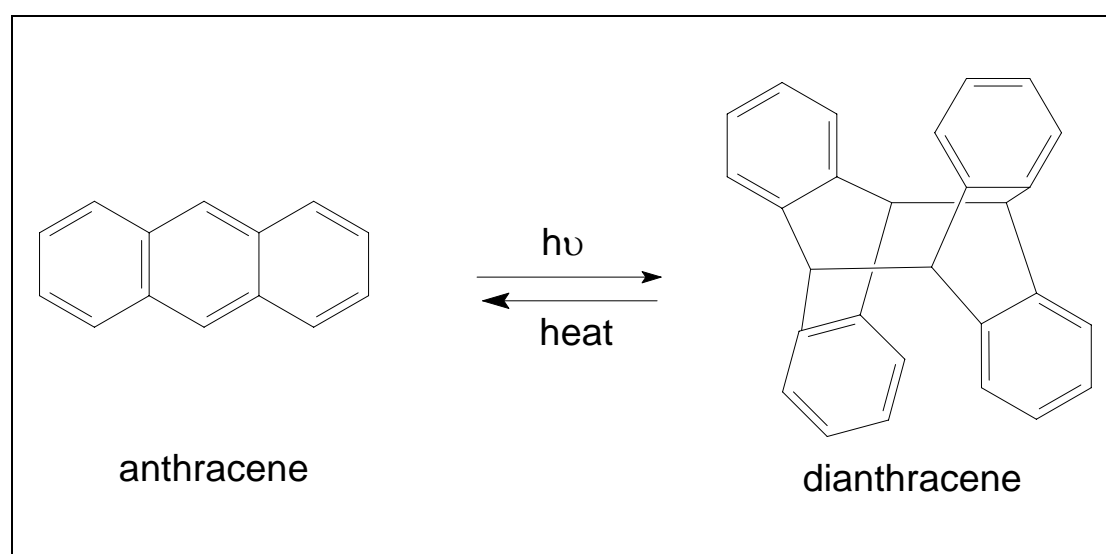

Fig. 4-1 Photodimerization of Anthracen

The mechanism study on the photochemical formation of this dimer commenced as early as 1905. In particular, the photophysics and reversibility of the reaction were studied during the following 50 years.

The classification of cycloadditon reactions follows the scheme of Woodward and Hoffmann[89], emphasized more recently by Turro[90]. By definition, a m,n-cycloaddition reaction is a ring-forming reaction of **m** participating electrons of one group to **n** participating electrons of another group. In most cases, new σ–bonds are formed in the products with a corresponding loss of π–bonds in the starting materials:
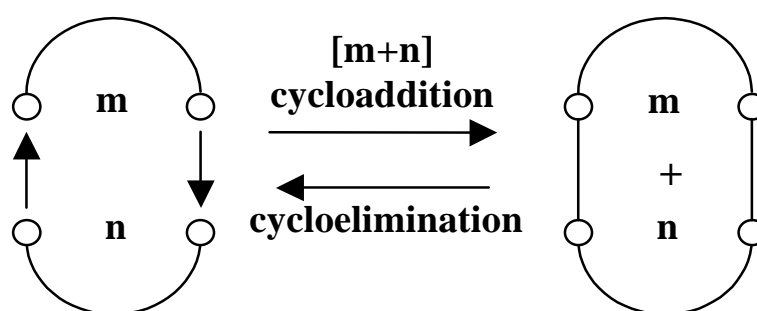

Fig. 4-2 Scheme for cycloaddition and cycloelimination[91]

Using this scheme, a large number of dimerization reactions can be classified into a single model reaction. The most common type of photodimerization involves m = 2 and n = 2 in this classifification scheme ([2+2] cycloaddition reactions). The [2+2] cycloaddition has been found to be extremely versatile, as shown in the photodimerization of a large number of natural products[92], such as thymine (Figure 4-3), coumarin and its derivative, and cinnamate and its derivative. The later two compounds were used in this thesis and their photodimerization will therefore be dicussed in more detail further below.
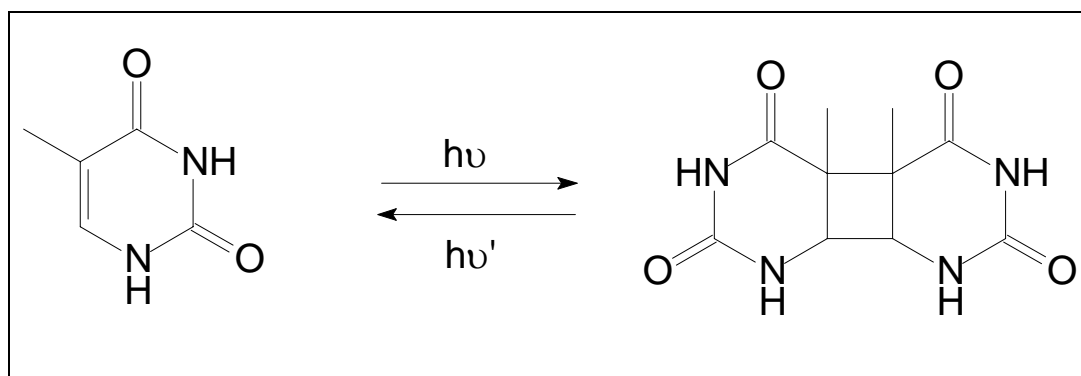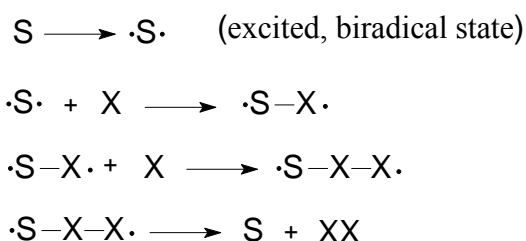

Fig 4-3 Photodimerization of Thymine

Cycloaddition reactions are not confined to [2+2] reactions. The dimerization of anthracene illustrates a case in which electrons from one anthracene molecule react under photochemical excitation with the electrons from another anthrancene molecule to yield the dimeric structure shown in figure 4-1. In this case, m = 4 and n = 4 according to the general classification scheme. So the dimerization of anthracene is an example for a [4+4] cycloaddtion.

A number of photochemical reactions are known in which the rate and yield of the product can be increased by using a chemically unreactive aromatic hydrocarbon in conjunction with an electron-deficient photosensitizer[93]. This effect is called cosensitization. The principle how such photosensitizers work can be explained as following:

$$S \longrightarrow \cdot S \cdot \quad \text{(excited, biradical state)}$$

$$\cdot S \cdot \ + \ X \longrightarrow \ \cdot S{-}X \cdot$$

$$\cdot S{-}X \cdot + \ X \longrightarrow \ \cdot S{-}X{-}X \cdot$$

$$\cdot S{-}X{-}X \cdot \longrightarrow \ S \ + \ XX$$

with S the sensitizer and X the photoreactive molecule.

In a reversible photodimerization cyclobutane can be cleaved, and this bond-cleavage is the result from an electron transfer of the cycloadducts. Since higher energy is required to break a σ-bond than to break a π-bond, photocleavage generally needs UV light of shorter wavelength than needed for the photodimerization. Stereochemistry can effect the ring-cleavage reaction. In case of the cleavage of cyclobutane, either symmetric or asymmetric cleavage could happen (Figure 4-4): for symmetric cleavage, cyclobutane is cleaved between the A-A and B-B bond, and the photodimer is reversed to the original monomers. In asymmetric cleavage cyclobutane is cleaved between the A-B bonds and new monomers are formed, wherefore this photodimerization is not reversible. The cleavage type is influenced either by steric repulsions or other interactions between neighbouring groups[82].
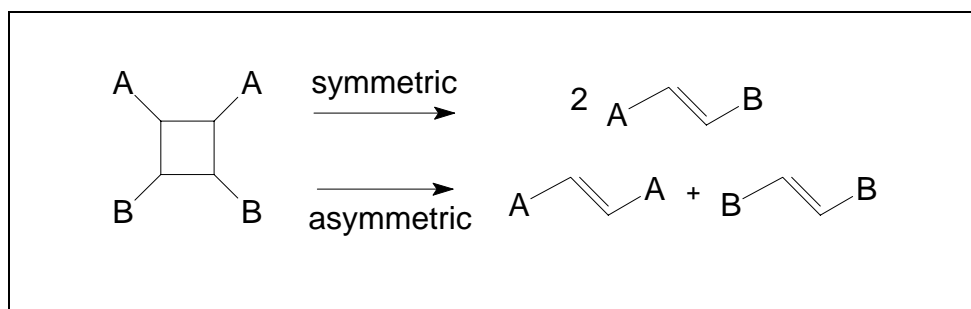
Fig. 4-4 Cleavage of cyclobutane

Strained cyclobutanes undergo cycloreversion when symmetric cleavage happened. Cyclobutane ring cleavage sometimes competes with electron-transfer-sensitized oxygenation[94]. In this case, interception of the open chain radical cation by oxygen leads to the oxygenated product.

4.1.1, Photodimerization of Coumarin derivatives[93, 95, 96]

The structure of coumarin (scheme 4-4) was first reported and the substance itself isolated in the 1820's, recognized as the hay-like sweet aroma of the tonka bean[97]. Since there are more than 800 different derivatives in the coumarin family, the applications of coumarin are manifold.
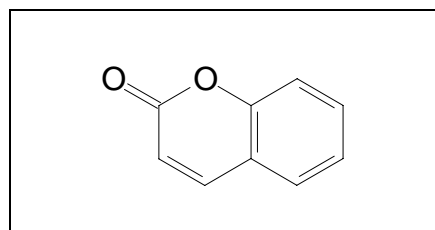

Fig. 4-5 Coumarin

The phododimerization of coumarin was discovered by Ciamician and Silber in 1902[98]. The dimerized product exhibited a melting point of 262 ℃, much higher than the original coumarin's melting temperature of 68-70 ℃. In 1904, Stroem reported a coumarin dimer with a melting point above 320 ℃. The different melting temperatures indicated that the structure of the photodimer is not unique. Later studies proved that there are basically two kinds of coumarin dimer: head-to-head and head-to-tail coumarin dimer. (Figure 4-6) The actual coumarin dimmer formed upon irradiation depends on the combination of light power, solvent, and coumarin concentration. In most cases, the head-to-head addition is favored.
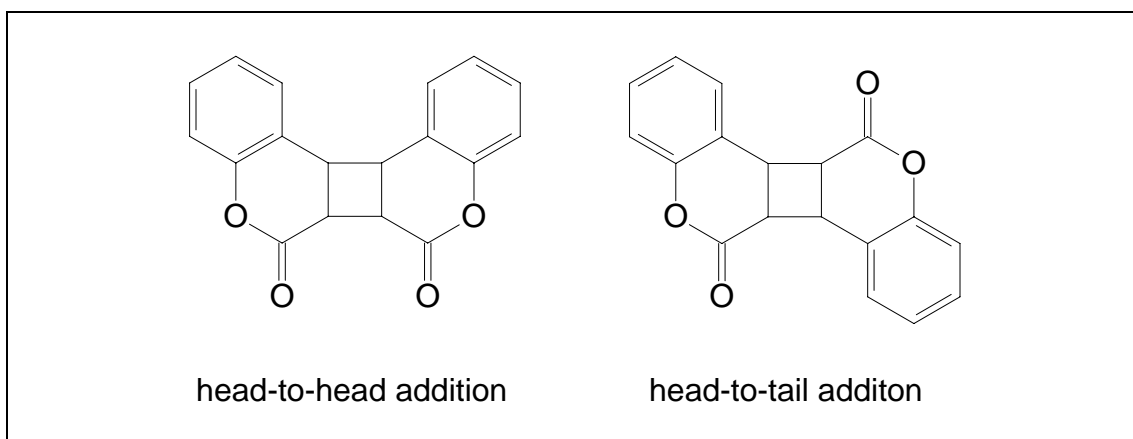
head-to-head addition   head-to-tail additon

Fig. 4-6 Coumarin photodimer

Most of the derivatives of coumarin show the same interesting photodimerization reaction as the basic form of coumarin. The photoinduced cluster formation of coumarin-343 (Figure 3-8a) labeled polyorganosiloxane-μ-gels has been studied by Graf et al[37]. Chujo et al [81]and Chen et al[78, 80] reported the reversible photodimerization of (7-coumaryloxy)acetate (Figure 3-8b) applied to a polymer system. In this thesis, we have studied the properties of nanoparticles labeled with coumarin 343 and (7-coumaryloxy)acetate, respectively.

4.1.2 Photodimerization of Cinnamate Derivatives

Cinnamate exhibits an interesting photochemical behaviour because here the presence of a double bond offers possibilities of dimerization and stereoisomerization[99, 100]. The photocrosslinking property of cinnamates has been broadly utilized in the field of photolithography and the semiconductor industry[101].

Cinnamate is known to undergo trans-cis isomerization and [2+2] cycloaddition upon UV irradiation at wavelengths longer than 290 nm (Figure 4-7). The trans-cis isomerization is favored in the early stage of UV irradiation (Figure 4-7a), and the photodimerization from head-to-head and head-to-tail [2+2] cycloaddition leads to the formation of a cyclobutane ring (Figure 4-7b).

In dilute solution, photodimerization of simple esters of cinnamic acid is inefficient due to very rapid competing trans-cis photoisomerization[102, 103]. The presence of nitro groups has an accelerating effect on the [2+2] cycloaddition process compared to unsubstituted cinnamate groups, which undergo only modestly efficient

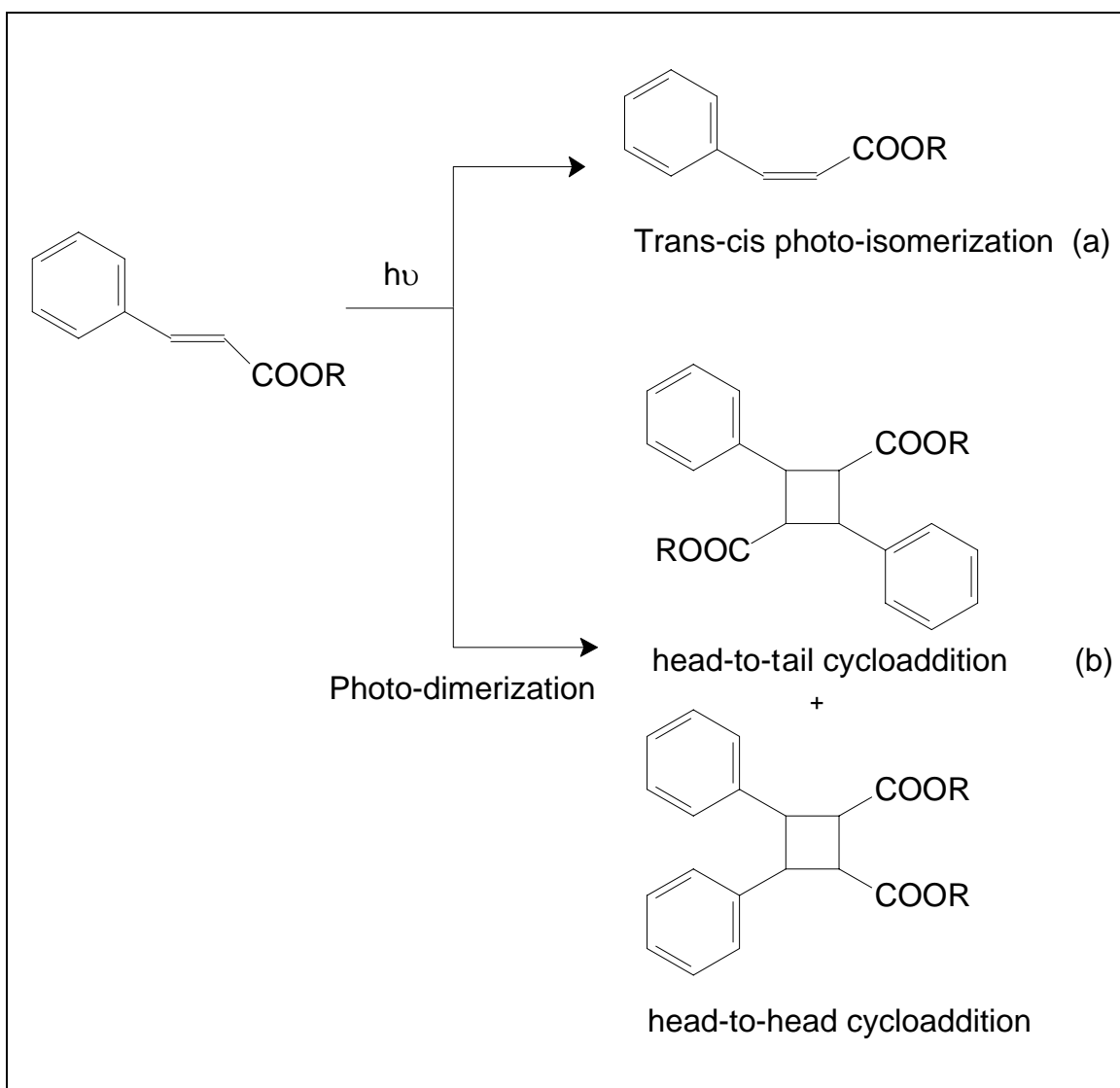photodimerization[73, 104]. So we chose p-nitrocinnamate (Scheme 3-3c) as one of our dye labels.

Fig. 4-7   Photochemisty reaction of cinnamate

4.2 Cluster formation induced by inter-particle photo-dimerization

In chapter 3, we discussed the preparation of coumarin and cinnamate labeled polyorganoslioxane-µ-gels. Both the coumarin derivative and the cinnamate derivative used to label the nanoparticles are typical molecules undergoing photodimerization upon irradiation (Figure 4-8)
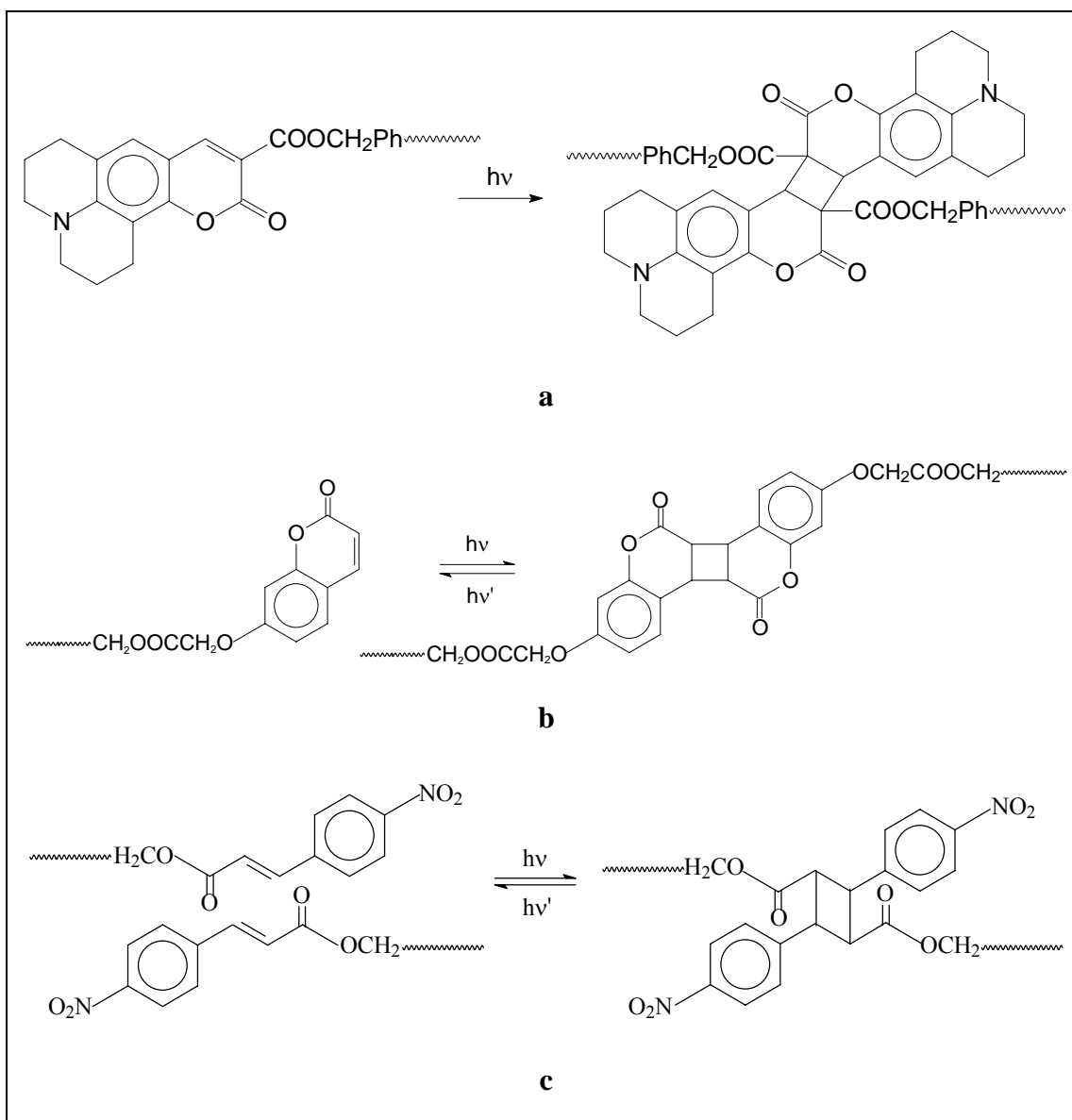
Fig. 4-8 Photodimerization of coumarin 343 (a), (7-coumaryloxy)acetate (b), and p-nitro cinnamate (c) upon irradiation with UV light.

For our dye-labeled nanoparticles, the photosensitive dyes are chemically attached at the surface of the nanoparticle. When these nanoparicles are exposed to suitable UV light, the dye molecules form photodimers. Photodimerization between the dye molecules located at different nanoparticles will cause aggregation of these nanoparticles, leading finally to the formation of clusters (Figure 4-9). If the photodimerization is reversible, we can irradiate the clusters with UV light of a shorter wavelength and the cyclobutane of the dimer will be cleaved, thus destroying the connection between different nanoparticles. Therefore, the clusters are switched back to single particles.
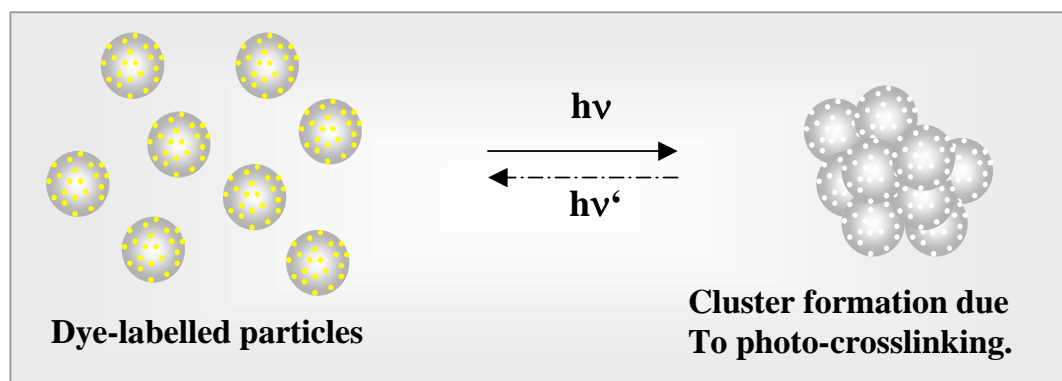
Fig. 4-9 Photo-cross-linking of dye-labeled poly(organosiloxane) nanoparticles by intermolecular photodimerization

As discussed before, head-to-head dimerization of the photo labels is favored in many cases. This process will mostly cause intraparticle crosslinking and no clusters will be formed. However, if we assume the dye is evenly distributed on the surface of the particles, for a nanoparticle of 10 nm with 400 photo labels (the surface area is around 1,256 nm^2 and the area for each label therefore is 3.14 nm^2) the distance between two labels is longer than 1 nm. On the other hand, for a photochemical reaction it is required that the distance between two reacting molecules is only around a few angstrom. As a consequence, intraparticle photodimerization is very difficult and interparticle photodimerization is favored, proceeding due to collisions between the nanoparticles. Most of the samples we investigated have even less than 400 labels per particle (see table 3-2,3,4), so intraparticle photodimerization should not be a problem.

We expect photodimerization to take place if the samples are irradiated with light of wavelength close to their respective absorption maximum, that is 429 nm for coumarin 343, 318 nm for (7-coumaryloxy)acetate (coumarin), and 302 nm for p-nitrocinnamate (cinnamate) labeled particles. On the other hand, cleavage should occur if the clusters are irradiated with light of wavelength about 50 nm shorter than the respective absorption maximum.

A Hg-Xe Lamp was used as the light source for sample irradiation. If you look at the spectral distribution of the light emitted by the lamp (Figure 4-10a) you will find that it provides light of a very broad wavelength range (from 230 nm to longer than 1000 nm).
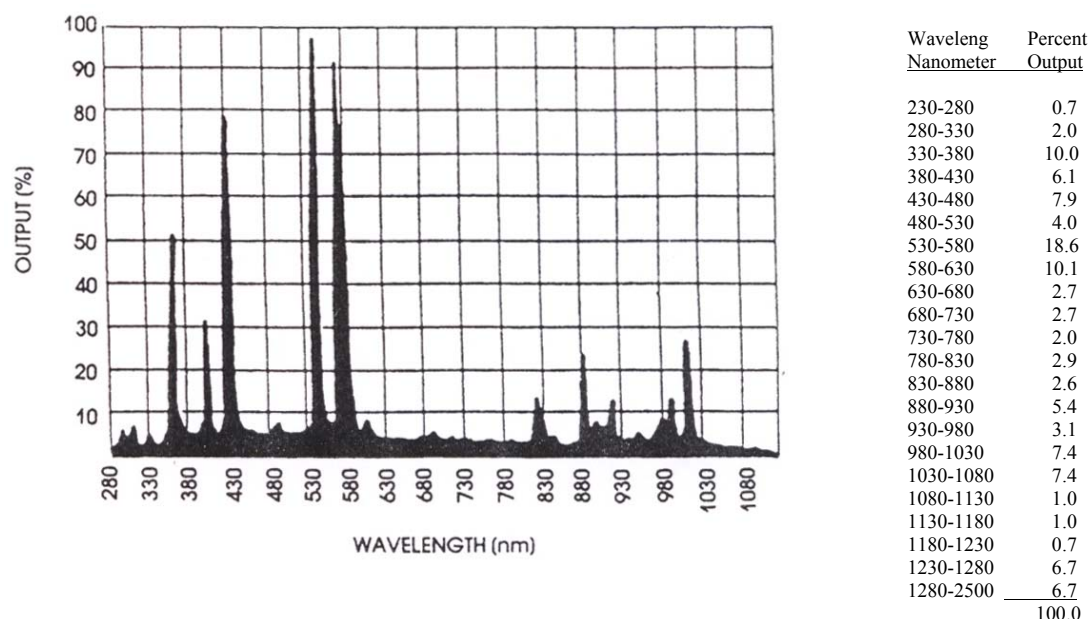
Waveleng Nanometer	Percent Output
230-280	0.7
280-330	2.0
330-380	10.0
380-430	6.1
430-480	7.9
480-530	4.0
530-580	18.6
580-630	10.1
630-680	2.7
680-730	2.7
730-780	2.0
780-830	2.9
830-880	2.6
880-930	5.4
930-980	3.1
980-1030	7.4
1030-1080	7.4
1080-1130	1.0
1130-1180	1.0
1180-1230	0.7
1230-1280	6.7
1280-2500	6.7
	100.0

Fig. 4-10a Spectral distribution of the light emitted by the Hg-Xe lamp used for irradiation in this thesis.
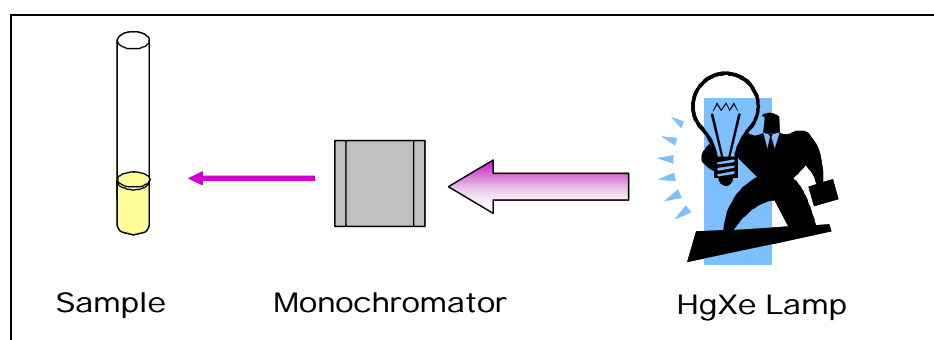

Fig. 4-10b Scheme for irradiation.

The most suitable UV light for photodimerization should have a wavelength close to the absorption maximum of the respective chromophore. Hence, the lamp was equipped with a monochromator, which was used to adjust the light to a suitable irradiation wave length (302 nm for cinnamate labeled particle and 318 nm for coumarin labeled particles). Stock solutions of dye-labeled particles within cylindrical 1 cm Suprasil light scattering cuvettes, filtered previously through a 0.2 μm Millex FGN Teflon filter, were irradiated using this lamp-monochromator combination. (Figure 4-10b)

To investigate the kinetics of photo-cross-linking, the average size of the particles versus irradiation time was characterized by dynamic light scattering (DLS). From the time-intensity correlation function $G_2(q,t)$ obtained in the DLS experiments, using a commercial ALV setup (ALV-3000) consisting of a He-Ne laser (632.8 nm) and ALV-3000 digital correlator, the average hydrodynamic radius was determined[39, 105]. Since the formation of clusters will increase the average hydrodynamic size of the particles in solution, the average hydrodynamic radius should increase during irradiation. By plotting the average hydrodynamic radii of coumarin 343 labeled particles (cou343p, around 170 labels per particle) versus irradiation time (Figure 4-11a), we observed the expected increase of the average hydrodynamic radius which supports the assumed cluster formation via interparticle photodimeriztion. However, the increase in hydrodynamic size is very slow (from 16 nm to 36 nm in 25 hours.), reaching the limit of 36 nm after 25 hours irradiation.
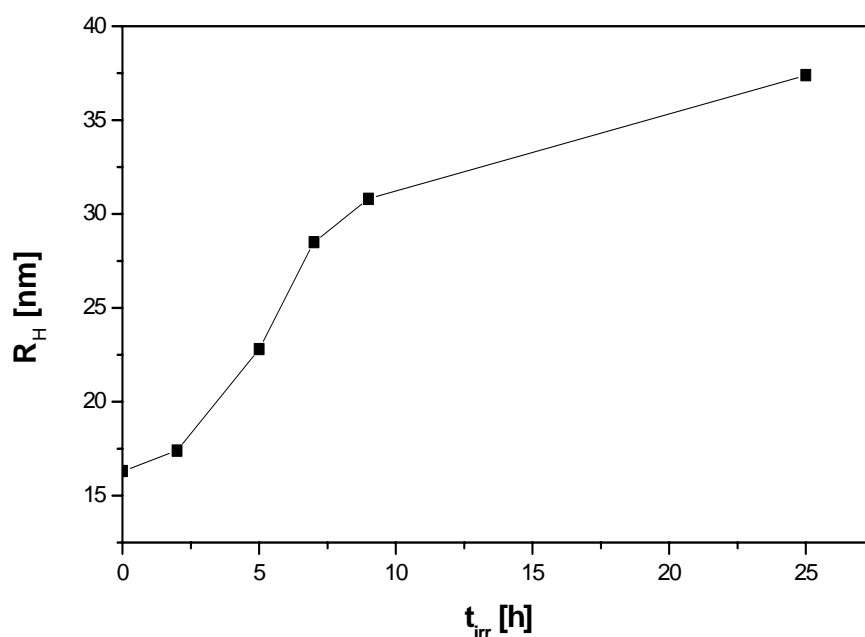

Fig. 4-11a   Change of the average R_h of Cou343p/THF (2g/l) nanoparticles versus irradiation time (light wavelength 426 nm)

The investigation of cinnamate labeled nanoparticles Cin01 (around 500 labels per particle) also yields a change of hydrodynamic size upon irradiation at 302 nm. The plot of hydrodynamic size against irradiation time (Figure 4-12) shows the

hydrodynamic size first increased from 20 nm to 30 nm, indicating the formation of small clusters. The interesting thing is that the hydrodynamic radius of the particles then began to decrease after 6 hours irradiation, implying the possibility of reversible cluster formation.
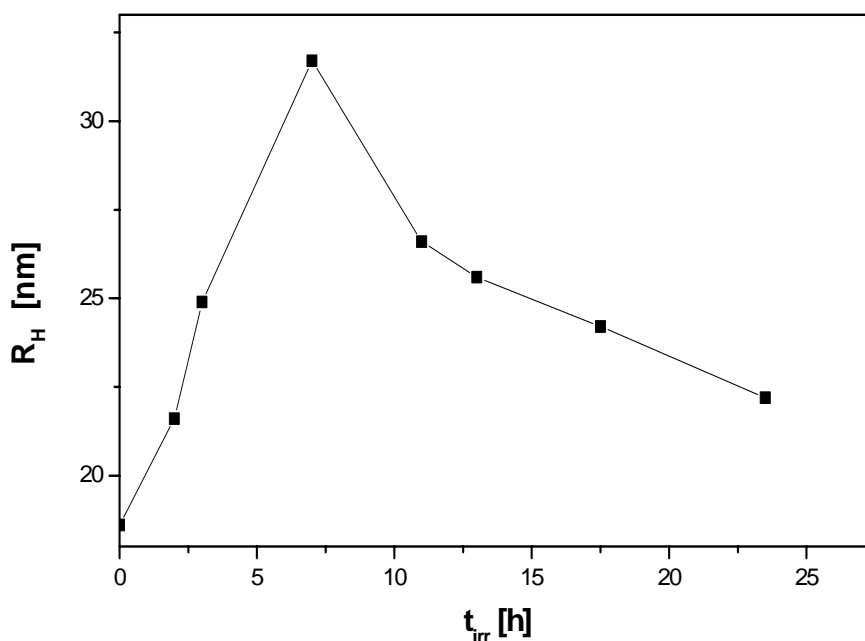

Fig. 4-12   Change of the average R_h of Cin01/THF (2 g/l) particle versus irradiation time (light wavelength 302 nm)

However, both results are not a convincing proof of cluster formation because the increase in size is not remarkable considering the very long irradiation time. Since the cluster formation is induced by inter-particle photodimerization, there are several factors which can influence this process, i.e. particle concentration, environment (solvent polarity, oxygen, …), energy input and the photosensitivity of dye labels. To increase the efficiency of cluster formation, we increased the concentration of dye-labeled nanoparticles in solution up to 10 g/l. Still, we could not observe an obvious increase of the hydrodynamic size, which means concentration is not the reason for this low efficiency of the cluster formation. The photosensitizer benzophenone was also introduced without success. It therefore seems that the low energy input using the lamp-monochromator combination might be the reason for the low efficiency of the cluster formation.

Since the energy output of our lamp at the respective wavelengths of maximum absorption of our dye molecules is quite low (see figures 4-10), the energy output at the monochromator selected single wavelength might not be strong enough to induce the inter-particle photodimerization. So, we removed the monochromator grating and replaced it by using either the whole spectrum of light emitted by the lamp or band pass filters to cut off a certain long wavelength regime of irradiating light from the total lamp emission spectrum. As a result, the energy amount absorbed by the sample per irradiation time is strongly increased.
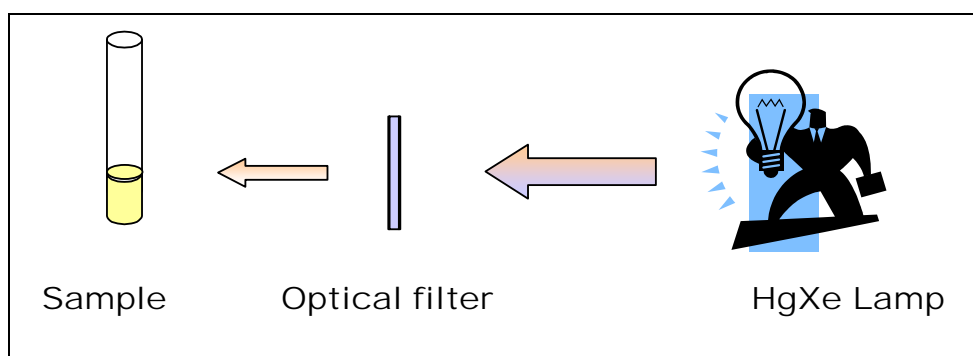

Fig 4-13a **Reversible Cluster Formation of coumarin labeled nanoparticles**
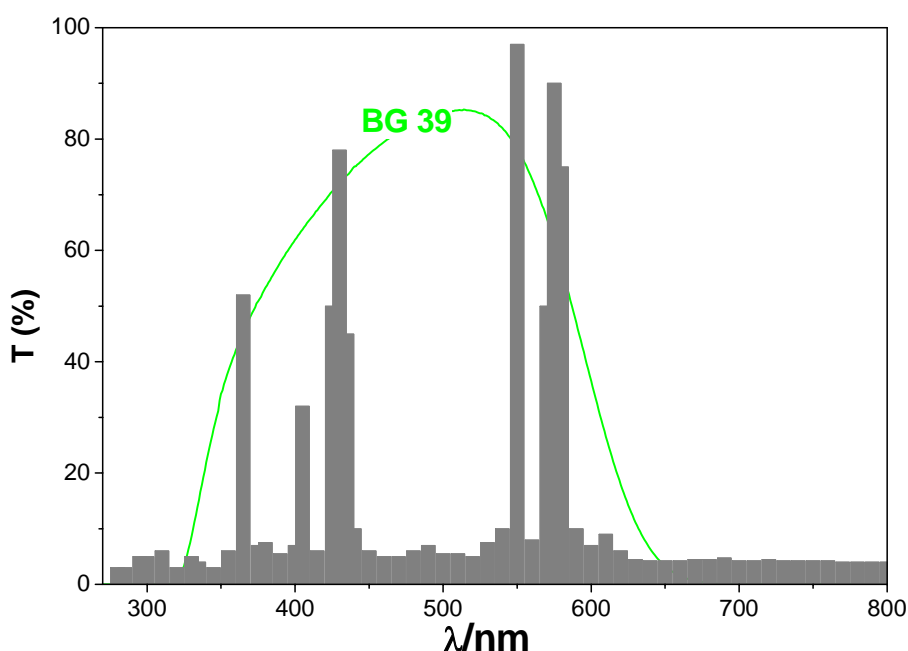

Fig 4-13b **UV transmission spectra of optical filter BG 39.**

Figure 4-13a is the scheme for the modified irradiation setup, figure 4-13b shows the transmission spectrum of the optical glass filter employed. Most of the light useful for photodimerization (>300 nm) was let through and therefore ensures enough energy for the photo-reaction. By irradiation of comparable samples as before, we find that the hydrodynamic radii of the particles increased to 100 nm after only 2 hours irradiation. This remarkable size increase in a relative short irradiation time proves that particles indeed were transformed into clusters induced by inter-particle photodimerization.

However, according to a previous report[37] and our study, this cluster formation based on coumarin 343 labeled nanoparticles has so far been irreversible: it was not possible to destroy the clusters by irradiation with UV light of shorter wavelength. We therefore stopped investigating the coumarin 343 labeled nanoparticles and tried to explore the possibility of reversible cluster formation using two more suitable samples, coumarin and cinnamate labeled nanoparticles.

4.3 Reversible Cluster Formation

4.3.1 Reversible Cluster Formation of cinnamate labeled particles

In this part, we discuss the size change of cinnamate labeled particles (cin04, around 150 labels per particle) upon irradiation. The new setup of irradiation was employed (Figure 4-13), that is optical filter BG 39 was used to cut off UV light of wavelengths shorter than 300 nm. As before we used dynamic light scattering to monitor the size change of particles with irradiation duration. As we expected, the average hydrodynamic radii of the particles increased from 10 nm to 60 nm within 6 hours because of cluster formation.

Figure 4-14 also shows how the particle size changes with irradiation time if the optical filter is removed, that is after large clusters have been formed. By removing the optical filter, the sample was exposed to UV light of very short wavelengths. Instantaneously after removal of the filter, the cluster size decreases dramatically by more than a factor of three. This is caused by the fact that irradiation with light of shorter wavelengths now reverses the photodimerization. Importantly, no change in cluster size is detected if the filter is not removed.
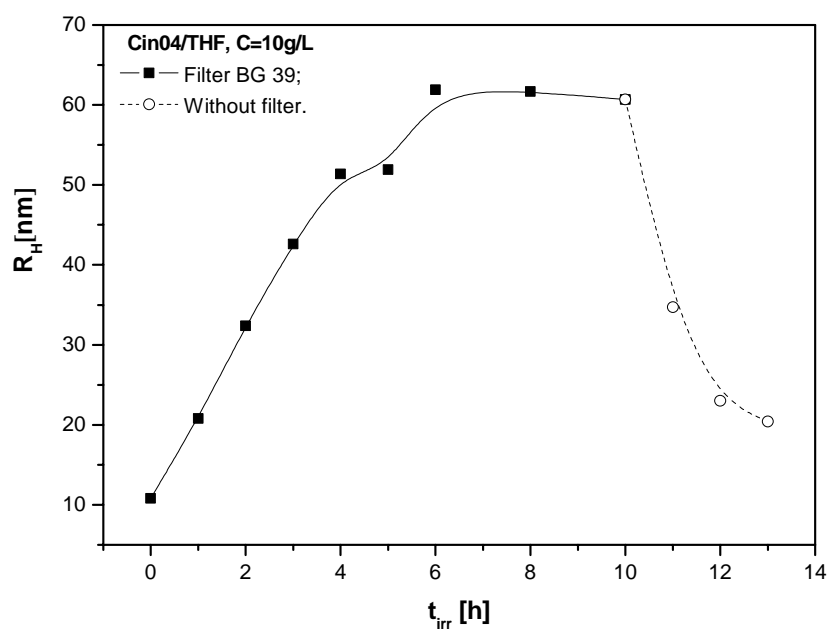
Fig. 4-14 Hydrodynamic Radius of cinnamate-labeled poly(organosiloxane) versus different irradiation time.
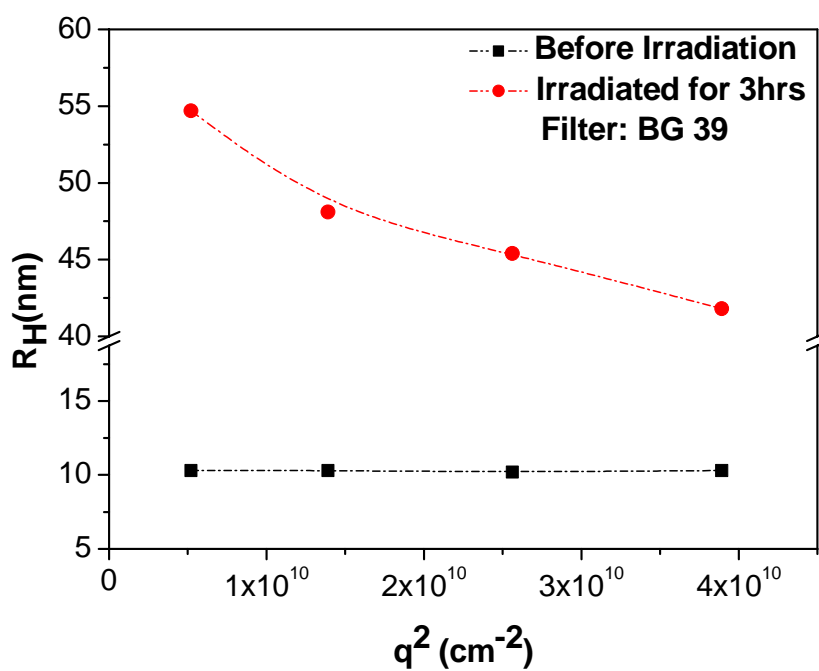

Fig. 4-15 Hydrodynamic radius of dye-labeled polyorganisiloxane-µ-gels before and after photocrosslinking versus scattering vector q^2.

We also observed the dependence of the apparent hydrodynamic radius of the particles on scattering vector, q, as is shown in figure 4-15. The hydrodynamic size changed with different scattering vector after the sample was irradiated for 3 hours, which indicates the clusters formed are rather polydisperse. Clusters of different size and even single nanopaticles could coexist in the solution. Since an accurate analysis of the respective size and amount of non aggregated microgels is very difficult, we restrict ourselves here to the discussion of the average particle size, R_H, which depends both on absolute cluster size and relative amount of clusters and single microgels.

Besides the dynamic light scattering, we also used asymmetric flow field-flow fractionation (AF-FFF) to quantify the reversible cluster formation. AF-FFF can not only measure the size difference of the particles, but also directly give the result of the size distribution[106]. First, the instrument was calibrated with narrow spherical standards to obtain the relation between the hydrodynamic radius R_h of the samples determined by DLS and the retention time t_R of the samples measured by AF-FFF. All measurements were performed at a fixed ratio of crossflow to channel outlet flow.
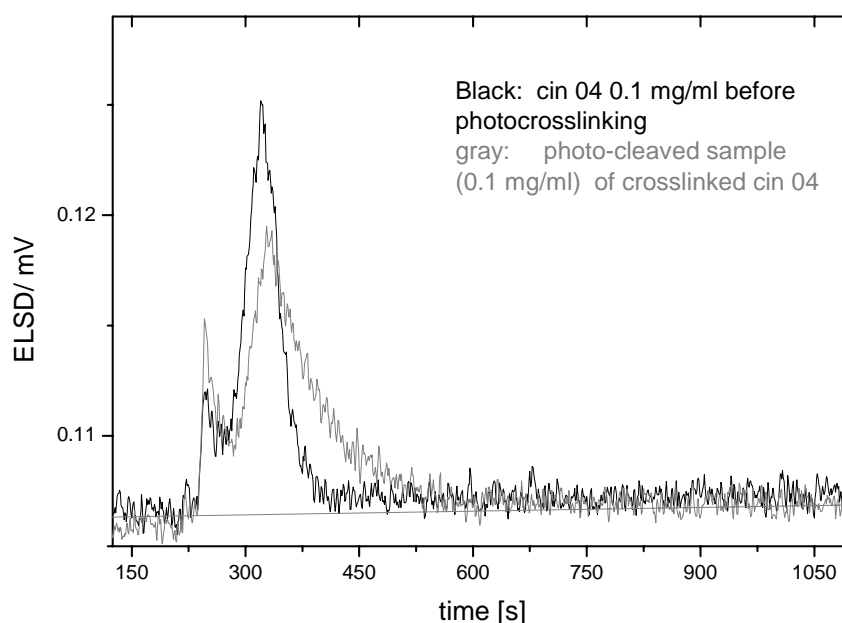

Fig. 4-16 AF-FFF measurement results of cinnamate labeled polyorganosiloxane nanogels (Black: cin04/THF (0.1g/l), Gray: photocleaved sample of crosslinked cin04/THF)

The result is shown in figure 4-16. The positions of the two peaks indicate that the particle size before irradiation and after photo-crosslinking and photo-cleavage is nearly identical, meaning the degree of photo-cleavage is very high. This agrees with the results from dynamic light scattering. By comparing the half peak width of these two peaks, we can also find that the peak for particles undergoing photo-crosslinking and photo-cleavage is broader than that of particles before irradiation. This means some clusters could not be completely reversed into single particles but small clusters and single particles are still coexisting. Since the absorption of the dye-labeled particles on the membrane of the AF-FFF in THF elution phase was very high, the signal detected was very weak, and no signal was detected for big clusters. Therefore, the cluster formation itself could not be investigated by AF-FFF.

The clusters formed by irradiation have been visualized by atomic force microscopy (AFM). A typical example of particles before and after irradiation is shown in figure 4-17. An obvious difference in both size and shape between single particles and clusters was observed in the AFM image.

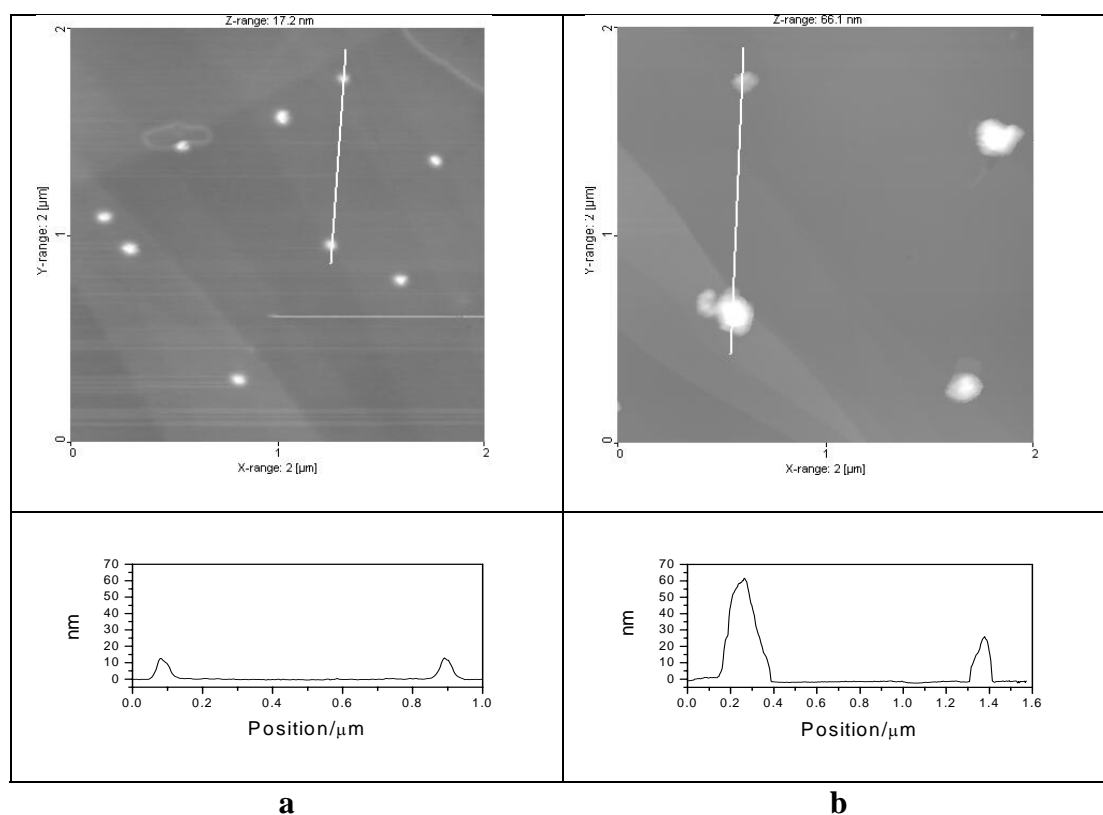**a**   **b**

Fig. 4-17 AFM image and height profile of the cinnamate labeled polyorganosiloxane-μ-gels. a) Before irradiation; b) After irradiation of 10g/l THF solution for 4h by UV light through filter BG 39.

For AFM, the resolution in x-y direction is usually lower than in z direction[107], especially for very small nanoparticles. Therefore we prefer to use the height profile to determine the difference of particles and clusters. From height profile analysis, one finds that even single polyorganosiloxane particles are not as rigid as expected, but are flattened onto the surface of the substrate. The particle height is only 14-15 nm whereas the hydrodynamic diameter of the particles as measured by DLS is larger than 20 nm. After photodimerization, rather uniform isotropic clusters are formed. Here, the height is also only about half as large as expected from the hydrodynamic diameter of the clusters.

Finally, let us demonstrate that reversibility of the cluster formation is also found if the sample is irradiated using our band-pass filter with the lowest cutoff wavelength (WG305) for quite a long time. The corresponding UV transmission spectrum is shown in figure 4-18. Resulting particle cluster size after irradiation is shown in figure 4-19.
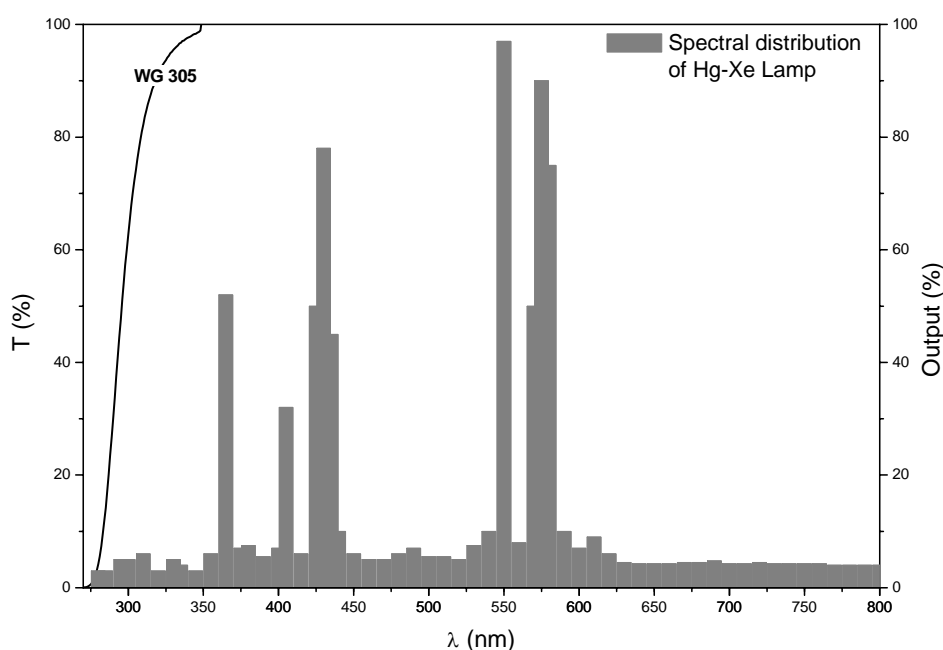

Fig. 4-18 UV transmission spectrum of optical filter WG 305

A steep increase in particle size is followed by a continuous decrease, ending up in a constant equilibrium value which still is more than twice the size of the single colloidal particles. This is quite unexpected, since the filter WG305 should cut off any

light of wavelength much smaller than 300 nm, as shown in its characteristic transmission spectrum (Figure 4-18). Obviously, the transmitted light is still sufficient to reverse the photodimerization to some extent. Comparing the equilibrium value obtained here with the equilibrium size obtained after removal of the optical filter, the former seems to be much smaller (< 20 nm). This underlines our statement that for long-time irradiation with filter WG305 the photodimerization is only partially reversed, whereas upon removal of the optical filter and irradiation with the total wavelength spectrum of our UV-lamp nearly the original size of the single particles is reached. Therefore the reversion of photodimerization in this case seems to be fairly complete.

Finally, the similar curves in figure 4-19 obtained for two cinnamate labeled particle solutions irradiated at the same condition nicely demonstrate the reproducibility of the cluster growth and shrinkage.
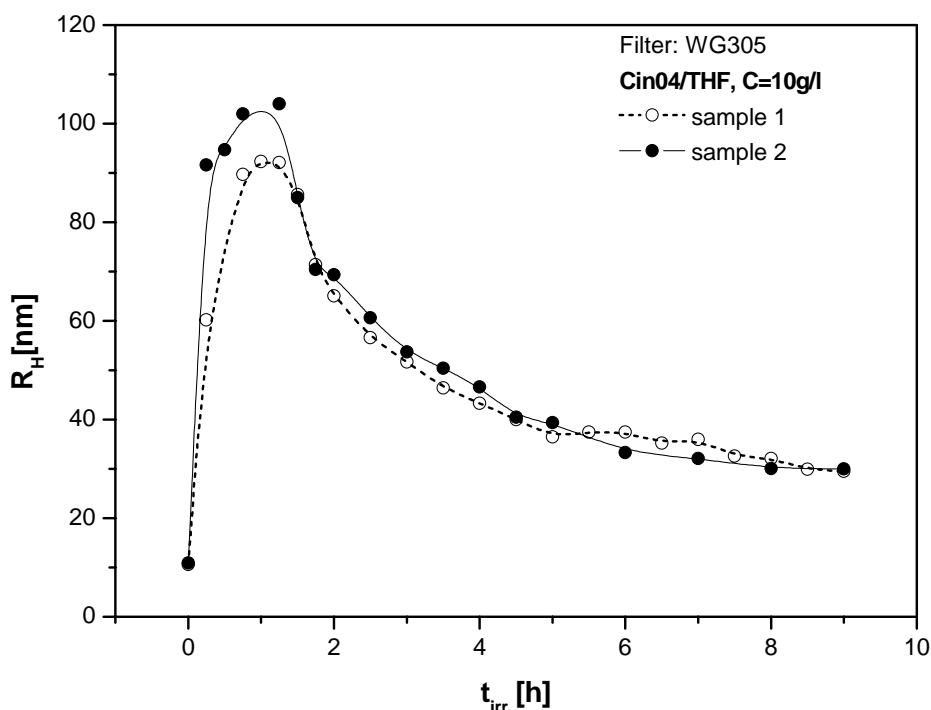

Fig. 4-19 Hydrodynamic Radius of cinnamate labeled polyorganosiloxane-µ-gels versus irradiation time, sample 1 and sample 2 were irradiated under the same conditions.

4.3.2 Reversible Cluster Formation of coumarine labeled particles

We observed the cluster formation of coumarin-labeled polyorganosiloxane-μ-gels (cou0303, around 136 labels per particle) under the same irradiation condition (concentration, solvent and optical filters) as for cinnamate-labeled particles. Similar reversible cluster formation behavior was observed. (Figure 4-20)
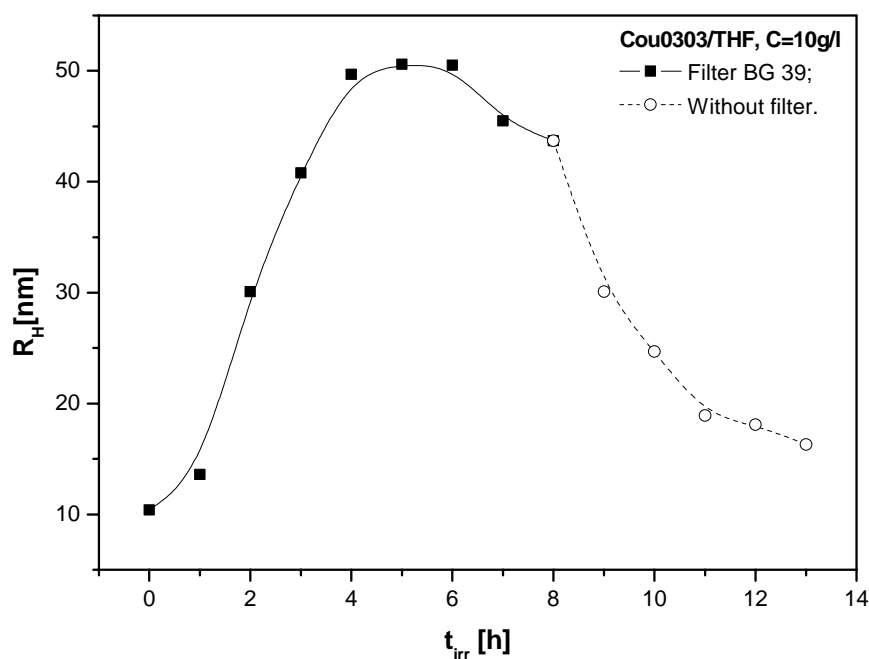

Fig. 4-20 Hydrodynamic Radius of Coumarin-labeled polyorganosiloxane-μ-gels versus irradiation time.

In conclusion, both our cinnamate- and coumarin-labeled colloidal systems undergo a reversible photodimerization and therefore a reversible cluster formation, as could be expected from previous results obtained from the pure dye molecules. Here, this reversibility can be used to make supramolecular particle aggregates grow and shrink in a controlled way.

However, the reversible cluster formation of coumarin labeled nanoparticles is not as controllable as for the cinnamate labeled particles. When irradiated at identical conditions, the speed of the size increase for the former changed sometimes. Hence, in the next few parts we focus on the study of the reversible cluster formation of cinnamate labeled nanoparticles only.

73

4.4 Effect of optical filters on Cluster Formation

We discussed in chapter 4.2 that by replacing the monochromator with a band pass filter, the rate of cluster formation greatly increased. This means the dimerization rate or particle growth rate was strongly depending on the filter used and therefore on the corresponding total power and spectrum of irradiating light.

To explore the influence of optical filters on the dimerization rate in more detail, we irradiated identical samples through different optical filters. The UV transmission spectra of the filters is given in Figure 4-21.
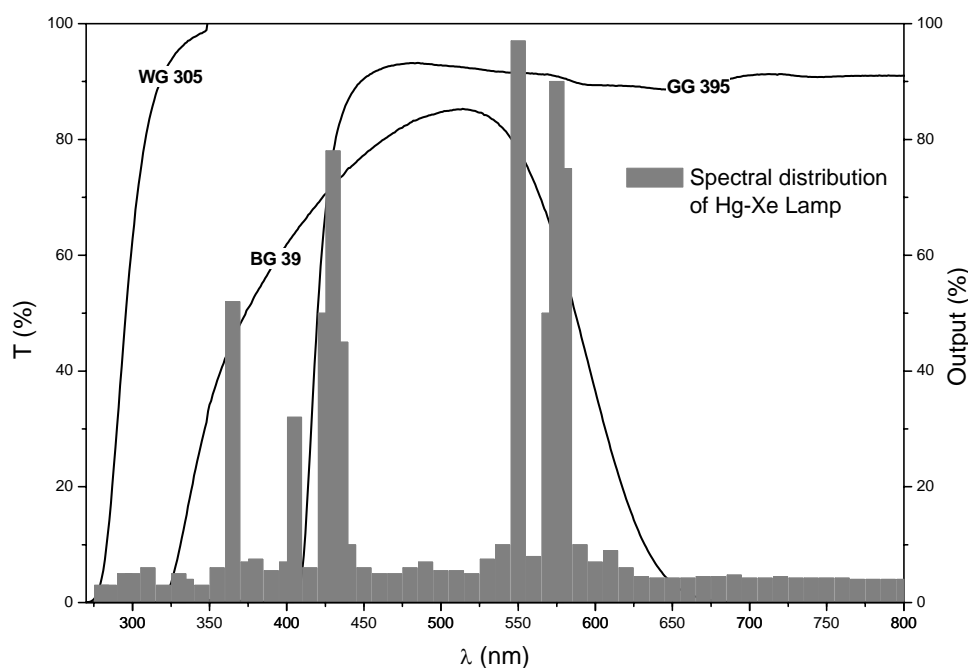
Fig. 4-21 Spectra of all optical filter (WG 305, BG 39, GG 395) used during irradiation.

In figure 4-22, we have plotted the increase in hydrodynamic radius for cinnamate labeled nanoparticles (cin04, around 150 labels per particle) in THF solution (c= 10 g/l) for different irradiation conditions, that is using three different band-pass filters. Here, the reader should keep in mind the different characteristics of the band-pass filters (optical transmission) shown in figure 4-21.

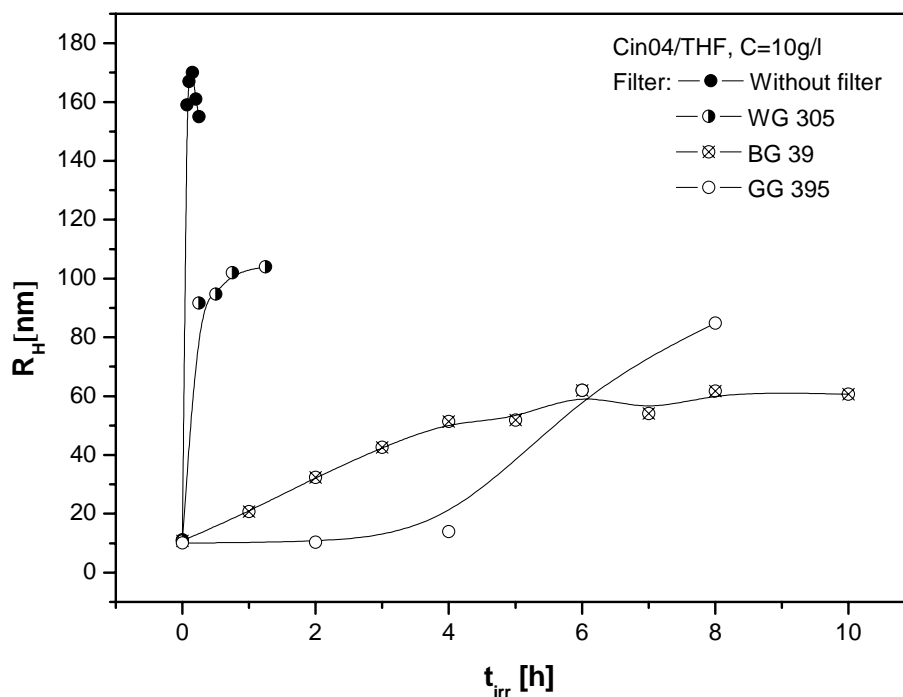**Fig. 4-22** Change of the hydrodynamic radii of cinnamate labeled polyorganosiloxane-μ-gels in THF versus irradiation time, different optical filters were used in this easurement.

It is nicely demonstrated how the kinetics of the photodimerization can be adjusted in a simple way via the irradiation conditions: the larger the energy input or, correspondingly, the lower the cut-off wavelength of the optical filter, the faster the particle growth. This conclusion was further proved by using UV lamps with different power output. Here we used another higher energy pulsed UV lamp (RC250B from Xenon-Corp, the spectrum of the emitted light is shown in figure 4-23a) to irradiate the sample and investigate the hydrodynamic size change by dynamic light scattering, and compared the results with our Hg-Xe lamp irradiation. This pulse lamp has higher energy output (390 Watt), and continuously emits UV light at wavelengths 200-300 nm (5%) and 300-400 nm (11%). It is obvious from figure 4-23b, c that by using higher energy input (pulsed lamp), the speed of cluster formation is faster both in Toluene solution (b) and in THF solution (c).
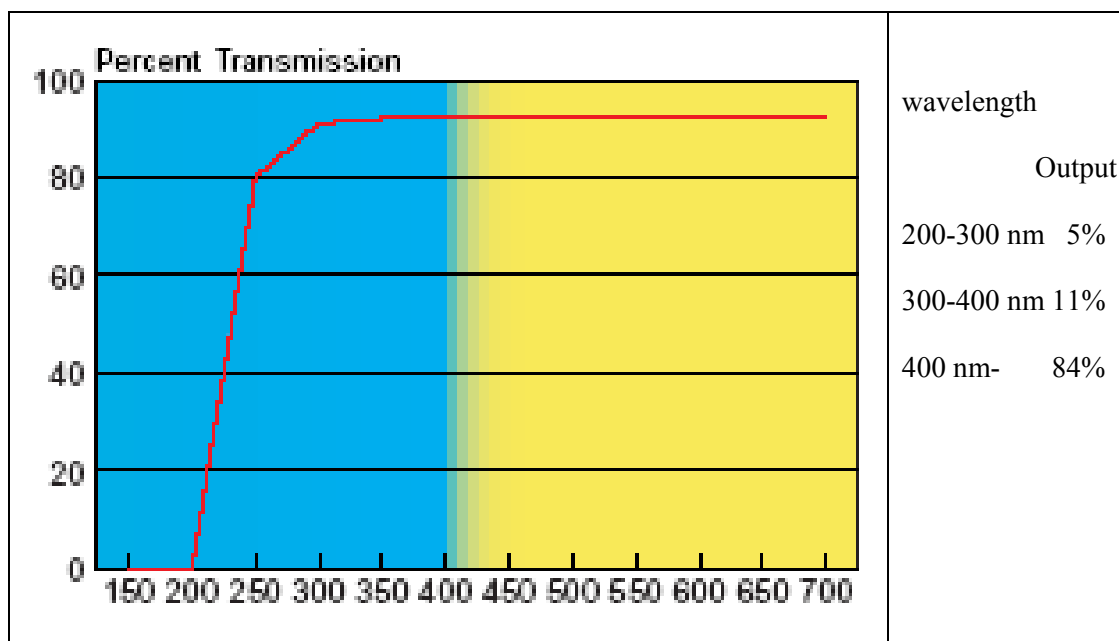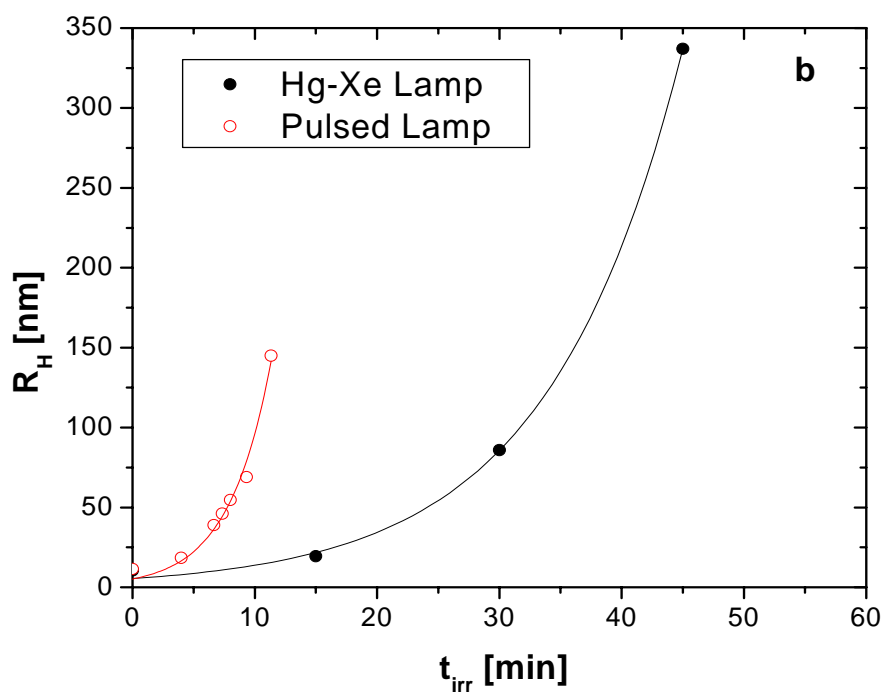
Fig. 4-23a Spectral distribution of the light emitted by the pulsed UV lamp (RC250B from Xenon-Corp.).
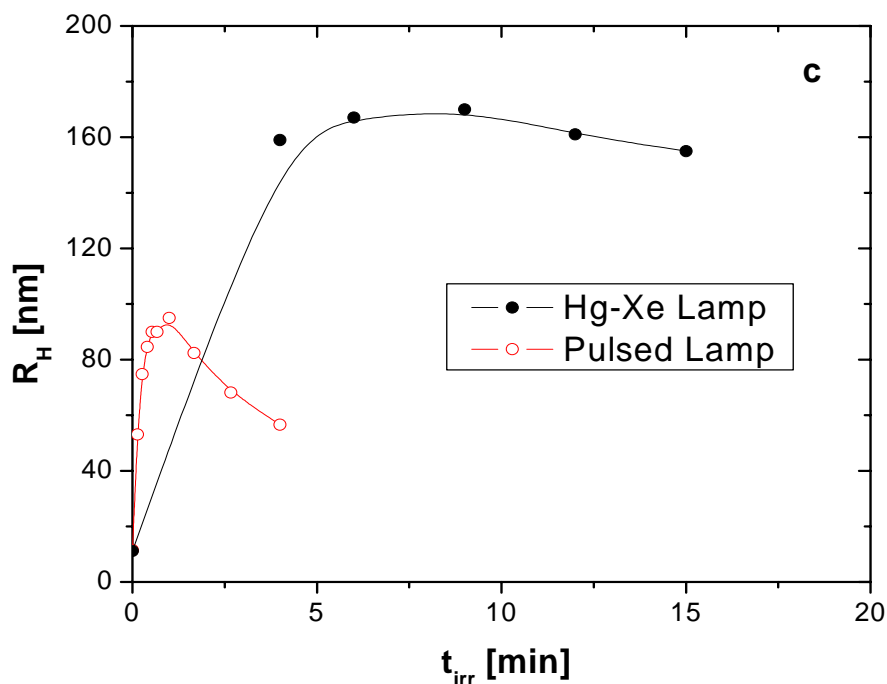
Fig. 4-23b,c Change of the hydrodynamic radii of cinnamate labeled polyorganosiloxane-μ-gels in THF versus irradiation time, irradiated by using a pulsed lamp or a Hg-Xe lamp (no optical filter was applied). b): cin04/toluene (10 g/l), c): cin04/ THF (10 g/l).

4.5 Effect of dye content on Cluster Formation

The dye content of the nanoparticles also plays an important role on the cluster formation. We prepared a series of cinnamate labeled polyorganosiloxane nanoparticles with different cinnamate contents (see table 3-4) and investigated their size change against irradiation time. From the plot of the hydrodynamic radii of polyorganosiloxane-μ-gels with different cinnamate content versus irradiation time (figure 4-24), we find as expected that the nanoparticles with higher cinnamate content form clusters at higher speed. This is reasonable, because if the dye content is higher, the possibility of dye molecules to "meet" with each other in a position favorable for the photochemical reaction is also higher.

On the other hand, for nanoparticles of much higher dye content, intraparticle photodimerization may compete with interparticle photodimerization. However, we discussed before (See page 63) that if the dye content is lower than 400 labels per

particle, intraparticle photocrosslinking will not be favored because of the long distance (> 1 nm) between different dye molecules. With increase of the dye content (> 400 labels/particle), however, also the possibility of intra-particle crosslinking increases, which consumes the photo-labels without forming clusters. As a result, although the dye content continuously increases, the speed of cluster formation will only increase up to a certain degree and then reaches a limitation.
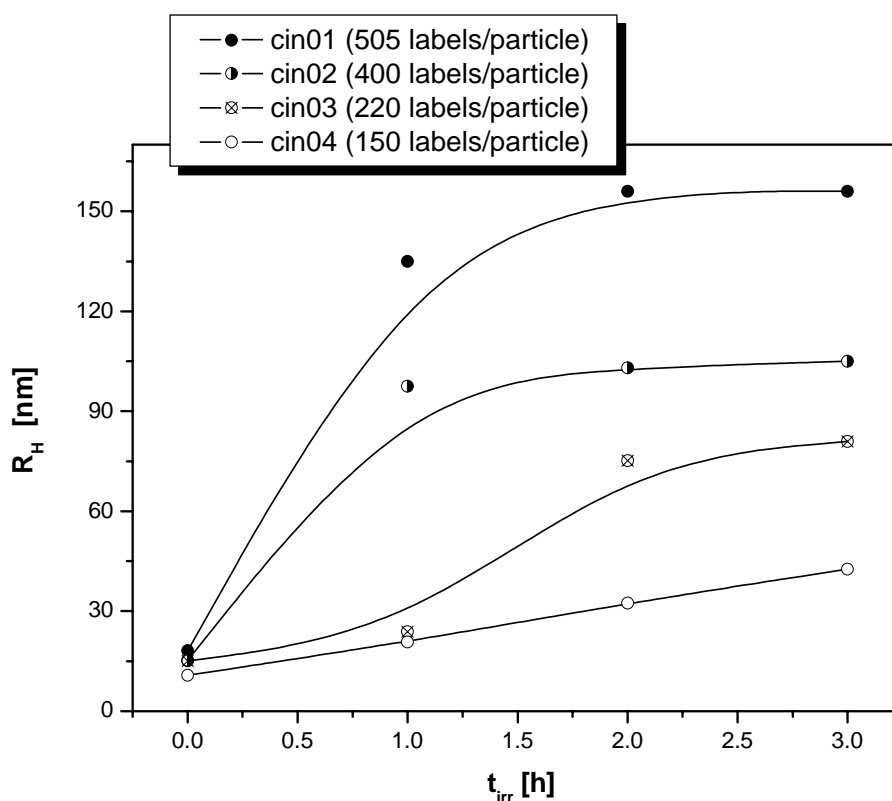
Fig. 4-24 Change of the average hydrodynamic radii of polyorganosiloxane-μ-gels with different cinnamate content in THF versus irradiation time.

4.6 Solvent Effect on the Cluster Formation

We also checked the cluster formation of cinnamate labeled nanoparticles (cin04, around 150 labels per particle) in different solvents. Toluene and THF were used to investigate the solvent effect on the cluster formation because both of them are a good solvent for cinnamate labeled particles and, importantly, they have different UV absorption spectra.
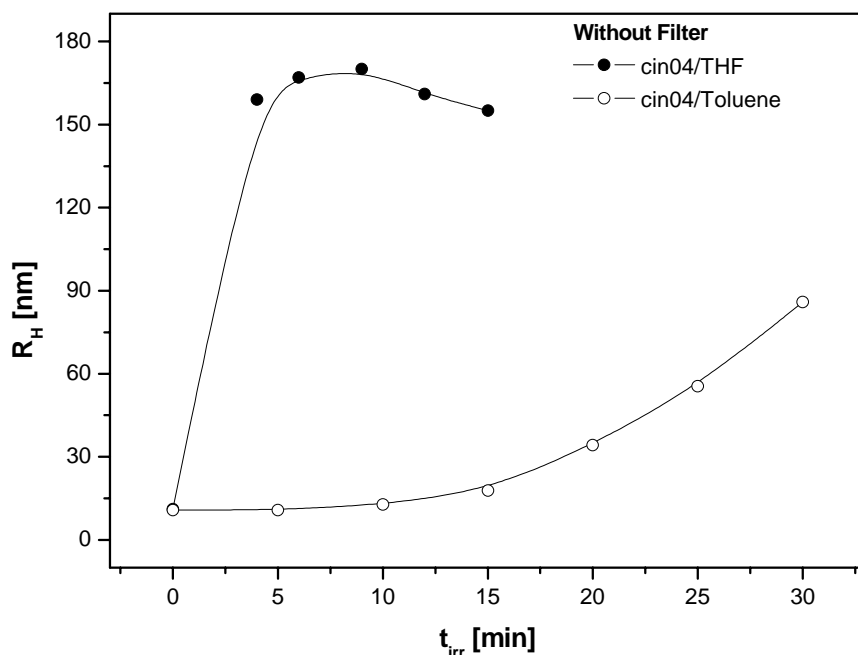
Fig. 4-25 Change of the hydrodynamic radii of cinnamate labeled polyorganosiloxane-µ-gels in Toluene and THF versus irradiation time

In figure 4-25, we have plotted the increase in hydrodynamic radius vs. irradiation time for two solutions of cinnamate-labeled particles (c = 10 g/l) in the different solvents toluene and THF. Both samples have been irradiated using no optical filter.

Obviously, the increase is much slower in case of the toluene solution. In THF, the clusters grow very fast and hit the limitation after 10 minutes, the average hydrodynamic size then beginning to decrease due to photocleavage of the clusters without the protection of an optical filter. In toluene, the speed of cluster growth is slower but continuously, we couldn't observe a decrease of the average hydrodynamic size of this sample, and the solution ended as a turbid solution after being irradiated for 2 hours. This result shows that photocleavage was totally suppressed in the toluene solution. This is trivially explained by the fact that toluene itself due to its UV absorption serves as an optical filter. The UV absorption spectra of pure toluene and THF are shown in figure 4-26. For clarification, the optical transmission of the pure solvents is summarized in table 4-1.

From the UV absorption spectrum, the optical transmission of pure toluene is much lower than that of THF at wavelengths < 300 nm. Therefore, the use of toluene or THF makes a major difference in respect to the energy input by radiation, i.e. an eventual optical filter effect of the solvent itself may strongly influence the kinetics of our photocrosslinking reaction.
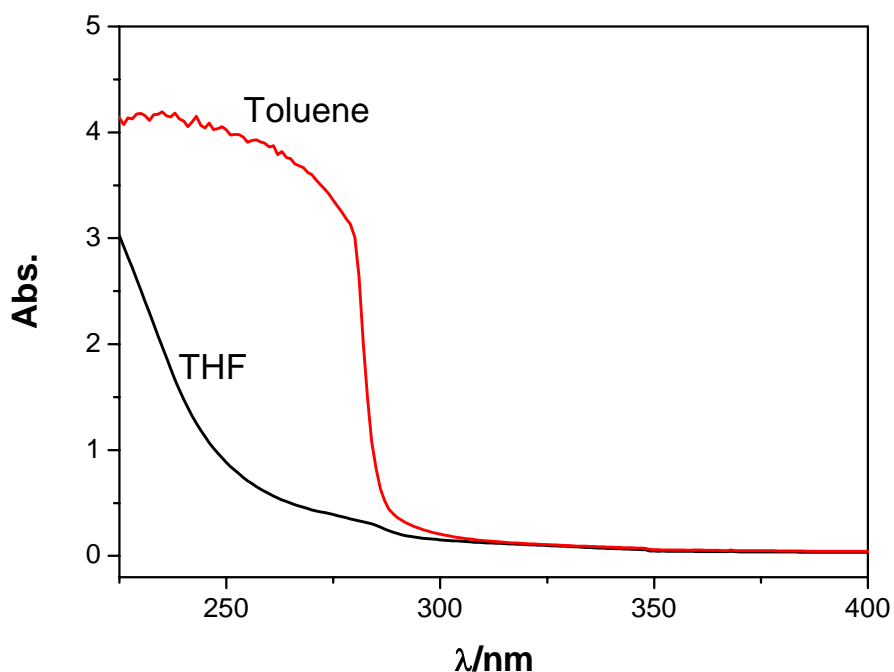

Fig. 4-26 UV spectrum of pure toluene and THF (Optical path length: 10mm).

Table 4-1 Optical Transmission of THF (a) and Toluene (b)

(a)

λ/nm	T(%)
240	30
250	52
260	70
280	89
300	96
>320	98

(b)

λ/nm	T(%)
285	10
290	50
300	80
310	89
320	93
>350	98

4.7 Optimization of Irradiation Conditions

As shown so far, we observed that the dye-labeled particles form clusters and these clusters can be cleaved into single particles again. However, the cleaved particles couldn't form clusters again after UV irradiation during the previous experiments. An ideal reversible photodimerization should allow unlimited monomer-dimer-monomer transitions. No cluster formation of the particles after photocleavage means that the photo labels on the particles are destroyed irreversibly and not photoreactive anymore. Usually, UV light may cause such undesirable side effects on organic molecules. Therefore, the suitable range of UV light is very critical for reversible photodimerization. How should one choose the range of UV light to make sure it is effective enough for photoreaction but meanwhile not harmful for the dye itself? First, we have to monitor the chemical structure changes of the photo labels during the photoreactions. We used UV spectroscopy to record the spectrum of cinnamate-labeled nanoparticles upon irradiation for both photocrosslinking and photocleavage.

4.7.1 Investigation of irradiated dye-labeled nanoparticles by UV-vis Spectroscopy

The UV-vis spectra of cinnamate-labeled particles in THF irradiated with UV light > 300 nm (Filter BG 39) are shown in figure 4-27. With the increase of irradiation time, the intensity of the UV absorption decreases and shifts to blue due to the formation of the photocrosslinking product.

Then we tried to photocleave the cinnamate photodimer by exposing the previous sample to UV light < 300 nm (no filter). If the photodimer undergoes symmetric cleavage, it should switch back to the original cinnamate molecules, causing higher absorption intensity and red shift in the UV-vis spectrum (a reverse of figure 4-27). From the actual result shown in figure 4-28, however, the UV absorption continuously decreases after photocleavage. This result shows that not the desired photocleavage happens and the photo labels are destroyed irreversibly.
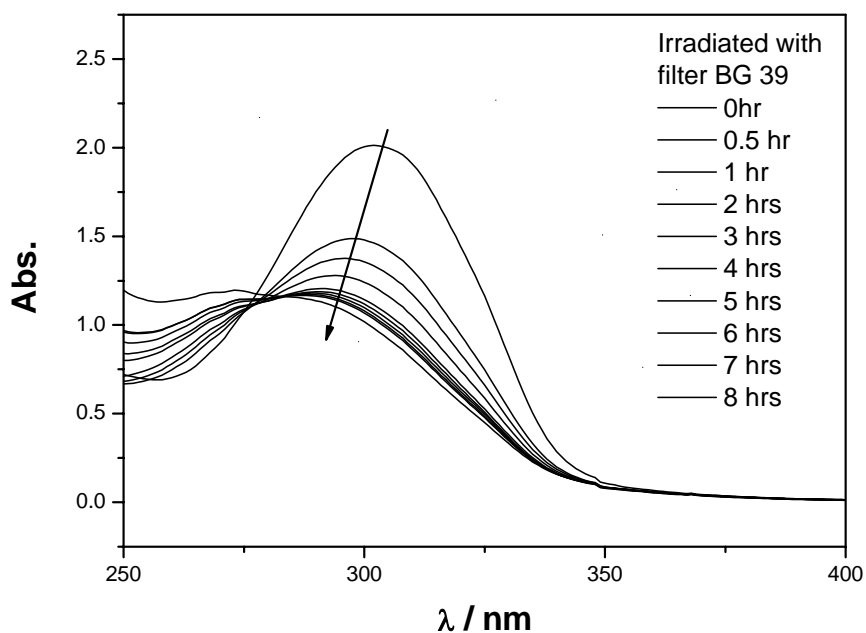
Fig. 4-27 UV-vis spectrum of cinnamate-labeled-polyorganosiloxane-μ-gels (cin04)/THF solution before and after irradiation with UV light >300 nm.
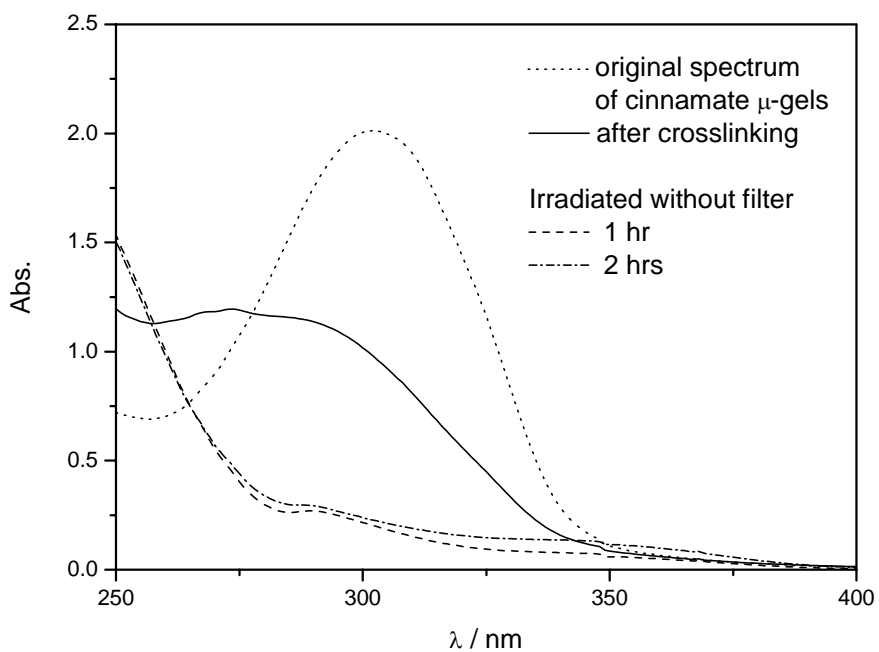

Fig 4-28 UV-vis spectrum of cinnamate-labeled-polyorganosiloxane (cin04)/THF solution after photocrosslinking, then photocleaved by UV light < 300 nm.

4.7.2 Toluene bath as a novel optical filter

In part 4.6, we studied the solvent effect on cluster formation of dye-labeled nanoparticles and found out that the photocleavage of cinnamate labeled particles could be suppressed in toluene solution. This interesting phenomenon told us that toluene could act as a perfect optical filter to allow only photodimerization during the process of photo-crosslinking. Though toluene is a perfect solvent for photo-crosslinking, the reversible cluster formation can't be executed in toluene because it will prevent the clusters from photocleaving according to the result in part 4.6. To solve this problem, we immersed the dye-labeled particle (cin04, around 150 labels per particle)/THF solution in a toluene bath (figure 4-29) for the photo-crosslinking experiment. Here the toluene bath is supposed to act as an optical filter and totally suppress the undesired photocleavage. After photocrosslinking, the sample solution in THF can be taken out form the toluene and used for the photocleavage study.
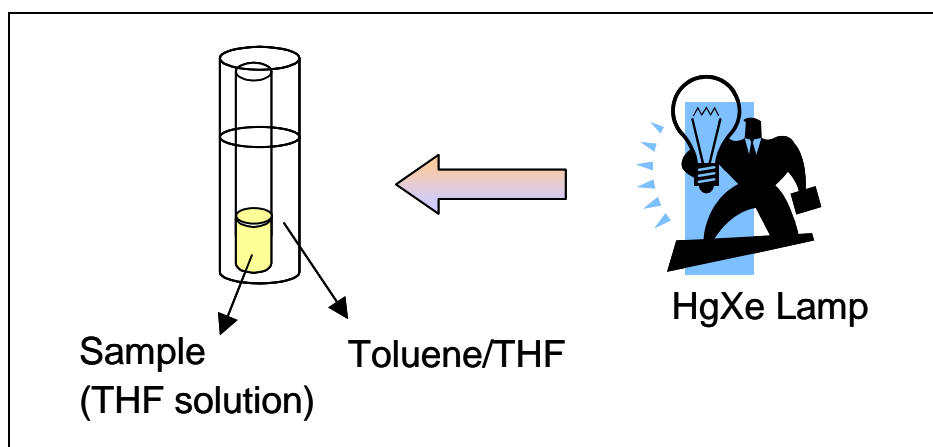
Fig. 4-29 Scheme for irradiation through solvent filter.

The average hydrodynamic radii of the sample solution vs. irradiation time were monitored using dynamic light scattering as before. The results given in figure 4-30 (circles) show that the toluene bath has the same protection effect as a particle/toluene solution, the photocleavage seems to be totally suppressed because we didn't observe the decrease of the average hydrodynamic radius and the solution finally turned turbid. It is worth to mention that when we used a mixture of toluene and THF as the solvent bath, the initial formation of clusters was faster than in a pure

toluene bath, but then the cluster formation soon reached its limitation (figure 4-30, spheres). The two different curves in figure 4-30 indicate that by varying the solvent ratio in the solvent bath, the kinetics of cluster formation can be changed.
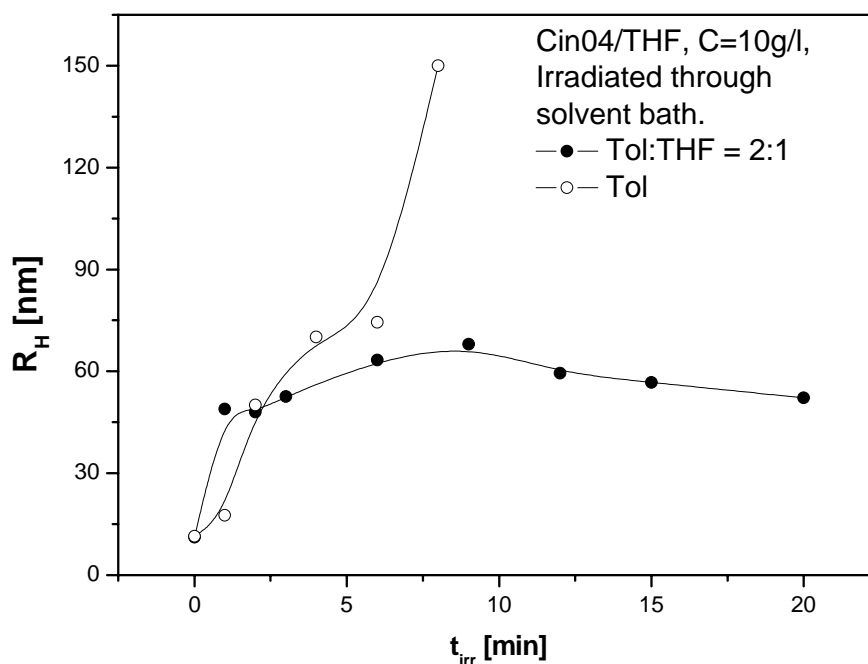
Fig. 4-30 Change of the average hydrodynamic radii of cinnamate labeled poly(organosiloxane) nanoparticles (c = 10 g/l) versus irradiation time. Sample cuvettes were immersed into two different solvent baths. (toluene and toluene/THF (2:1))

4.7.3 Combination of toluene bath and dichroic mirror

Since our target is reversible cluster formation, we also need to safely cleave the clusters without irreversibly destroying the cinnamate molecules. Previously we used UV light < 300 nm for photocleavage, and since the Hg-Xe lamp emits UV light of wavelengths as short as 230 nm, this could be the reason why the photo labels were destroyed. To avoid the harmful UV light of very short wavelength (< 250 nm), we employed a dichroic mirror which provides a very narrow band of UV light around 254 nm for photocleavage. (Figure 4-31b)
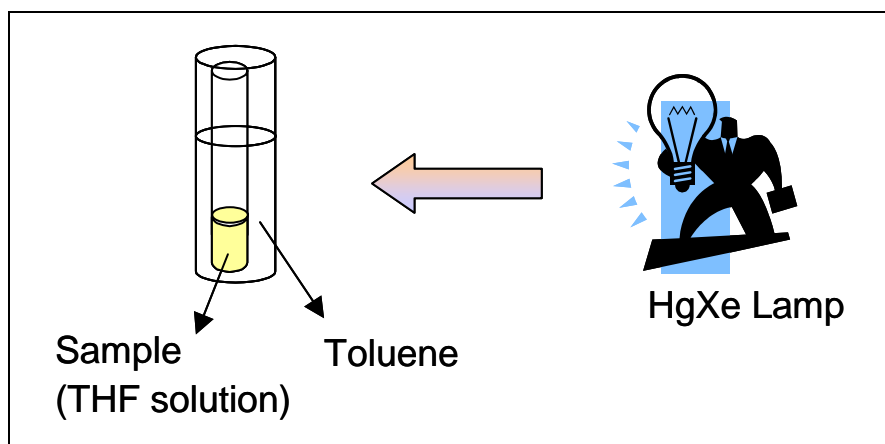
a): Photocrosslinking
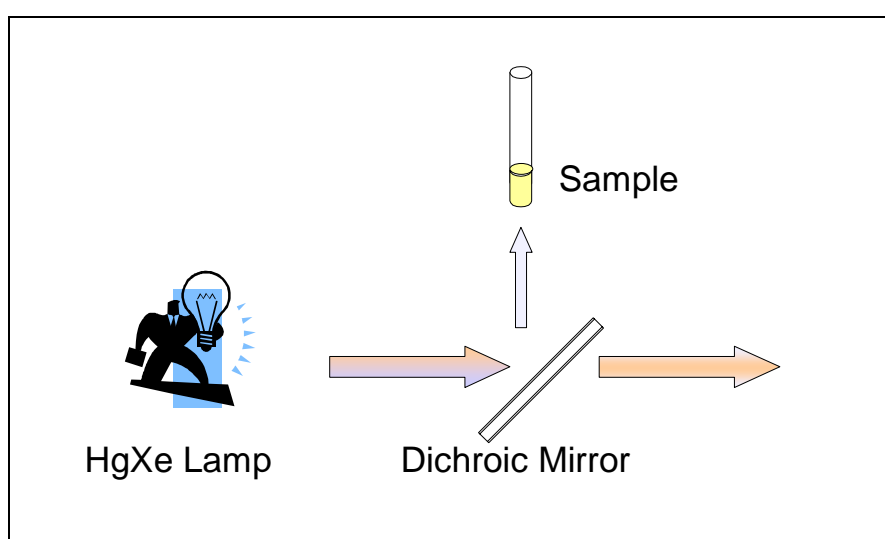
b): Photocleavage

Fig. 4-31 Scheme for irradiation through solvent filter and dichroic mirror.

To prove the advantage of the experimental conditions shown in figure 4-31, the photo-reaction of p-nitrocinnamate moieties was studied using UV-Vis spectroscopy. For UV-Vis spectroscopy measurements, we used only 2 g/l cinnamate-labeled poly(organosiloxane) nanoparticles (Cin04)/THF, because a higher sample concentration will exceed the measurement limit of the UV-Vis spectrometer. The UV absorption spectra for photocrosslinking and photocleavage were shown in figure 4-32 and figure 4-33, respectively.

Figure 4-32 shows the UV absorption spectrum of cinnamate-labeled poly(organosiloxane) nanoparticles during photocrosslinking. From the spectrum of

cinnamate-labeled poly(organosiloxane) nanoparticles before irradiation, we find that 2 g/l is already a concentration slightly too high for UV spectroscopy, and the absorption peak at 302 nm decreases abruptly in intensity after only 5 mins' irradiation. This intensity decrease is much faster than in case of irradiation using filter BG39 (figure 4-27), proving the higher efficiency of the photoreaction which is also shown in the speed of cluster formation (Figure 4-34).
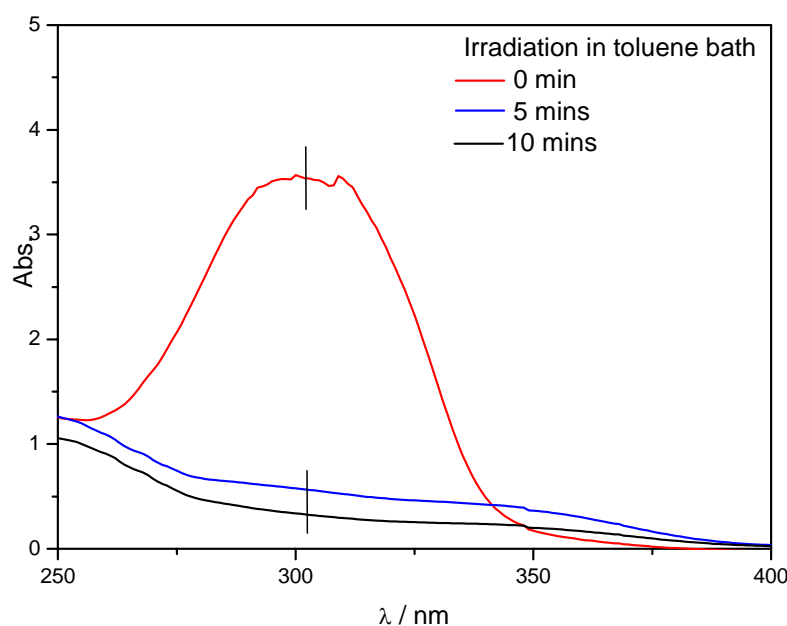
Fig. 4-32 UV-vis spectrum of cinnamate-labeled-polyorganosiloxane (cin04)/THF solution before and after irradiation in a toluene bath.

The photocrosslinked sample was then photocleaved by irradiation using a dichroic mirror (figure 4-31b). The spectra in figure 4-33 show that after the sample was irradiated at 254 nm for 5 mins, the UV absorption intensity between 275 nm and 310 nm increases slightly. Since the absorption maximum of cinnamate is at 302 nm, we assume that this indicates a very small part of photocrosslinking products are cleaved into cinnamate. We couldn't observe further increase of the absorption intensity in this wavelength regime after longer irradiation, meanwhile the absorption in the range of 250 - 275 nm and 310 - 400 nm decreases continuously with irradiation time, which we believe corresponds to the disappearing of the photocrosslinking product during the photocleavage.
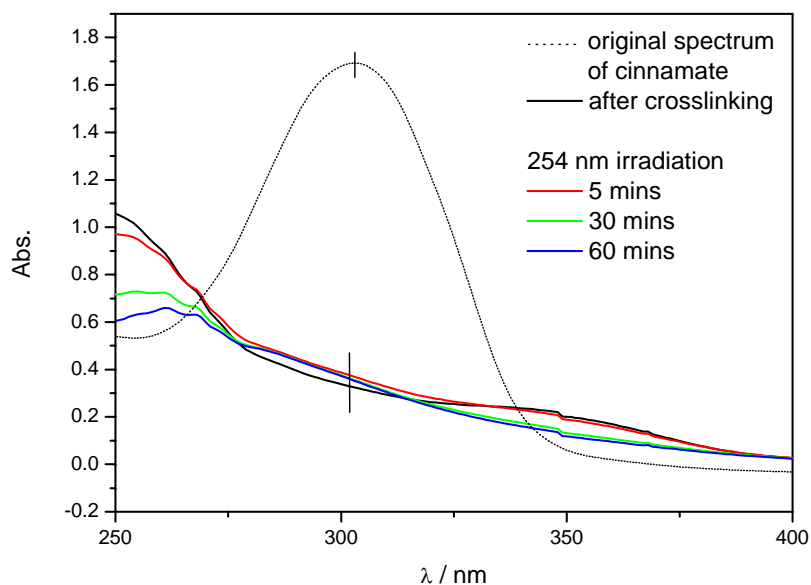
Fig 4-33 UV-vis spectrum of cinnamate-labeled-polyorganosiloxane (cin04)/THF solution after photocrosslinking, then photocleaved by UV light at 254±10 nm using a dichroic mirror.

The photodimerization of p-nitrocinnamate moieties under the new experimental conditions shows only partial reversibility in the UV spectra. Since our purpose is to explore the possibility of highly reversible cluster formation, we still need to investigate the cluster formation of our photoreactive nanoparticles under these new experimental conditions. The average hydrodynamic size of the particles in solution was monitored again by dynamic light scattering. By using the combination of a toluene bath for photo-crosslinking and a dichroic mirror for photo-cleavage, we observed a second increase of particle size. (figure 4-34). This means the process of cluster formation/destruction indeed is partially reversible. However, the photolabels are still inevitably destroyed even under this modified irradiation condition, so we couldn't observe a third increase of average hydrodynamic particle size.

If we compare this optimized reversible particle-cluster transition with our previous experiment results (figure 4-14), we find that both cluster growth and decrease are much faster in this optimized experimental condition. This means that the optimized experiment can not only protect the dye itself, but also increases the efficacy of the interparticle photodimerization.
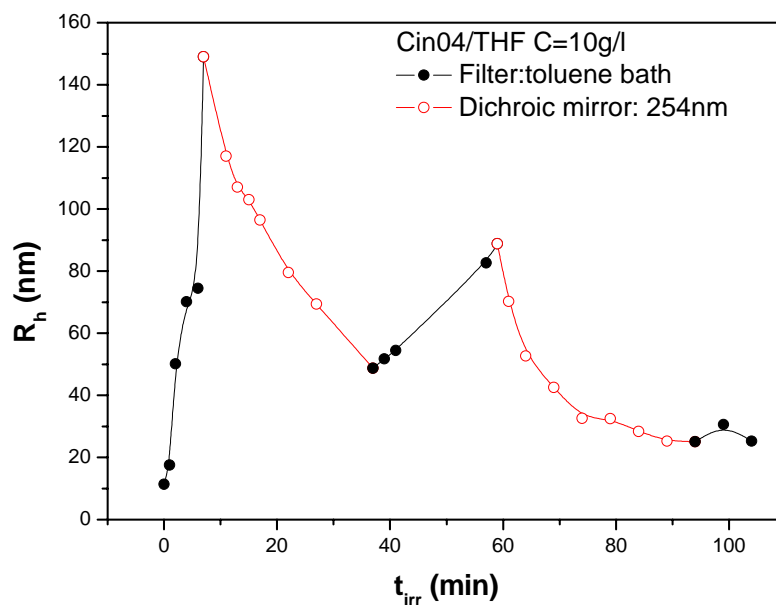
Fig. 4-34 Change of the average hydrodynamic radii of cinnamate-labeled poly(organosiloxane) nanoparticles (c = 10 g/l) versus irradiation time and wavelength

Though the results shown in this part are still not satisfying, it is an encouraging discovery, which means the experimental conditions were improved and under even more optimized irradiation conditions, an even higher degree of reversible cluster formation should become possible.

5 PHOTOCLEAVABLE POLYORGANOSILOXANE MICROCAPSULES BUILT FROM PHOTOREACTIVE NANOPARTICLES

Encapsulation of chemical substances in tiny containers and their controlled release remain a highly challenging but extremely important subject in the modern field of nanoscience [108-111]. This field may not only open up new pathways to control chemical reactions on a nano-scale level, but also promises important new findings relevant to health care as, for instance, drug targeting and controlled drug release. Many different types of such tiny containers have recently been prepared. In the following we try to provide a brief historic overview which is far from complete, but should provide a representative insight in the variety of synthetic techniques used for the preparation of microcapsules. All these techniques have in common that they use some form of well-defined microscopic template, around which the shell of a microcapsule can be formed. Such templates may vary from monodisperse polymeric microparticles to tiny oil or water droplets. The later can be prepared by various methods, ranging from simple spraying to highly sophisticated emulsion techniques. This variety shall be illustrated by the following examples: Hettler et al. prepared crosslinked protein microcapsules which were capable of iron binding, using an interfacial crosslinking process with terephtaloylchloride [112]. Cylindrical polymeric microcapsules used for enzyme immobilization were synthesized by a template-based synthetic method [113]. The template technique has also been used to prepare polypyrrole microcapsules employed for immobilization of both enzymatic and catalytic systems [114]. Another approach is the coacervation method, used for example to make chemically crosslinked poly (vinyl alcohol) microcapsules containing oil [115]. Interfacial crosslinkage of different amounts of chitosan solubilized in the inner phase of a water/oil emulsion was used to prepare a controlled release system for insulin [116]. Duarte et al. used the same approach to synthesize microcapsules from starch derivatives [117]. A completely different technique is the preparation of microcapsules by photopolymerisation in aerosols: well defined capsules with solid polymer shell and liquid core, in the size range $10 - 50$ μm with different shell thickness to core diameter ratios have been fabricated by Esen et al. [118]. Polyurethane microcapsules

with good mechanical resistance but sufficiently subtle to allow deformation without breakage have been synthesized by interfacial polycondensation [119]. Interfacial polycondensation has also been used to prepare polyamide capsules with various sizes[120]. These capsules, however, were mechanically instable: they could all be destroyed after only 5 minutes of ultrasonic irradiation. Combination of the characteristics of the interfacial reaction and conventional emulsion processes was used to prepare a new system of very small microcapsules with a hydrophilic polymeric wall [121]. A very sophisticated but quite simple new emulsion technique, miniemulsion, has recently been used to prepare small uniform microcapsules consisting of hollow shells of clay sheets [122]. A very interesting system, monodisperse thermoresponsive core-shell microcapsules with a mean diameter of about 4 μm with a porous membrane and with linear-grafted poly(N-isopropylacrylamide) (PNIPAM) chains in the membrane pores acting as thermoresponsive gates has been reported by Chu et al. [123]. The excellent monodispersity of these capsules has been achieved using a combination of the new Shirasu porous glass (SPG) emulsification technique and interfacial polymerization. Another interesting and extremely simple approach is the so-called droplet technique: an aqueous solution has been sprayed into an organic solvent containing cyanoacrylate esters which then have been polymerized at the droplet interface to form semipermeable membrane microcapsules [124]. Alternating polyelectrolyte multilayers have also been used to prepare microscopic spherical shells. Two interesting examples for this approach are: (i) microcapsules with a multilayer shell of poly(styrenesulfonate) and poly(allylamine hydrochloride) permeable for small ions used to prepare well-defined inorganic particles [125], and (ii) thermosensitive hollow capsules based on thermosensitive polyelectrolytes which showed a decrease in permeability with increasing temperature [126]. Unfortunately, this thermoresponsive behaviour was only partially reversible. Here, we should not forget to mention that Caruso and coworkers recently developed a very nice microcapsular system which, due to light-absorbing gold nanoparticles incorporated within the polyelectrolyte layers constituting the microcapsule shell, is optically addressable for controlled drug delivery[34]. Such a system is interesting for potential applications. For microcapsule preparation of filled containers we find the approach using water/oil/water-emulsions as a template more attractive than the layer-by-layer assembly onto solid colloidal particles, since in this case any drug or substrate soluble in water can be encapsulated

directly and up to very high amounts in a trivial way. Therefore, we became interested in developing a new species of optically controllable microcapsules by combining a templating technique using water/oil/water emulsions with our spherical nanoparticles which undergo reversible photoaggregation [127] as has been shown in the previous chapter of this thesis.

5.1 Water/Oil/Water emulsion

5.1.1 Introduction

An emulsion is a thermodynamically unstable two-phase system consisting of at least two immiscible liquids, one of which is dispersed in the form of small droplets throughout the other, and an emulsifying agent. The dispersed liquid is known as the internal or discontinuous phase, whereas the dispersion medium is known as the external or continuous phase. If oils, petroleum hydrocarbons, and/or waxes are the dispersed phase, and water or an aqueous solution is the continuous phase, the system is called an oil-in-water (o/w) emulsion. An o/w emulsion is generally formed if the aqueous phase constitutes > 45% of the total weight, and a more hydrophilic emulsifier is used. Conversely, where water or aqueous solutions are dispersed in an oleaginous medium, the system is known as a water-in-oil (w/o) emulsion. W/O emulsions are generally formed if the aqueous phase constitutes < 45% of the total weight and a more lipophilic emulsifier is used.

The term "Multiple emulsion" was first introduced by Seifriz[128] to describe oil drops of an o/w emulsion containing droplets of water, or small oil globules inside the water drops of a w/o emulsion. The two major types of multiple emulsions are water-in-oil-in-water (w/o/w) emulsions where small water droplets are entrapped within larger oil droplets that in turn are dispersed in a continuous water phase, and oil-in-water-in-oil (o/w/o) emulsions containing small oil droplets within larger water droplets that are dispersed in a continuous oil phase. Because of the reservoir phase inside droplets of another phase that can be used to prolong the release of active ingredients, multiple emulsions are extensively applied in industries such as pharmaceutics and cosmetics.

Multiple w/o/w emulsions contain both w/o and o/w simple emulsion and require at least two emulsifiers to be present in the sample. A systematic approach

was developed to assist in making decisions about the amounts and types of emulsifiers needed to obtain stable products. The system is called the HLB (hydrophile-lipophile balance) system and has an arbitrary scale of 1 - 18. HLB numbers are experimentally determined for the different emulsifiers. If an emulsifier has a low HLB number, there are a low number of hydrophilic groups on the molecule and it will have more of a lipophilic character. The low-HLB emulsifier is dominantly hydrophobic and used for the primary w/o emulsion. The higher HLB emulsifier has a large number of hydrophilic groups on the molecule and therefore is dominantly hydrophilic. Usually it is dissolved in the outer continuous aqueous phase. The concentration ratio of these two surfactants is important to obtain a stable w/o/w emulsion[129].

Mentioning stability, emulsions are, by nature, physically unstable: that is, they tend to separate into two distinct phases or layers over time. Several levels of instability are described in the literature. **Creaming** occurs when dispersed oil droplets merge and rise to the top of an o/w emulsion or settle to the bottom in w/o emulsions. In both cases, the emulsion can be easily redispersed by shaking. **Coalescence (breaking or cracking)** is the complete and irreversible separation and fusion of the dispersed phase. Finally, a phenomenon known as **phase inversion** or a change from w/o to o/w (or vice versa) may occur.

For the stability of w/o/w emulsions, the most difficult feature to control is the osmotic flux of water molecules across the oil lamellae[130]. If the osmotic pressure is higher in the internal aqueous phase, water will pass into this phase leading to swelling of the internal droplets which eventually burst and release their contents into the external phase. If the reverse gradient exists, transfer of water from the internal to the external aqueous phase may cause shrinkage of the internal droplets. If the osmotic pressure difference across the oil layer is extreme, then passage of water is so rapid that almost immediate rupture of the oil drops with expulsion of the internal droplets occurs. When the oil layer ruptures, the inner aqueous phase disappears instantaneously, which is followed by mixing of the internal aqueous phase with the external aqueous medium, leaving a single oil drop. This appears to occur frequently if the oil layer is thin. Electrolytes and other additives including drugs can affect the stability of the w/o/w emulsion systems through osmotic effects.

Stratagems to suppress the osmotic effects in w/o/w emulsion systems include: 1) the use of a highly viscous oil phase, 2) the polymerization of the interfacial surfactant, and 3) the gelation of the oil phase. The second and third methods are often used to prepare hollow spheres based on w/o/w emulsion templates. In this chapter we will discuss the preparation of microcapsules by photo-crosslinking the photoreactive cinnamate-labeled nanoparticles in the oil phase.

5.1.2   Preparation of Water/Oil/Water emulsions

Three traditional methods are found in the literature to prepare double emulsions[131]: first, phase inversion[132]; second, two step emulsification[129]; third, mechanical agitation of a mixture of an aqueous solution of a hydrophilic emulsifier and an oil phase containing a lipophilic emulsifier[133].
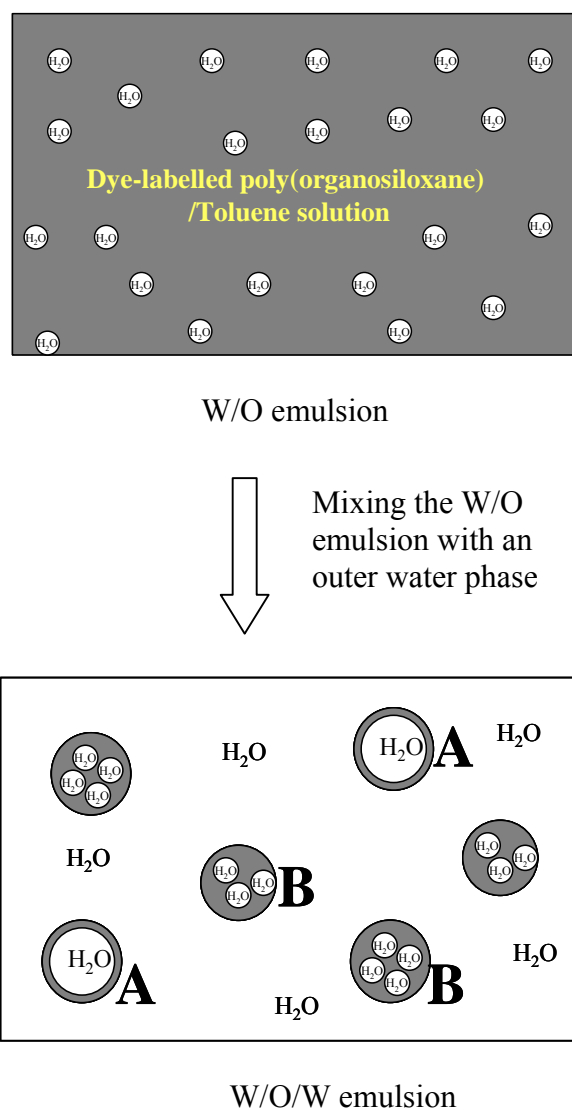

W/O emulsion

Mixing the W/O emulsion with an outer water phase

W/O/W emulsion

Fig. 5-1 Preparation of double emulsion by using 2-step w/o/w emulsification

93

The w/o/w emulsions in this thesis were prepared by the two-step procedure reported by Matsumoto[129]: the first step is preparation of a primary w/o emulsion, which is usually carried out in a high-shear device to produce very fine droplets in the presence of a hydrophobic emulsifier. This w/o emulsion is then mixed with an aqueous solution of hydrophilic emulsifier as the second step procedure for obtaining a w/o/w type dispersion. The two-step emulsification procedure[134, 135] is schematically described in figure 5-1. First, a W/O emulsion is produced by mixing water with a toluene solution containing the surfactant Span85 (figure 5-2a) and cinnamate-labeled poly(organosiloxane) nanoparticles (to form the crosslinked shell of the microcapsules). This water/oil mixture is homogenized with an Ultra-turrax homogenizer at 1.0×10^4 rpm to obtain a milky and viscous homogeneous w/o emulsion. To enhance the optical contrast between the different phases for fluorescence microscopic observation, either an oil-soluble or a water-soluble fluorescent dye is dissolved in the oil or water phase, respectively. Next, this W/O emulsion is added to an outer water phase containing the surfactant sodiumdodecylsulfate (SDS) (figure 5-2b), and the mixture is mildly stirred at 500 rpm to obtain the w/o/w emulsion. Principally, in a w/o/w emulsion prepared by this two-step procedure, the oil droplets may contain more than one water droplet, which is indicated in figure 5-1 by type **A** (single water droplet) and type **B** (multiple water droplets).
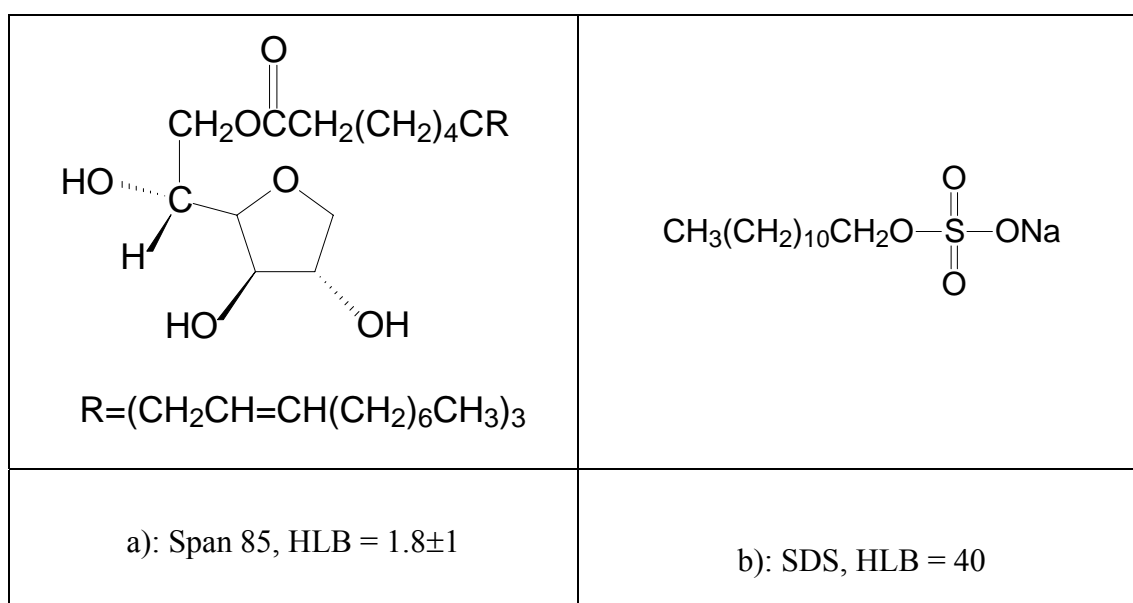

a): Span 85, HLB = 1.8±1	b): SDS, HLB = 40

Fig. 5-2 Chemical structure of Span85 and SDS

The two emulsifiers used for our w/o/w system are shown in figure 5-2. We chose span 85 as the hydrophobic surfactant because of its low HLB number, as well as the ability to increase the viscosity of the oil layer. SDS is a typical hydrophilic surfactant which has a very high HLB number and therefore is widely used to obtain o/w emulsions. The main role of the surfactant is to lower the energy required to increase the surface area so that spontaneous dispersion of water or oil droplets occurs and the system is thermodynamically stable. As a result, the emulsion stability increased with an increase in Span 85 concentration within a certain range. However, the primary emulsion in this case was too viscous to be effectively dispersed in the continuous aqueous phase to form a w/o/w emulsion under the agitation conditions used in the secondary emulsification process. On the other hand, at high concentration SDS will solubilize the hydrophobic surfactant and consequently cause disruption of multiple droplets. There is usually an optimum concentration and concentration ratio of the two emulsifiers. Based on several experimental variations, we obtained the following prescription for our w/o/w emulsions. (Table 5-1)

Table 5-1 Standard emulsion recipe for our w/o/w emulsion system

Emulsion type	Ingredient	Weight (g)
W/O emulsion	H_2O	1
	Span85/Toluene (12wt%)	1
	oil soluble CdSe or Water soluble CdSe or Fluorescein sodium	$\sim 1*10^{-8}$mol/l
W/O/W mulsion	W/O emulsion	0.2
	H_2O	1.794
	SDS	0.006

By using a high quantum yield fluorescent dye to enhance the contrast of oil and water phase, we can image the multidroplets of the w/o/w emulsion with the help of fluorescence microscopy. First, oil soluble fluorescent nanocrystals[136] with diameter around 7 nm were used to single out the oil phase. The structure and fluorescence spectrum are shown in the following picture (figure 5-3). The nanocrystal we used has a core shell structure: the core is consisting of cadmium selenide (CdSe) and emits strong fluorescence when irradiated. This core is surrounded by a shell of Zinc sulfide (ZnS) which increases both the quantum yield and the stability of nanocrystals. If the band offsets between the core and shell materials are such that the band-gap of the core is enclosed by that of the shell, then the electron and hole wave functions may be confined to the core region, reducing the probability for nonradiative decay via surface states and traps[136-138] and thus increasing the quantum yield of the nanocrystal. The nanocrystal is stabilized in organic solvent by octadecyl amine ligands.
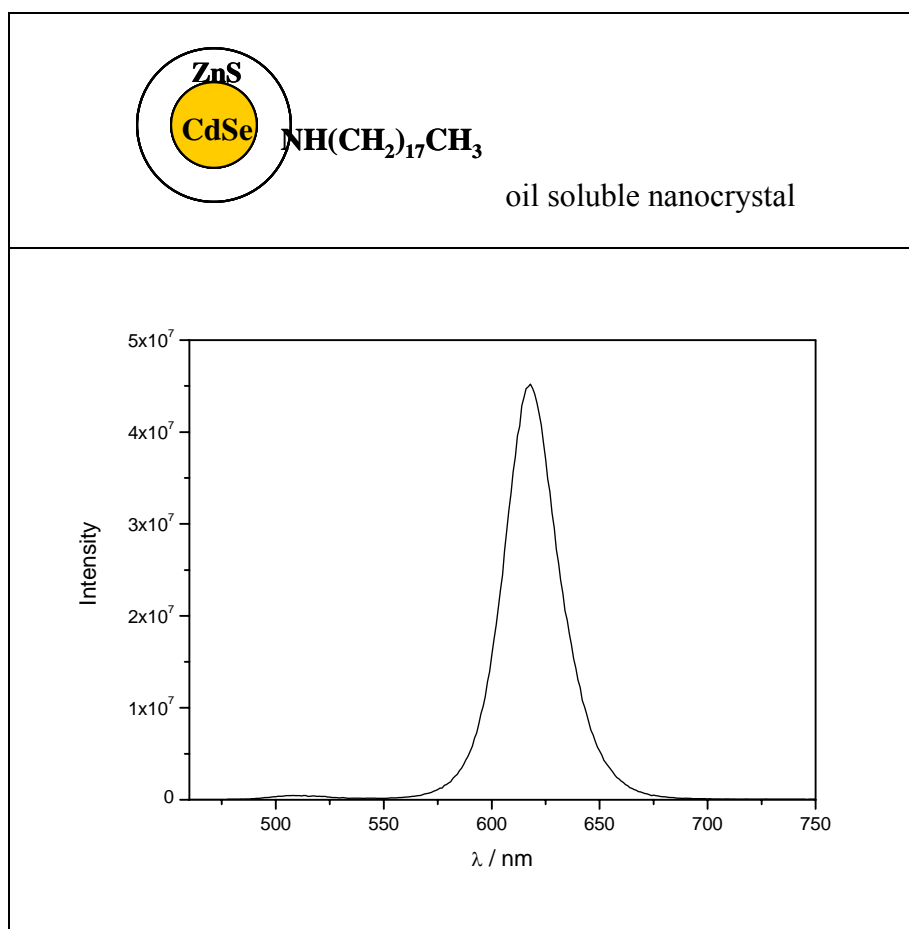

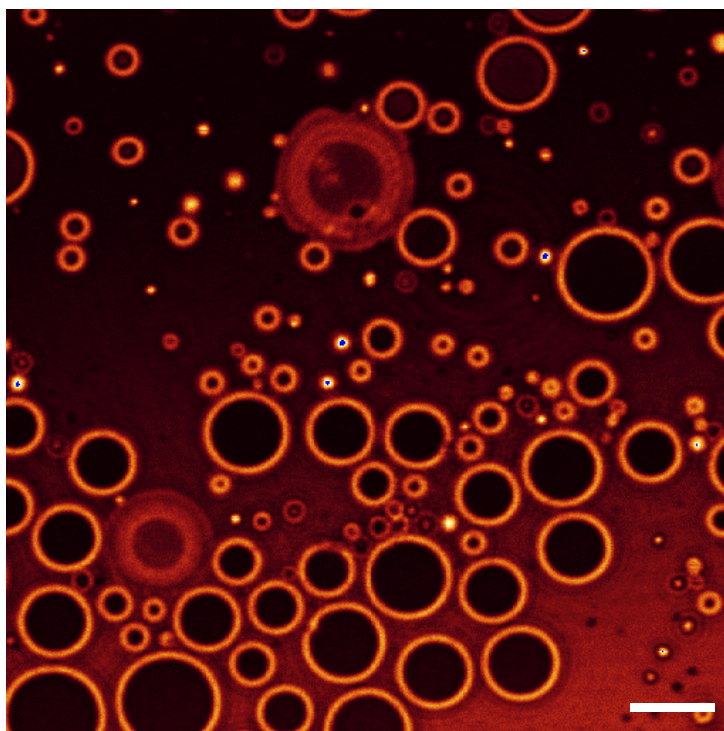**Fig. 5-3** Oil soluble CdSe nanocrystals and fluorescence spectrum

Fig. 5-4 Optical fluorescence micrograph of a typical w/o/w emulsion (scale bar 10 µm). The toluene shell of the microdroplets has been contrasted by fluorescent CdSe-Nanoparticles.

The oil soluble nanocrystals were dissolved in toluene before the emulsification procedure. The w/o/w emulsion prepared was directly observed by using fluorescence microscopy. An optical fluorescence micrograph of a typical water / oil (toluene) / water emulsion is shown in figure 5-4. The bright circles seen in the picture indicate the successful formation of a w/o/w double emulsion, and the inner and outer water phase are separated by a thin toluene layer. The average diameter of the microdroplets shown in the figure is about 8 µm, with a considerable size polydispersity.

We then used water soluble CdSe nanocrystals to stain the inner water phase. The structure and fluorescence spectrum of these water soluble CdSe nanocrystals are shown in figure 5-5. This nanocrystal has the same structure as the oil soluble nanocrystal, but the surface is coated with sodium thioglycolic acetate and therefore the particles can be dispersed in aqueous solution. This inner-water-phase-stained w/o/w emulsion enables us to observe the size and polydispersity of the inner water droplets. More importantly, dissolving the fluorescent dye into the inner water phase

equals to the procedure of encapsulation. Through the encapsulation the CdSe nanocrystals, the potential application of this w/o/w emulsion system could be explored.
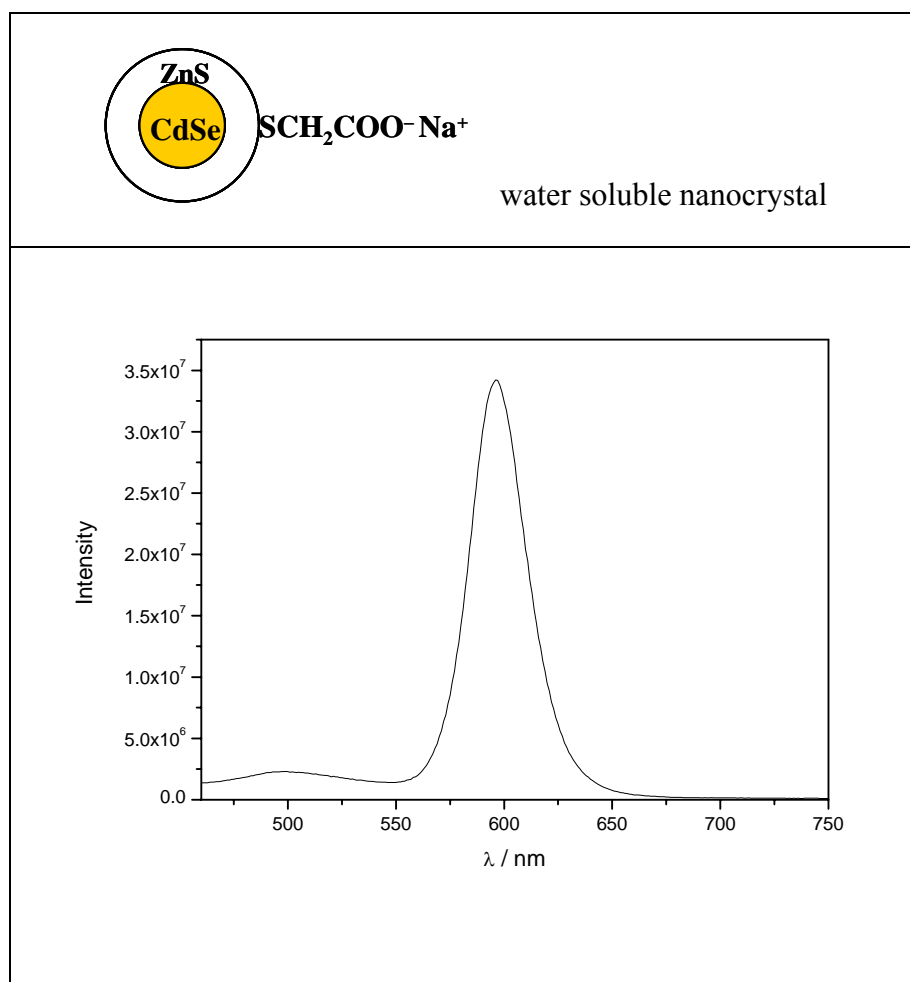
Fig. 5-5 Water soluble CdSe nanocrystals and fluorescence spectrum

The water soluble nanocrystals were dissolved in the inner water phase before the emulsification procedure. Directly after the emulsification, the w/o/w emulsion prepared was observed by using fluorescence microscopy. The optical fluorescence micrograph of this emulsion is shown in figure 5-6. The bright dots in the picture represent the inner water droplets, which is contrasted from the background by the water soluble fluorescent nanocrystals. This means the water droplets are safely enclosed by an oil shell and thus separated from the outer continuous aqueous phase.

Fig. 5-6 Optical fluorescence micrograph of a typical w/o/w emulsion (scale bar 10 μm). The inner water phase of the microdroplets has been contrasted by fluorescent CdSe-Nanoparticles.

Finally, another hydrophilic dye, fluorescein sodium (Figure 5-7), was used to stain the inner water phase. Due to its small molecular size compared to CdSe nanocrystals and electrolyte nature, the release of the fluorescein sodium from the inner to the outer water phase should be faster than for the CdSe nanocrystals.

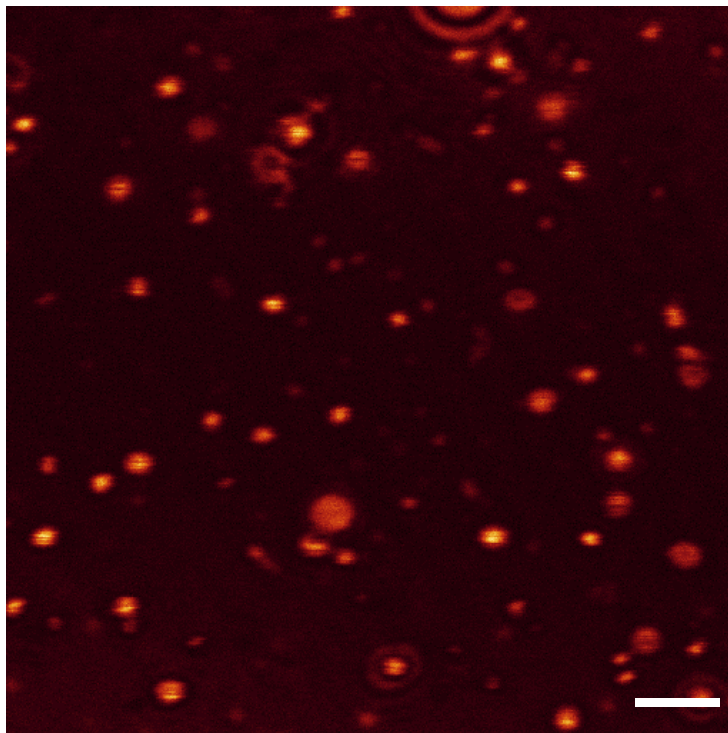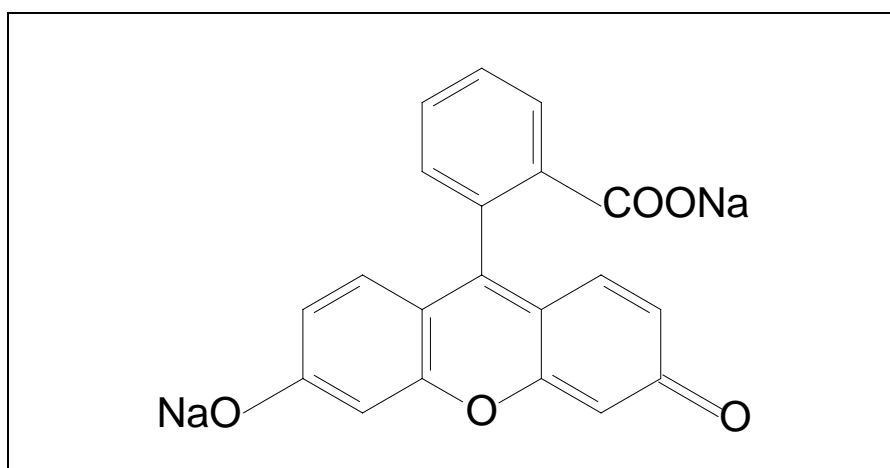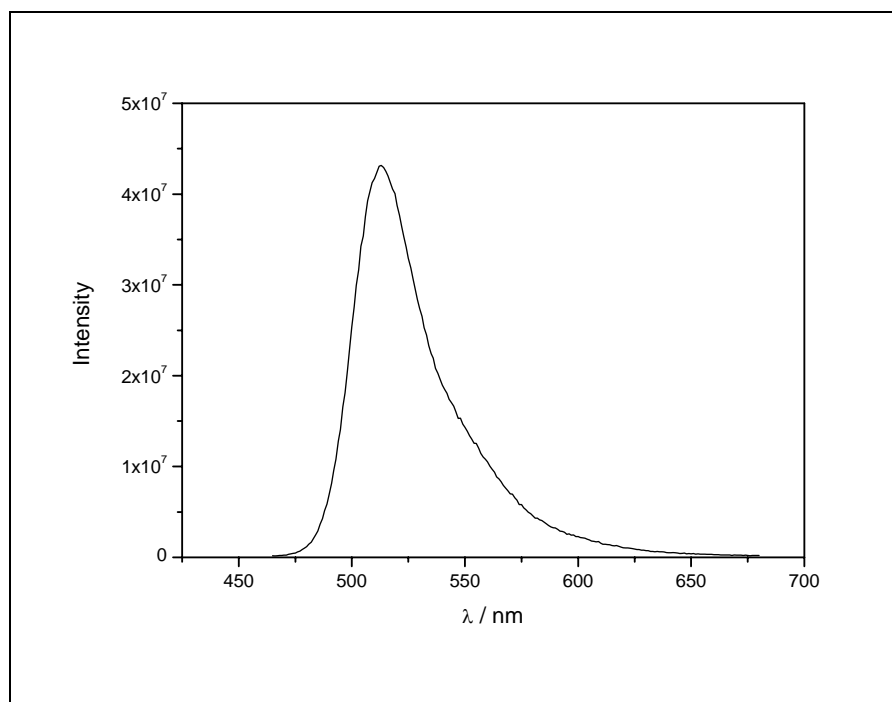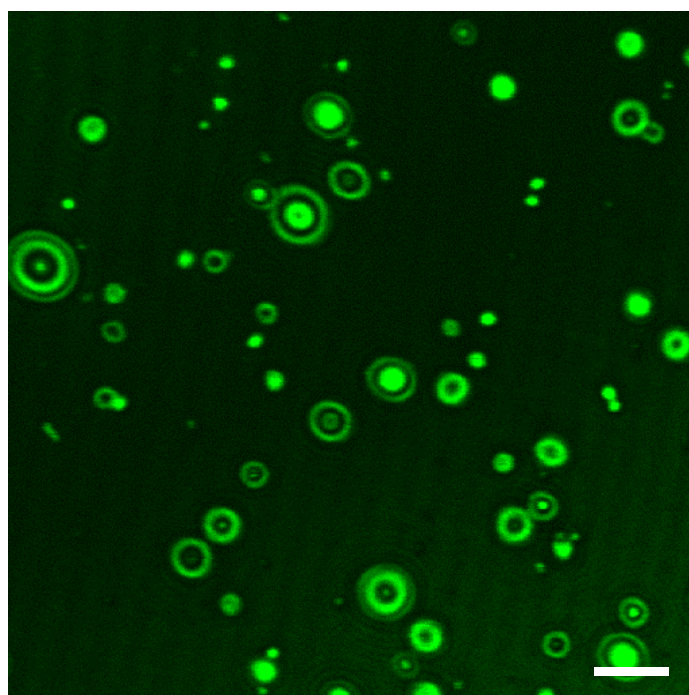**Fig. 5-7** Fluorescein sodium and its fluorescence spectrum

Figure 5-8 Optical fluorescence micrograph of a typical w/o/w emulsion (scale bar 10 μm). The inner water phase of the microdroplets has been contrasted by fluorescein sodium.

The optical fluorescence micrograph of the w/o/w emulsion (the inner water droplet was stained by fluorescein sodium) shows bright dots corresponding to inner water droplets containing fluorescein sodium, which means at least during the measurement time the fluorescein sodium was safely enclosed by the toluene-surfactant barrier. In figure 5-8, we can also find some bright "rings". We believe they are out of focus images of droplets, because the liquid film on the microscope slide is larger than the droplet size. Therefore for a given "snapshot" not all droplets are in the same in-focus position and some of them form these out of focus "rings".

As mentioned above, instability is always a problem for w/o/w emulsion systems. Our w/o/w emulsion system also suffered from instability: rapid evaporation of the toluene leads to the destruction of w/o/w emulsions within less than 4 hours. Fusion of the droplets also causes instability of our emulsions, macroscopic phase separation can be observed after a freshly prepared emulsion is kept for 4-5 hours. A freshly prepared w/o/w emulsion and an emulsion stored for 6 hours were observed using fluorescence microscopy (figure 5-9). The fluorescence micrographs show that the w/o/w emulsion changes from a stable dispersion to an irreversible separation and fusion of the dispersed phase.
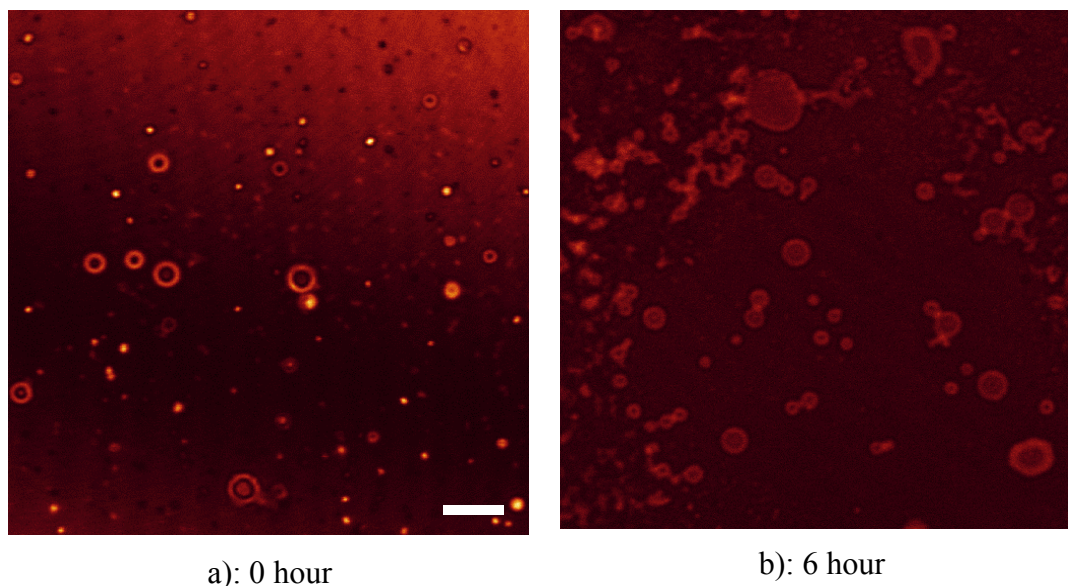

a): 0 hour

b): 6 hour

Fig. 5-9 Optical fluorescence micrographs for a typical w/o/w emulsion freshly prepared (a) and stored for 6 hrs after preparation (b) (scale bar 10 μm for both). The toluene shell of the microdroplets has been contrasted by fluorescent CdSe-Nanoparticles.

5.2 Photoclevable Microcapsules built from photoreactive polyorganosiloxane-µ-gels, based on a w/o/w emulsion template

In the previous part, we showed how we prepared w/o/w emulsions which can be used as a template for building microcapsules. Now we start to discuss the formation of photocleavable microcapsules using this approach.

5.2.1 Formation of Microcapsules

Our idea of forming photocontrollable microcapsules is shown in the following sketch. (Figure 5-10)
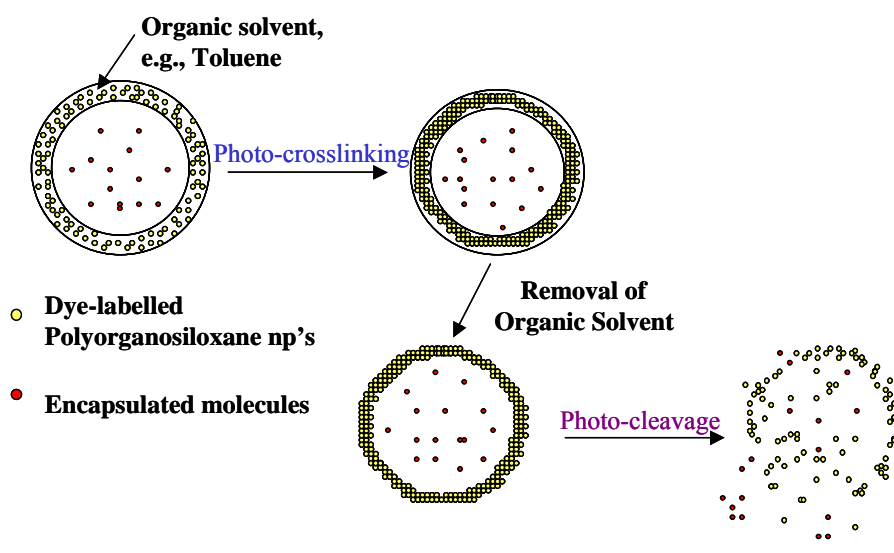
Fig. 5-10 Schematic synthesis path of preparing photodestructable hollow spheres by using a photocrosslinkable and photocleavable shell

First, through the preparation of a w/o/w emulsion as described in the last part, we can obtain "toluene vesicles" in which photoreactive dye-labeled-polyorganosiloxane-µ-gels are dissolved. Since the dye-labeled nanoparticles are insoluble in the aqueous phase, they are confined to the toluene layer. By irradiating this emulsion with UV light, the photoreactive nanoparticles will crosslink inside the toluene layer due to inter-particle photo-dimerization as described before. If the concentration of nanoparticles is sufficient and the irradiation time is long enough, clusters will grow until they form a continuous shell covering the whole droplet. Due to the spherical shape of the toluene vesicle, the dye-labeled nanoparticles therefore are shaped into a hollow spherical microcluster. It is notable that these microcapsules

can be photodegraded: since the cluster formation of the dye-labeled nanoparticles is reversible[139], the nanoparticle-clusters could also be broken up and therefore the microcapsules selectively destroyed by irradiation of the sample with uv-light of shorter wave lengths compared to the light used for fixing the micro-capsule structure. A potential application of the photocleavable microcapsules is indicated in figure 5-10. Guest molecules like drugs can be previously dissolved in the inner water phase and encapsulated. After the formation of microcapsules, these guest molecules can then be easily released by photocleavage of the microcapsule shell.

As we know, the w/o/w emulsions are not stable. However, irradiation of the droplets in aqueous dispersion allowed us to fix their structure by the formation of a crosslinked multilayer shell of tiny nanoparticles, as is proved by the scanning electron microscopy (SEM) pictures in figure 5-11. Clearly, the sphere-like structures shown in figure 5-11 agree nicely in size, shape, thickness and polydispersity with the emulsion depicted in figure 5-4. Therefore, we may state here that we have been successful in fixing the droplet structure and preparing solid crosslinked microcapsules, meanwhile the toluene itself certainly has evaporated. Some of the shells in figure 5-11 seem to be broken, which is attributed to the sample preparation and the drying procedures necessary for SEM. However, some capsules show indentations or even tiny holes which may be caused by the formation of multi-droplet structures within the water/oil/water-emulsion, i.e. tiny droplets fused with larger ones.

a

b
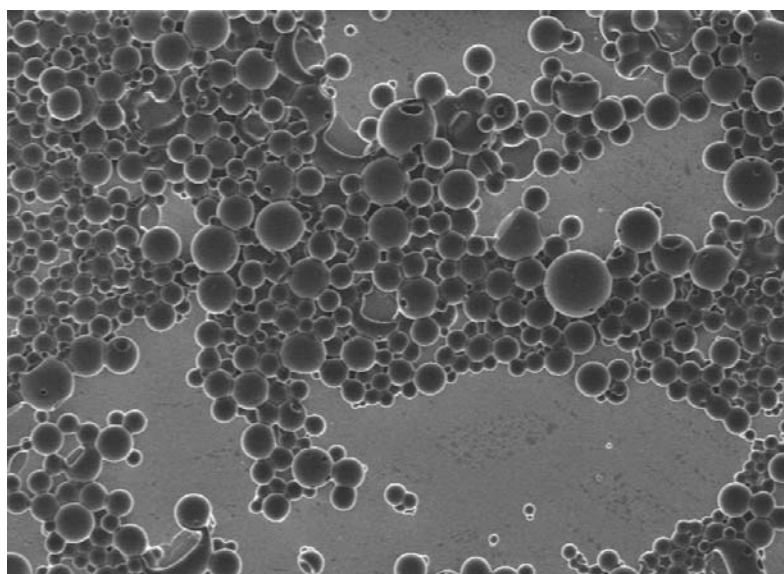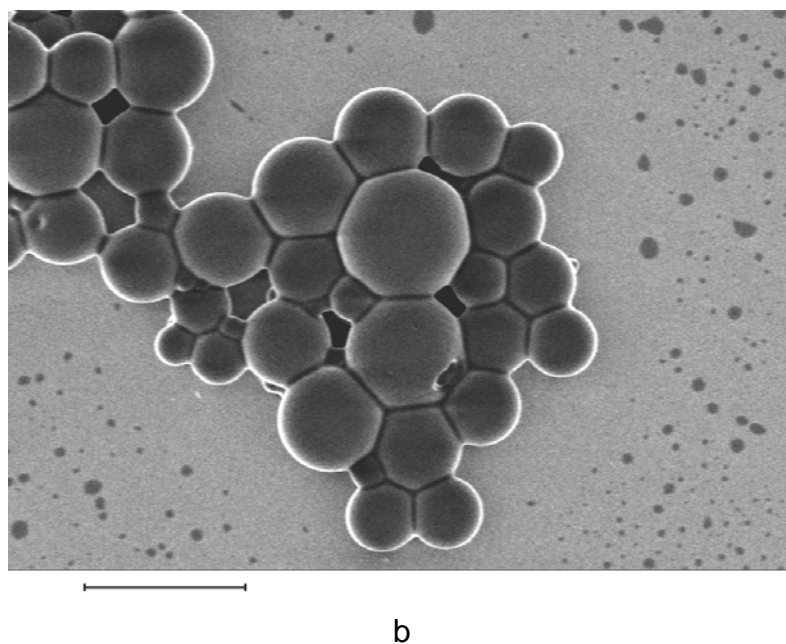
Fig. 5-11 Scanning electron micrograph of dried water/oil/water-emulsion-droplets (Cinem01, sample composition see table 5-2) after fixing their structure by photocrosslinking of the photoreactive nanoparticles within the toluene shell (scale bars 20 μm (a) and 10 μm (b)).

Table 5-2 Emulsion recipe for photoreactive microcapsules

Emulsion type	Ingredient	Weight (g)
W/O emulsion	H_2O	1
	cin04	0.1 (variable)
	Span85/Toluene (12wt%)	0.9
W/O/W mulsion	W/O emulsion	0.2
	H_2O	1.794
	SDS	0.006 (variable)

Table 5-3 Variable SDS and nanoparticle contents for different emulsions

Sample No.	SDS/outer water phase(wt%)	Cinem0303/oil phase (wt%)
Cinem10a	0.0033	10
Cinem10b	0.0066	10
Cinem05	0.0033	5

The emulsion composition used for preparation of the microcapsules shown in figure 5-11 is given in table 5-2. Usually, droplet size and thickness of the oil shell in w/o/w double emulsions can be adjusted by the sample composition, which will in turn change the size of the microcapsules. We prepared an alternative microcapsule sample (cinem10b) by varying only the concentration of the hydrophilic surfactant SDS (increased by a factor of 2 compared to sample cinem10a shown in figure 5-11 (Table 5-2)). Because more surfactant tends to stabilize more droplets while the volume of the w/o emulsion is fixed, the size of the droplets thus should decrease. The structure of the droplets was again fixed by UV irradiation of these w/o/w emulsions. The SEM pictures of these microspheres is shown in figure 5-12. Obviously the average size of the microspheres is smaller than that in figure 5-11, despite the polydispersity of the size distribution. This nicely agrees with the theoretical estimation.

a
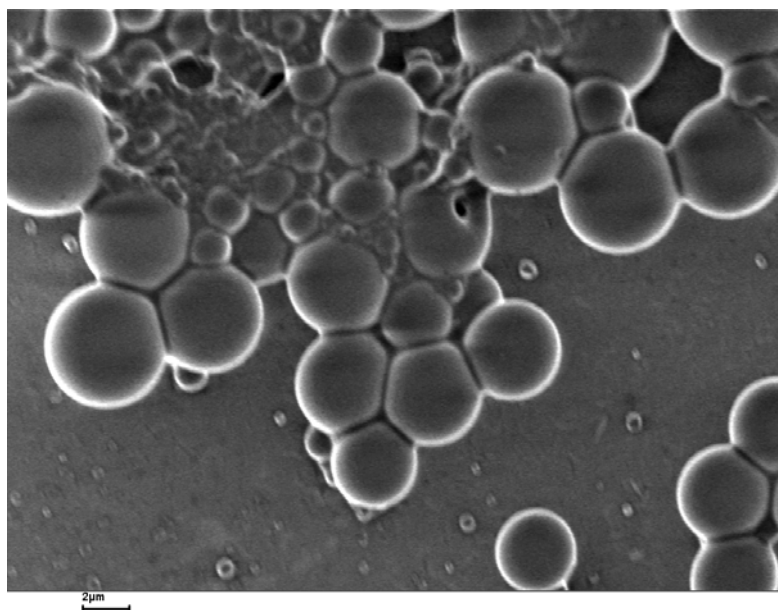
b

Fig. 5-12 Scanning electron micrograph of dried w/o/w emulsion-droplets (cinem10b) after fixing their structure by photocrosslinking of the photoreactive nanoparticles within the toluene shell (scale bars 20 μm (a) and 2 μm (b)).
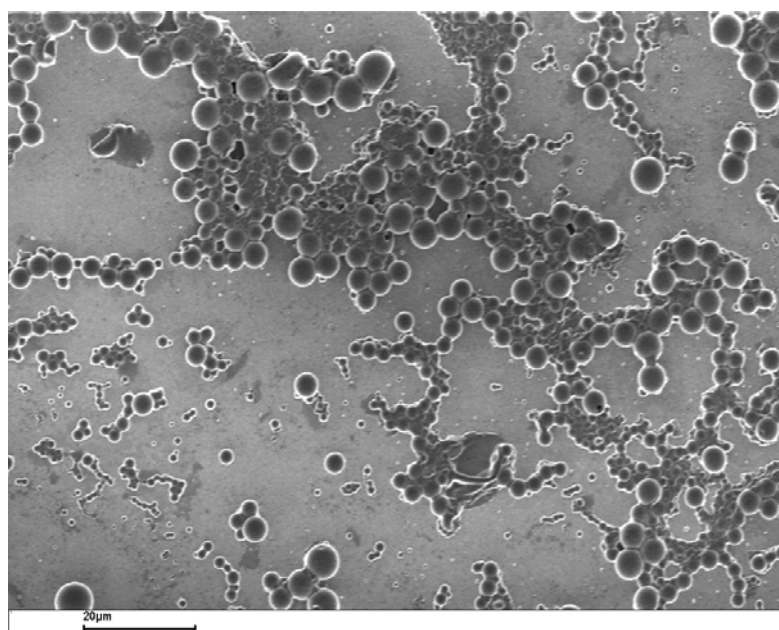
Compared to figure 5-11, the microspheres in figure 5-12 show higher polydispersity, and many very small spheres (< 1 μm) can also be found. Such a high polydispersity might limit the potential application of these microcapsules as a well-defined system. We therefore prefer to use the emulsion recipe with the lower SDS concentration (see Table 5-2) to obtain microcapsules for a more detailed investigation of encapsulation and release properties. It should be noted that in principle the size polydispersity can be decreased using more sophisticated techniques for preparation of the w/o/w-emulsion, like SPG emulsification (see above and [140-147]). For example, we tried to reduce the polydispersity by simply filtering the w/o/w emulsion through a 0.45 μm membrane filter. The resulting sample was observed by SEM and shown in figure 5-13. It is obvious that the microspheres formed after filtration have smaller diameters and the size polydispersity was reduced compared to the results shown in figures 5-11,12.
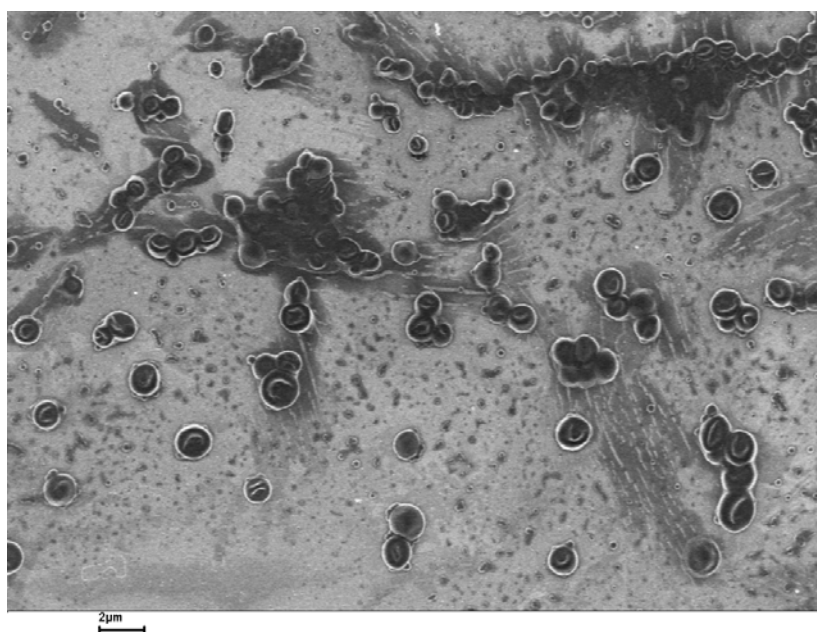
a
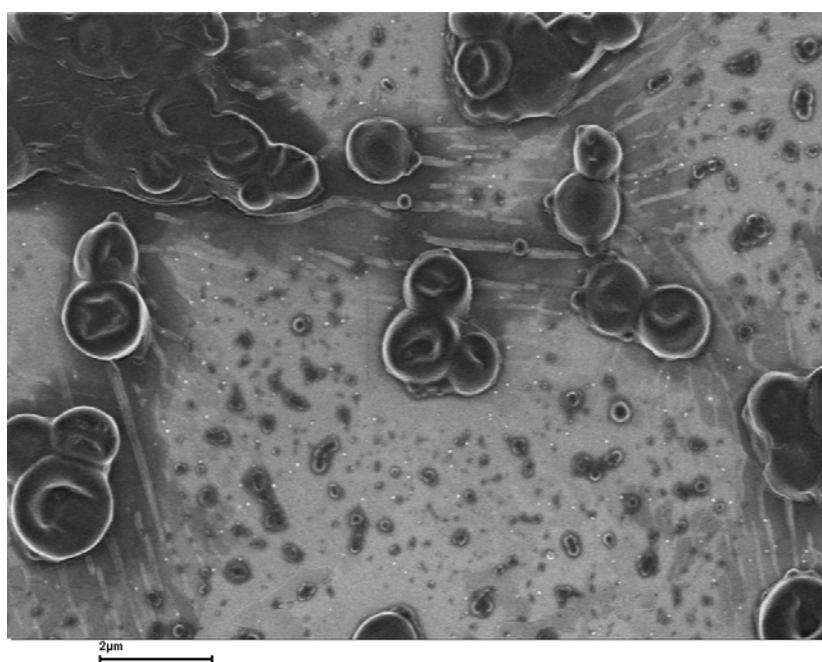
b

Fig. 5-13 Scanning electron micrograph of dried w/o/w emulsion-droplets (cinema10a, filtered through 0.45 µm membrane) after fixing their structure by photocrosslinking of the photoreactive nanoparticles within the toluene shell (scale bars 2 µm).

The filtered sample, however, shows microcapsules with an interesting "doughnut" shape instead of the spherical shape. This "doughnut" shape could be caused during extrusion by several factors. First, because the pore size of the membrane filter (0.45 μm) is much smaller than the average droplet size (~ 8 μm), we needed high pressure to squeeze the emulsion through the membrane even though the droplets were still not solid microspheres before irradiation. The high pressure then could force the highly concentrated particles within the toluene layer to fuse together and form a conglomerate. Secondly, when a compressed fluid was extruded, it would expand after it leaves the membrane pore. The expansion together with the fusion of particles transferred the original W/O/W droplets to a "doughnut" shape as shown in figure 5-13. The conglomerates first obtained by fusion of the nanoparticles seem to be very rigid and to need a long time to relax and redisperse into the toluene phase. Otherwise, the liquid droplet should quickly reform to spherical shape after being released from the extrusion, and the final microcapsules should also be spherical after UV irradiation. In conclusion, we believe the "doughnut" shape couldn't relax before the UV irradiation, resulting in the unusual microcapsule image shown in figure 5-13.

The above result shows one possibility of reducing polydispersity, though the sample might lose its original isotropic spherical structure during the process. At present, we are more interested in establishing a principally new system of photocontrollable microcapsules at this stage, wherefore reducing polydispersity is not a major issue and has not been studied in more detail during the limited time of this thesis.

5.2.2 Photocleavage of Microcapsules

As schematically shown in figure 5-10, the shell of the microspheres could be broken due to the reversibility of photocrosslinking. The broken microspheres can reveal the inner structure of the microsphere shell, and more important, photocleavable microspheres will open up a route to the potential application as a controlled release system.

While the optimum conditions for potential applications have yet to be identified, we already have been able to prove the photodestructability of our new microcapsules using the samples at hand. To de-crosslink the micron-sized spherical nanoparticle shells, the microcapsule solution from sample cinem10a (table 5-3) has

been irradiated with UV-light of wavelength 254 nm, as described in detail in the experimental part. Figure 5-14 shows the development of the optical transparence of a typical emulsion with increasing irradiation time: starting with a highly turbid emulsion corresponding to micron-sized objects immersed in the aqueous phase, after 6 hours of irradiation we end up with a seemingly transparent solution. Also, some white precipitate is found close to the bottom of the sample cell. These findings are explained as following: before de-crosslinking, the amount of surfactant present in the W/O/W emulsion is sufficient to stabilize the otherwise insoluble microcapsules. During de-crosslinking, however, the shells are destroyed and therefore the nanoparticle-water-interface increases to such a large value that the amount of surfactant is no longer sufficient to maintain a stable emulsion. As a consequence, most of the smaller nanoparticle clusters and larger fragments of the microcapsule shells, which become insoluble in water without their stabilizing surfactant layer [148-150], precipitate either to the glass wall or to the bottom of the sample cell, and the remaining aqueous phase becomes optically transparent.
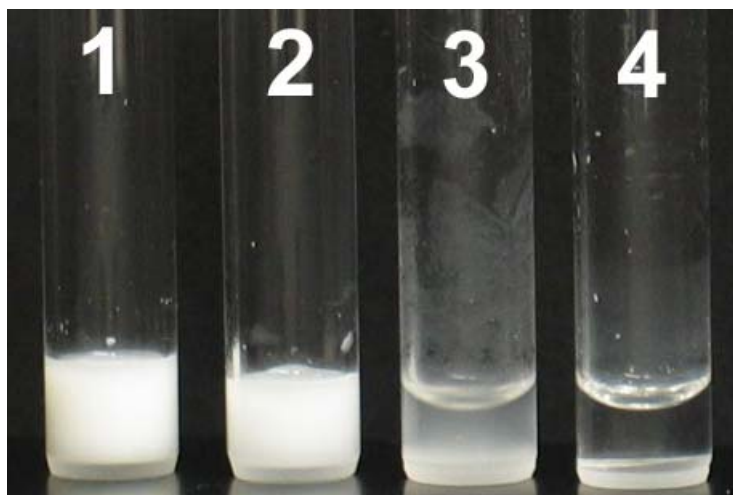
Fig. 5-14 Sample cell containing an aqueous dispersion of crosslinked microcapsules, after 0, 2, 4 and 6 h irradiation (1 – 4) with uv light suitable for decrosslinking.

To prove this macroscopic indication of a successful photodestruction of our crosslinked microcapsules, a closer look into the detailed structure of the capsules and the fragments themselves, as obtained by scanning electron microscopy, is shown in figure 5-15. Pictures 5-15a and 5-15b clearly show large irregular cracks within

microcapsules of diameter about 4 μm. Most interestingly, there are many small spherical clusters of size 100 nm to 1μm visible in the picture. Although, as stated above, our microcapsules are rather polydisperse, these smaller particles (size < 1 μm) seem to originate mainly from the photodestruction itself and not from the original w/o/w emulsion (see figs. 5-11 for comparison, where no large number of such smaller spherical objects can be seen). Our assumption that these smaller spherical clusters are fragments of the microcapsule shells is underlined by picture 5-15b, which shows spherical gaps of size comparable to the small spherical particles (here: 0.5 – 1 μm) within the crack of a larger microcapsule. With larger magnification, the observation that the small spherical particles originate from the cracked shell of the microcapsule becomes even more obvious (figures 5-15c, d). Still larger magnification shows that the shell of an individual microcapsule consists of a close packed layer of crosslinked nanoparticles with a layer thickness of about 40 nanoparticles (figure 5-15e), which agrees nicely with the average amount theoretically calculated from the sample composition (that is, total amount of nanoparticles, amount of toluene and average droplet size in the original w/o/w-emulsion). Within this thin shell, however, there are tiny spherical holes of only about 100 nm in diameter clearly visible (figure 5-15f). These correspond nicely to the smallest spherical particles already seen in figure 5-15a and b, one of which very clearly can be identified in figure 5-15e on top of the broken microcapsule shell. We therefore conclude here that the shell of the microcapsules, although it seems to be built up by closely packed nanoparticles, nevertheless is not homogeneously crosslinked. Photocrosslinking within the w/o/w-emulsion seems to lead first to the formation of strongly crosslinked spherical nanoparticle clusters of diameter 100 – 200 nm due to diffusion-controlled aggregation. This average cluster size agrees very well with our previous results obtained by irradiation of pure nanoparticle solutions in toluene [127]. Upon evaporation of the thin toluene layer during continued irradiation, these smaller clusters become fused together to form a less tightly crosslinked (compared to the diffusion-controlled clusters) micronsized shell. If the process is reversed, decrosslinking most probably "cuts" the fewer chemical bonds between these small clusters, while a considerable fraction of the larger number of chemical bonds between individual nanoparticles within the small clusters may remain intact. This explains what is seen in figure 5-15, that is the existence of many small spherical clusters not found previous to photocrosslinking of the W/O/W-emulsion (see fig. 5-

11), and the indication that the cracks within the microscopic shells clearly show missing spherical objects (figures 5-15 b-d).

a

b

c

d

e

f

Fig. 5-15 Scanning electron micrographs of a dried solution of microcapsules (from 10 wt% nanoparticle solution) after destroying the previously fixed shell structure by photocleavage of the photoreactive nanoparticles within the shell. (scale bar 1 μm (a,b), 0.2 μm (c,d), and 0.1 μm(e,f)).

The mechanism of shell formation and photodegradation is schematically shown in figure 5-16. The route can be described as single particles → clusters → continuous shell → clusters → fragments of microcapsules.
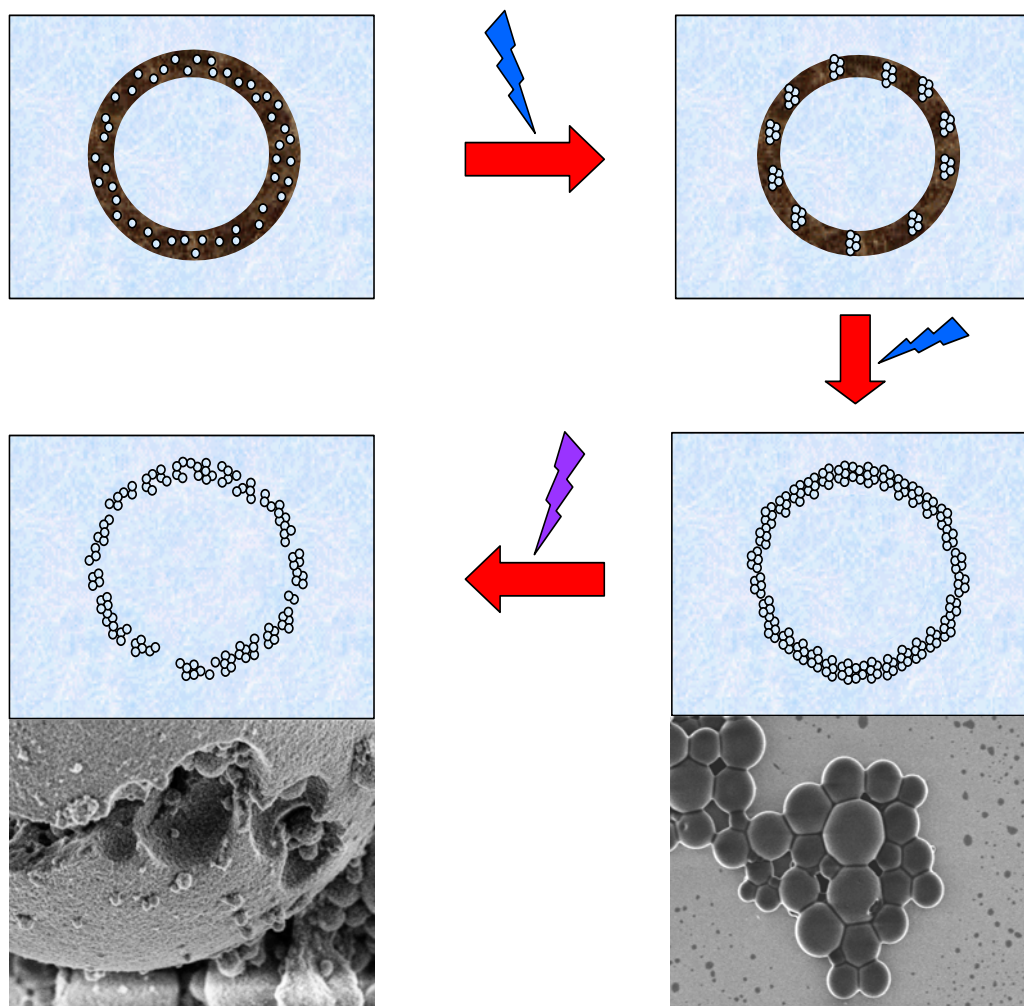
Fig. 5-16 possible mechanism for the formation of microcapsule shells from nanoprticles and the photodegradation of the microcapsule shell

5.2.3 Controllable Shell Thickness of Microcapule

In principle, the shell thickness of microcapsules depends on the concentration of nanoparticles if the emulsion composition is fixed. Figure 5-17,18 show SEM pictures of photo-decrosslinked microcapsules (from samples cinem10a and cinem05) which have been prepared using nanoparticles of different concentration in the oil phase. As shown in table 5-3, sample cinem05 used half the amount of nanoparticles compared to sample cinem10a. Clearly, the shell of microcapsules cinem05 in figure 5-18 is much thinner and also seems to be more flexible than the thicker shell of the

microcapsules cinem10a seen in fig. 5-17. Due to the polydispersity of the microdroplets, the shell thickness of the microcapsules cannot be exactly controlled, hence the shell thickness difference of these two types of microcapsules is not exactly proportional to the difference of the nanoparticle concentrations.

This illustrates another important aspect of our new promising system of photodegradable microcapsules: shell thickness and crosslink density, and therefore mechanical and optical stability of the microcapsules, can be adjusted simply by the amount of nanoparticles.
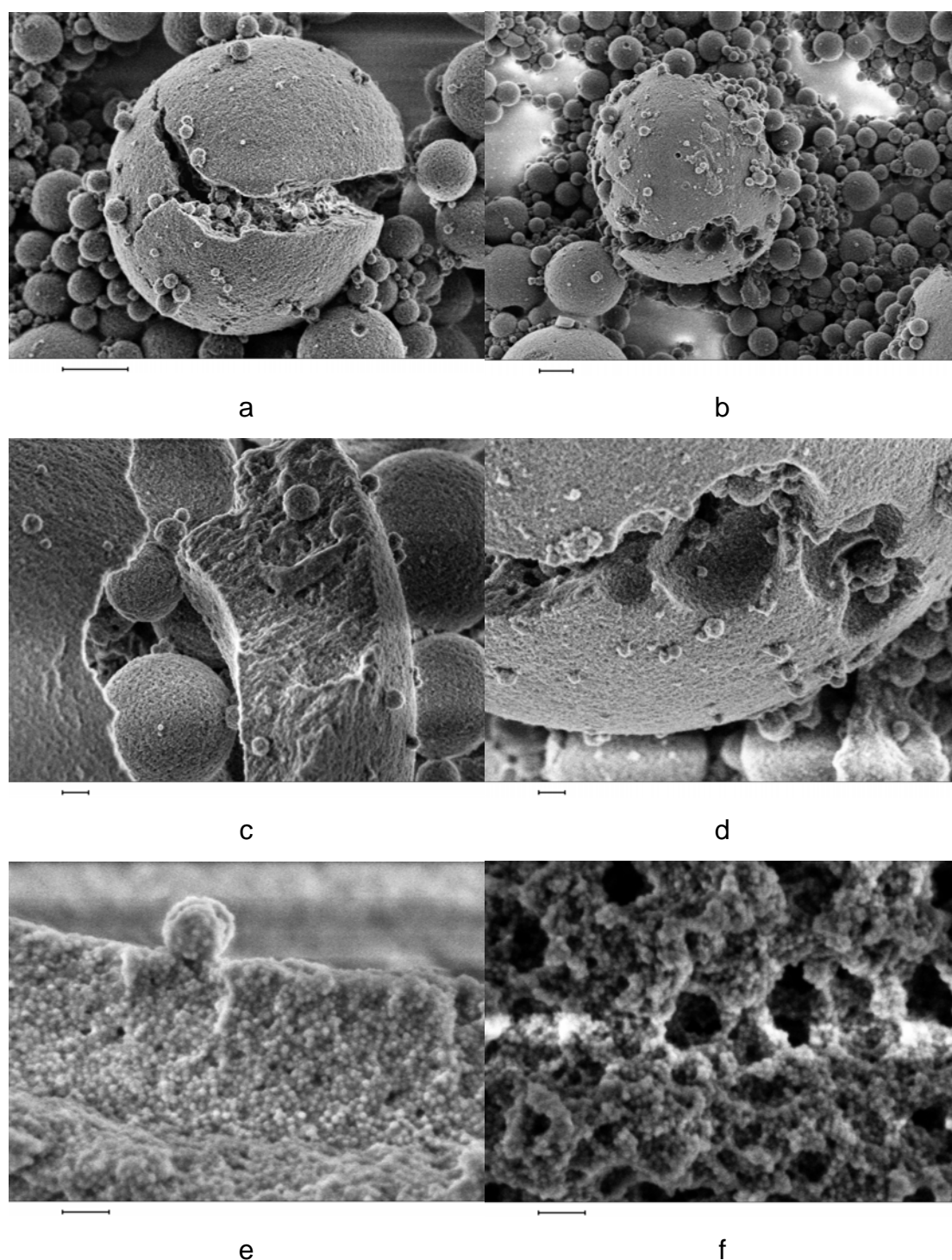

a   b
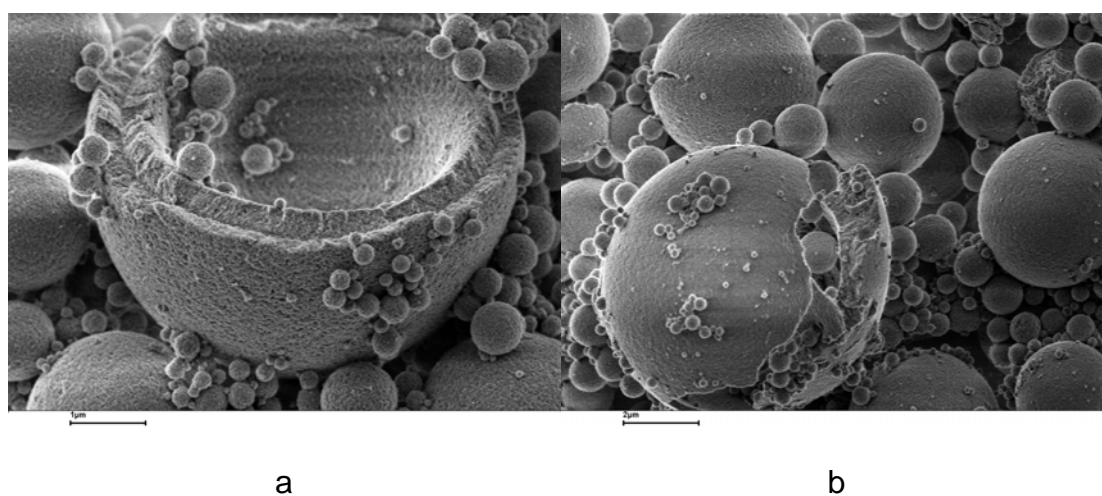
Fig. 5-17 Scanning electron micrographs of a dried solution of microcapsules (from cinem10a) after destroying the previously fixed shell structure by photocleavage of the photoreactive nanoparticles within the shell. (scale bar 1 µm (a) and 2 µm (b)).

a   b
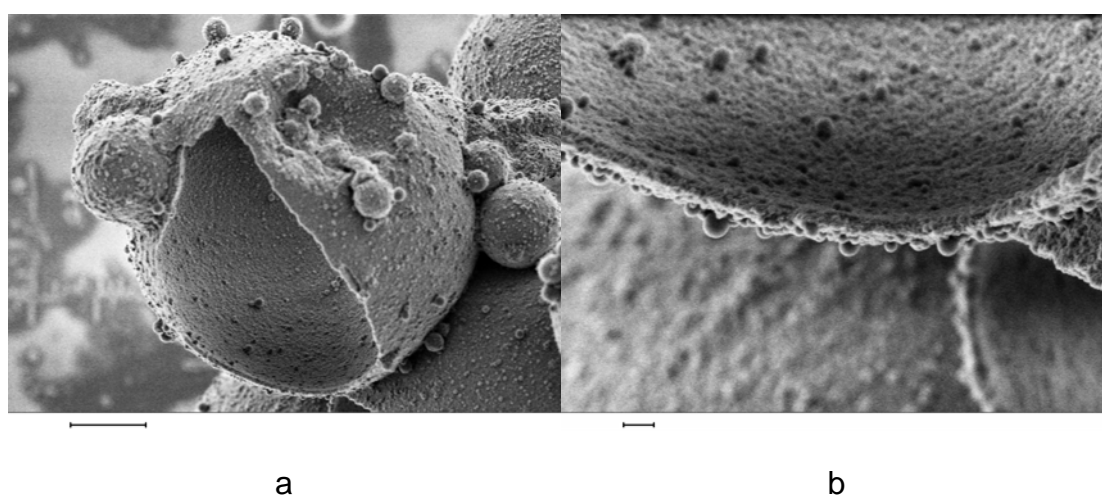
Fig. 5-18 Scanning electron micrographs of a dried solution of microcapsules (from cinem05) after destroying the previously fixed shell structure by photocleavage of the photoreactive nanoparticles within the shell. (scale bars 2 µm (a) and 0.2 µm (b)).

113

In this chapter we showed how photocrosslinking of nanoparticles within water-oil-water emulsion leads to a promising new species of photoreversible microcontainers. The inner water droplet of these emulsions may contain drugs, dyes or other water-soluble components, leading to filled containers. Thickness, mechanical stability and light resistance of the container walls can be controlled in a very simple way by the amount of nanoparticles present during the crosslinking reaction. The major additional advantage of our new system is the reversibility of the photocrosslinking: irradiation of the microcontainers with UV light cracks the chemical bonds between the nanoparticles and therefore leads to destruction of the containers, opening up a pathway to controlled release of the enclosed components. Microencapsulation has attracted a lot of interest because its potential use ranges from controlling chemical reactions on a very small scale ("laboratories on a chip") to drug transport and controlled drug release. For this purpose, we need to further our study into exploring the potential application of the microcapsules we prepared, especially in respect to encapsulation and release.

6 ENCAPSULATION AND RELEASE TEST

Nanoparticles may lead to higher order structures, for example hollow microspheres. One of the important applications of such hollow spheres[30, 31] is their capability of encapsulating guest molecules, and the controlled release behaviour. Controlled delivery technology represents one of the frontier areas of science, which involves multidisciplinary scientific approaches from the fields of chemistry, material science, engineering, pharmacology and biological science. The advantages of controlled release compared to conventional dosage forms include: delivery to the required site; delivery at the required rate; reduced dangers of overdose, or side effects; and also economic advantages by virtue of more efficient dosage at the expense of possibly more complicated fabrication. The field of the intelligent drug delivery technology has grown and diversified rapidly in recent years. In those systems the drug or the substance of model drug were released with an on–off switching mechanism in response to a narrow change of environmental stimuli signals, such as temperature[32], pH[33], light[34], electric field[35], etc.. Concerning the intelligent drug delivery system, the preparation and applications of the stimuli-responsive materials appears to be very important.

A number of controlled release systems have been developed using polymers[151], and some of them are already in commercial production. For instance, biodegradable porous microspheres have been used extensively as drug delivery systems for bioactive proteins and anticancer drugs[152]. Drug release from these microspheres is usually based on diffusion. Hydrogels have also received significant attention as delivery vehicles on account of their acceptable biocompatibility and controllable permeability[153, 154]. For controlled delivery applications, these materials are particularly suitable to deliver entrapped drugs in aqueous media and can regulate drug release by controlling gel swelling and crosslinking density. Certain hydrogels undergo phase transitions, demonstrating reversible large swelling-deswelling behaviour in response to environmental changes including solvent composition, ionic strength, pH, temperature, electric field, and light. These polymer matrices may well be able to achieve sustained and pulsatile drug release strategies using external stimuli.

Another important controlled release system are microcapsules. A typical approach to controlled release is to encapsulate or contain the drug entirely within the microcapsules. The w/o/w multiple emulsion method which we have used is particularly suitable for the encapsulation of highly hydrophilic drugs, it has great industrial attractiveness due to its comparatively simple preparation method[155]. Many research results show effective entrapment of water soluble ingredients in w/o/w emulsions and their prolonged release. For example, Engel et al.[156] immobilized insulin in the inner aqueous phase of a w/o/w emulsion to improve the efficacy of the intestinal absorption.

The new polyorganosiloxane microcapsules described in this thesis (see chapter 5) have several advantages:

(i)   polyorganosiloxane nanoparticles offer a biocompatible, stable drug carrier system;

(ii)   drug loading is extremely simple using a solution of the guest molecules as inner water phase of the W/O/W-emulsion;

(iii)   a wide range of guest molecules (monomers, polymers, nanoparticles) could be encapsulated;

(iv)   the shell of the microcapsules can be broken in a controlled way;

(v)   their optical and mechanical properties are easily adjustable.

Due to the microscopic destruction, also quite large substances can be encapsulated and released in contrast to merely diffusion controlled systems. The basic idea of encapsulation and release using our microcapsule system is shown in figure 6-1: at the first step, the guest molecules dissolved in the inner water phase can be readily encapsulated through the w/o/w emulsification and the photocrosslinking of the microcapsule shells; secondly, the guest molecules will be released from the microcapsules when the shells are photocleaved and broken. To investigate the encapsulation efficacy and the release behaviour, the amount of the guest molecules encapsulated and released has to be quantified. UV and fluorescence spectroscopy are conventional methods to quantify the concentration of organic molecules. However, most organic molecules cannot survive the strong UV light during the process of photocrosslinking and photocleavage, which greatly increases the difficulty of the release study of our photocleavable microcapsules, and also, to be honest, limits their

potential application. Hence, it is necessary to find a suitable guest molecule that shows both UV resistance and also sufficient sensitivity in photo-physics.
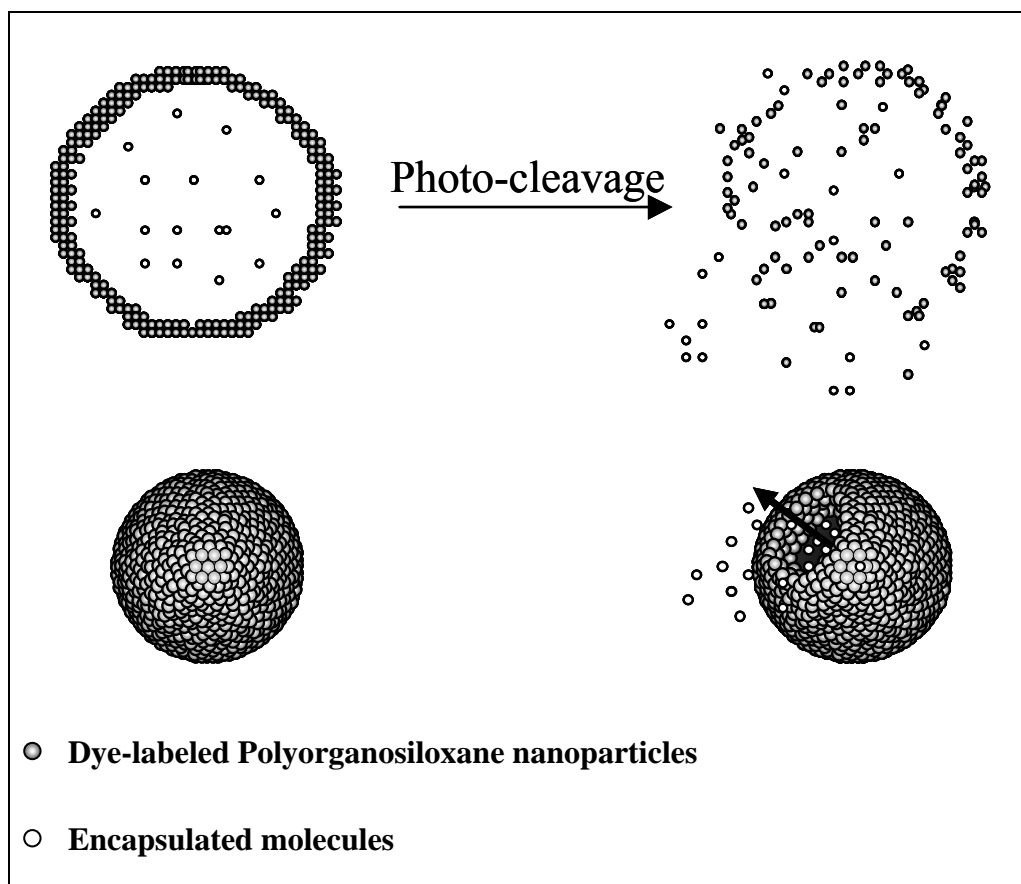
Fig. 6-1 Scheme for the release of encapsulated guest molecules after photocleavage of the microcapsule shell.

6.1. Release reagent study

To illustrate the release properties of our new microcapsule system we used several different chemical compounds as encapsulated guest molecules. These are: amylose (figure 6-2), Zinc Chloride ($ZnCl_2$), and β-cyclodextrin.

Amylose is one component of starch. The structure of amylose consists of long polymer chains of glucose units connected by an alpha acetal linkage, and amylose forms a colloidal dispersion in water. It is well known that starch shows a deep blue color in the presence of iodine. Amylose in starch is responsible for this deep blue color, which comes from the amylose-iodine complex when iodine molecules slip into the amylose coil. If the amylose can be encapsulated into our microcapsule, the

release behaviour of amylose can be easily monitored by observing the color change of the solution after adding iodine solution. However, the solubility of amylose in water is limited, so that the concentration of amylose in the whole microcapsule solution is too low to be sensitive enough to detect the difference before and after release.
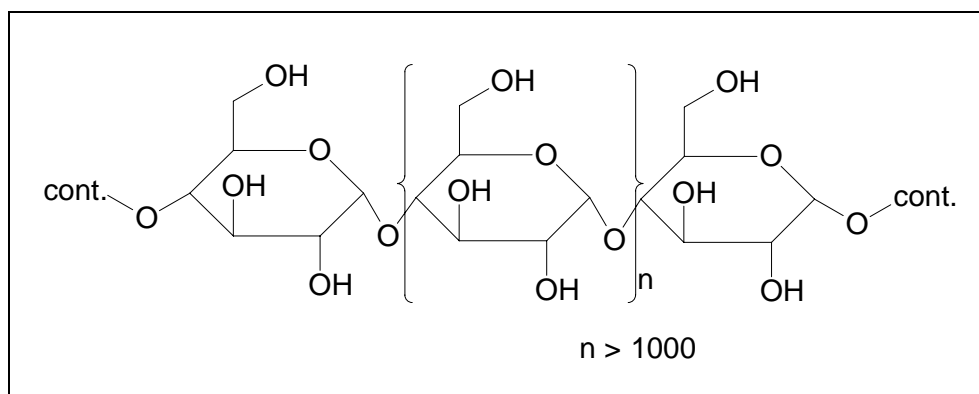
Fig. 6-2 Amylose

Another guest molecule, Zinc chloride ($ZnCl_2$), has a higher solubility in water which allows efficient encapsulation. Meanwhile, as a transition metal, Zn^{2+} can form complexes with organic molecules which provide a sensitive assay for Zn^{2+}. For example, Zn^{2+} forms a complex with 8-quinolinol (figure 6-3) in water solution which shows a characteristic fluorescence emission maximum at 517 nm. Thus, the detection of Zn^{2+} ions released from the microcapsules can be carried out by using 8-quinolinol as indicator[157, 158]. However, we detected Zn^{2+} in the outer water phase of the microcapsule solution before we performed the photocleavage experiment. If we tried to remove this Zn^{2+} in the outer water phase by dialyzing the microcapsule solution against pure water, then no Zn^{2+} was detected after photoleavage. These results mean Zn^{2+} is too small to be enclosed inside the microcapsules and is continuously released because of diffusion. Though prolonged release could be another interesting topic for our new microcapsule system, we didn't investigate in detail the kinetics of the release of $ZnCl_2$ from unbroken microcapsules because we are more interested in the optically controlled release properties of the photocleaved microcapsules.
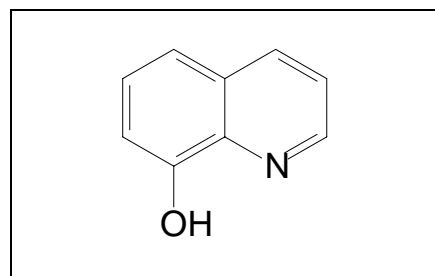
Fig. 6-3 8-quinolinol

Our first successful release experiment was carried out by using cyclodextrin as an encapsulated guest molecule. Because of the suitable molecular size (~1 nm) and reasonable water solubility, cyclodextrin became a perfect candidate for both encapsulation and release tests. Also, cyclodextrin has very interesting photophysical properties which make possible quantitative release experiments[159].

6.2. Photophysics of cyclodextrin inclusion complexes[160]

Cyclodextrins are cyclic oligosaccharides with six to eight D-glucose units linked by α-1,4 bonds. The common hexamers, heptamers, and octamers are identified as α-, β-, and γ-cyclodextrin[161]. Figure 6-4 is the schematic representation of the structural feature of β-cyclodextrin (the inner diameter of the cavity is about 0.78 nm), the coupling of glucose moieties gives cyclodextrins a rigid conical structure with a hollow interior of a specific volume. Cyclodextrins display various characteristic chemical and physical properties due to their cyclic nature when compared to the flexible open-chain analogues. The most specific property is their ability to form inclusion complexes in aqueous solution. A distinguishing feature of these host systems, however, is the existence of finite size cavities or pores that lead to shape selectivity concerning the molecules they include. Consequently, there is intense interest in the characterization and exploitation of the host-guest complex properties, i.e., the driving force for binding and the binding specificity as well as the photophysics of inclusion complexes.

119
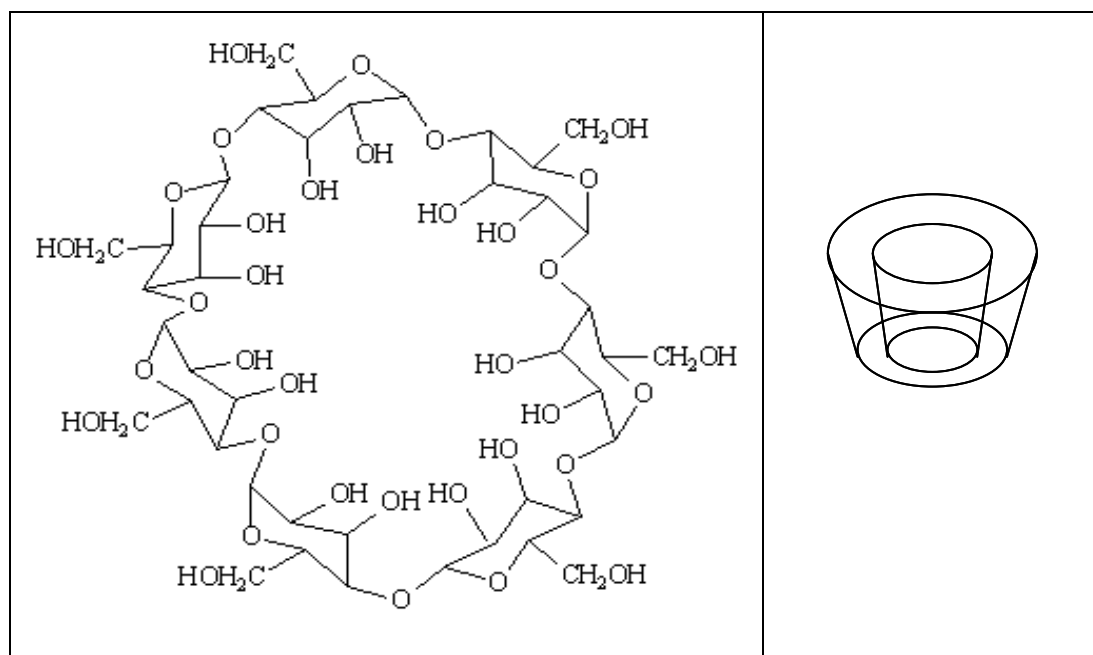
Fig. 6-4 β-cyclodextrin

It is believed that the driving force for the inclusion process is mainly hydrophobic-hydrophobic interaction. The molecules which can form an inclusion complex with cyclodextrin must fit into the cyclodextrin cavity. If the substrate is too small, it will pass in and out of the cavity with little apparent binding. Larger molecules simply cannot fit into the cavity. A simple approach to probe the inner cavity and the inclusion process is to use medium-sensitive fluorescence probes as guest molecules[162-164]. The fluorescence intensity enhancement along with the spectral blue shifts on inclusion in the cyclodextrin cavity appear to be a general feature with a wide variety of microenvironmental probes. Nozakura et al.[159] reported the fluorescence enhancement of 2-(p-Toluidino)-6-naphthalenesulfonic acid potassium salt (TNS) (figure 6-5) in aqueous solutions of β-CD or a β-CD-containing polymer.
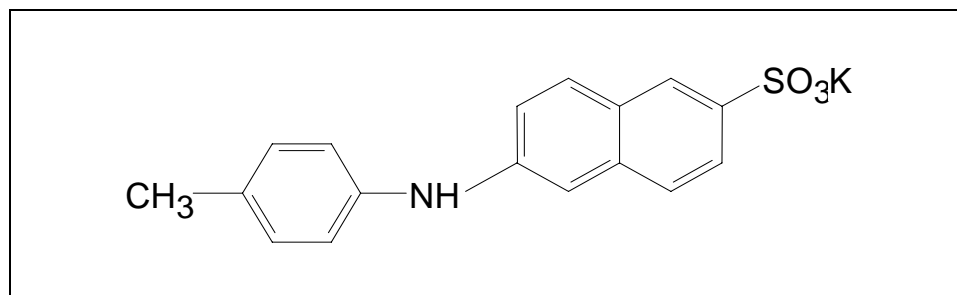
Fig. 6-5 2-(p-Toluidino)-6-naphthalenesulfonic acid potassium salt (TNS)

TNS alone in water showed negligible fluorescence. In the presence of β-CD, TNS showed enhanced fluorescence with a blue shift of the emission maximum (see figure 6-6). The fluorescence enhancement of TNS was generally thought to be caused by an increased viscosity and decreased polarity of the microenvironment in the β-CD cavity, which in turn leads to an increase in the radiative rates, a decrease in the probe rotational freedom, and the elimination of water molecules surrounding the probe molecule in aqueous solution. The effect of solvent on quantum yield has been interpreted in terms of conformation and rigidity of fluorophore, solvent relaxation, and existence of two excited singlet species. Intramolecular rotation of the fluorophore should promote radiationless transition to the ground state. Solvent relaxation should decrease the singlet-triplet gap, facilitating the intersystem crossing and thereby quenching the fluorescence[165]. The solute-solvent interactions can also affect the relative positions of the excited state with respect to the ground state, leading to red or blue shifts in the emission maximum. The blue shift of TNS in β-CD aqueous solution thus corresponds to the lower polarity of the microenvironment in the cyclodextrin cavity.
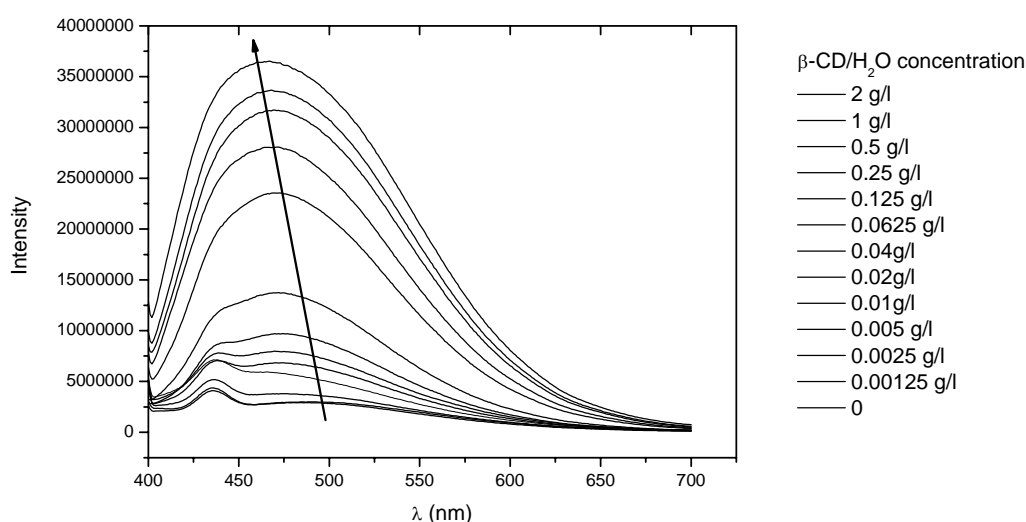
Fig. 6-6 Dependence of the fluorescence intensity of TNS on the concentration of β-Cyclodextrin in water. The arrow indicates the fluorescence peak of the cyclodextrin-TNS-complex increasing with increasing cyclodextrin concentration, the second peak at $\lambda = 430$ nm is, as described in the literature [166, 167], the RAMAN scattering peak of water.

Due to the special photophysical properties of the β-CD and TNS inclusion complex and the fluorescence intensity change shown in figure 6-6, TNS can be used to quantify the β-CD content in aqueous solution. It has to be mentioned that the emission maximum of TNS in aqueous solution is at around 500 nm, the emission peak at around 430 nm in figure 6-6 is the Raman scattering peak of water. The photophysical properties of β-CD, combined with its sufficient UV resistance and relatively high molecular weight (~1000 g/mol), make β-CD very promising as a guest molecule for probing the drug release behaviour of our microcapsules.

6.3 Results and discussion

The w/o/w emulsfication for preparing microcapsules was based on the procedure described in the last chapter but the ingredients were slightly changed due to the encapsulation of guest molecules (see table 6-1).

Table 6-1 Ingredients of emulsion used for encapsulation and release test

Emulsion type	Ingredient	Weight (g)
W/O emulsion	H_2O	0.94
	β-Cyclodextrin	0.06
	cin04	0.1
	Span85/Toluene (12wt%)	0.9
W/O/W emulsion	W/O emulsion	0.2
	H_2O	1.794
	SDS	0.006

The microcapsule solution (10 ml) prepared from the w/o/w emulsion template was placed in a dialysis tube, and dialyzed against pure water (40 ml) (details see experimental part 8.2.8). Since the dialysis membrane only let through molecules with $M_w < 5000$ g/mol, only β-cyclodextrin and small surfactant molecules can penetrate

the dialysis membrane into the dialysis medium. Microcapsules and nanoparticles will be kept inside the dialysis tube. (Figure 6-7)
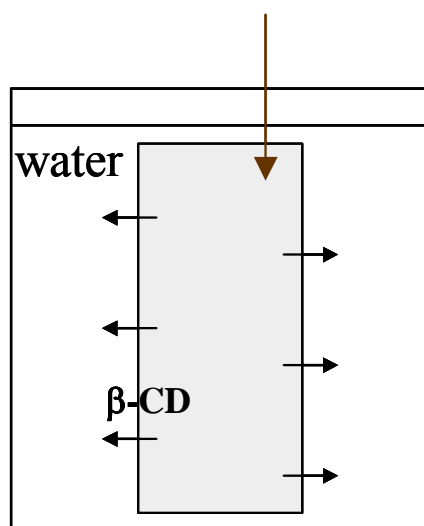
Fig. 6-7 Scheme for dialysis

β-Cyclodextrin molecules which are entrapped within microcapsules were distinguished from released molecules as follows: dispersions of microcapsules (from 10 wt% nanoparticle solution) containing a known amount of β-cyclodextrin were dialyzed (membrane pore size 5 nm) both before and after photocleavage versus an outer phase of pure MilliQ water. The amount of β-cyclodextrin which passed the dialysis membrane was quantified using a standard solution of the fluorescent dye 2-(p-Toluidino)-6-naphthalenesulfonic acid potassium salt (TNS) which due to complexation with β-cyclodextrin shows strong enhancement of its fluorescence emission [168]. For calibration, an aqueous solution containing only β-cyclodextrin was also dialyzed. Resulting fluorescence emission spectra are shown in figure 6-8.

The fluorescence spectra of pure TNS-solution and of dialysis medium from the dialyzed microcapsules before photocleavage are almost identical, showing that > 90 % of the β-cyclodextrin molecules were encapsulated. According to the fluorescence intensity resulting from microcapsule dispersions after photocleavage in

comparison to that resulting from pure β-cyclodextrin solution, ~ 50 % of the β-cyclodextrin molecules were released after photocleavage. There could be several reasons why the release is incomplete: for thick-shell microcapsules used here (shell thickness 40 layers of crosslinked nanoparticles) some capsules may still remain intact. Also, some β-cyclodextrin molecules may simply absorb onto large microcapsule shell fragments. In addition, photocleavage of the microcapsules leads to precipitation of the shell fragments and β-cyclodextrin molecules might also get entrapped within the insoluble precipitate.
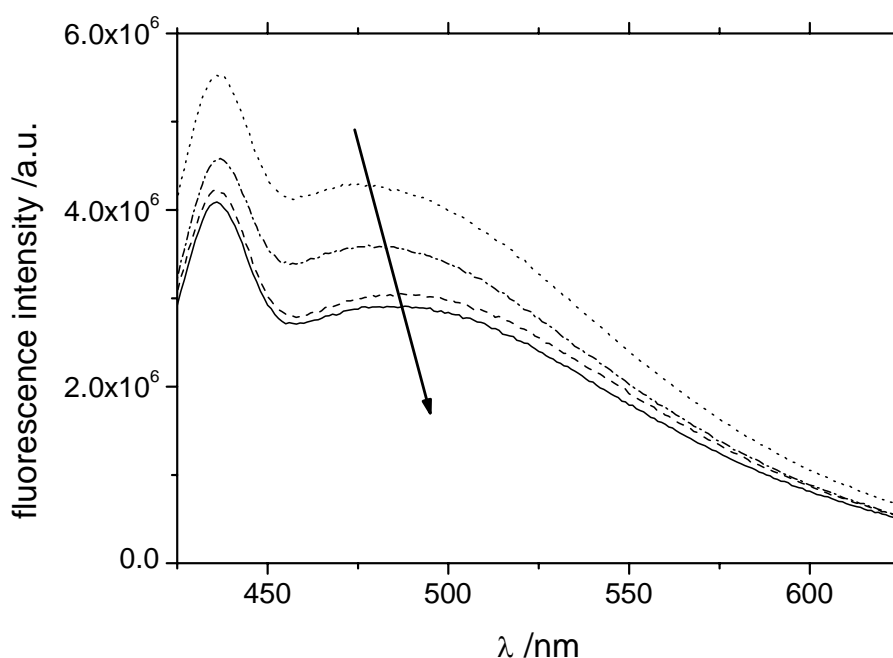
Fig. 6-8: Fluorescence emission spectra of pure TNS-solution (solid line), TNS-solution plus the dialysis medium from dialyzed cyclodextrin solution (dotted line), and TNS-solution plus dialysis medium from dialyzed solution of microcapsules containing cyclodextrin before (dashed line) and after (dash-dotted line) photocleavage. The arrow indicates the fluorescence peak of the cyclodextrin-TNS-complex decreasing with decreasing cyclodextrin concentration, the second peak at λ = 430 nm is, as described in the literature [166, 167], the RAMAN scattering peak of water.

In conclusion, the new controlled release system described here shows several advantages including: high encapsulation efficacy (~90%); they can be destroyed in a controlled way, and release of the entrapped guest molecules is efficient (> 50 %) even though the system has not yet been optimized (see chapter 5). Though very strong UV light necessary for photocleavage limits the application of this system, it opens up a pathway to controlled release of the enclosed components based on reversible photochemistry.

7 SUMMARY & OUTLOOK

7.1 Summary

In this thesis, we have presented the preparation of highly crosslinked spherical photoreactive colloidal particles of radius about 10 nm based on the monomer trimethoxysilane. These particles are labeled chemically with two different dye systems (coumarin, cinnamate) which are known to show reversible photodimerization. By analyzing the change in particle size upon UV irradiation with dynamic light scattering, we could demonstrate that the partially reversible photoreaction in principle can be utilized to control increase and decrease of colloidal clusters. Here, selection of the appropriate wavelengths during the irradiation employing suitable optical filters proved to be very important. So far, we have not been able to grow very large clusters again once they have been destroyed by UV radiation. We believe at present that UV light of very short wave lengths emitted from our lamp irreversibly destroys the photo labels if irradiating them for several hours. Therefore, we did the irradiation in an even more controlled way, using a toluene bath for photo-crosslinking and a dichroic mirror for photo-cleavage, we observed a second increase of particle size. This results means the experimental conditions were improved and under even more optimized irradiation conditions, an even higher degree of reversible cluster formation should become possible.

Next, we showed how photocrosslinking of our nanoparticles within the micrometer-sized thin oil shell of water-oil-water emulsion droplets leads to a new species of optically addressable microcontainers. The inner water droplet of these emulsions may contain drugs, dyes or other water-soluble components, leading to filled containers. Thickness, mechanical stability and light resistance of the container walls can be controlled in a simple way by the amount and adjustable photoreactivity (= No. of labels/particle) of the nanoparticles. Importantly, the chemical bonds between the nanoparticles constituting the microcapsule shell can be cleaved photochemically by irradiation with UV light. An additional major advantage is that filling our microcapsules with water-soluble substrate molecules is extremely simple using a solution of the guest molecules as inner water phase of the W/O/W-emulsion. This optically controlled destruction of our microcontainers thus opens up a pathway

to controlled release of the enclosed components as illustrated by the example of enclosed cyclodextrin molecules.

7.2 Outlook

We showed that our photoreactive nanoparticles indeed are capable of photo-reversible cluster formation. However, the particle-cluster transition couldn't be infinitely repeated. An ideal reversible cluster formation process would be highly desirable for both fundamental studies and for potential applications. Therefore, to find out the optimum experimental conditions to realize a 'real' or at least more reversible cluster formation is an interesting future challenge.

We are not only interested in understanding the general mechanism of cluster formation in more detail by employing an experimental system which allows us to control the aggregation rate and the reversibility. We also want to explore the suitability of our new system as an opto-chemical switch, i.e. upon irradiation with UV-light the properties of a colloidal dispersion (e.g. optical transparence, electric conductivity, viscosity etc.) can be adjusted in a well-defined way. For this purpose, we first have to explore the change in dispersion properties with cluster size. By measuring the viscosity of a single particle solution and a cluster solution (average cluster size > 500 nm, obtained after irradiating a 10 g/l cin04/toluene solution for 2 hours), we found that the viscosity of the cluster solution has increased by around 1000 times. This result is shown in figure 7-1.
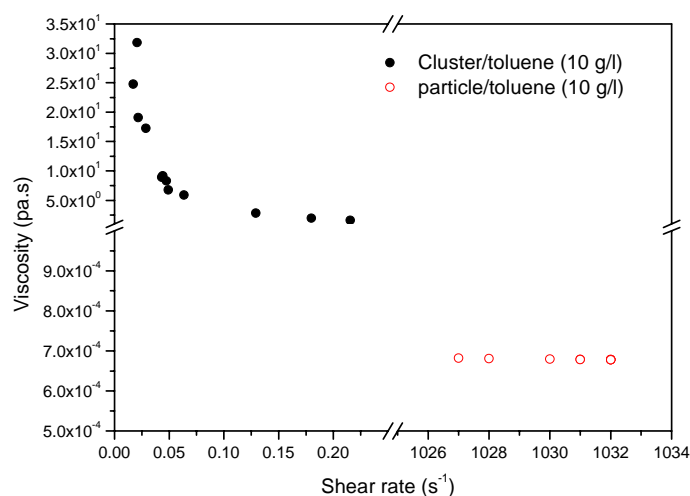
Fig. 7-1 Viscosity versus shear rate for particle (sphere) and cluster solution (sphere)

This huge increase in viscosity by far exceeds our expectation and therefore is very interesting. A more systematic study of the viscosity of these clusters in solutions might help us to understand this special rheological behaviour and to further explore the possibility of a potential application of our photoinduced cluster formation as an "optical switch".

The photocrosslinking of the above photoreactive nanoparticles within water-oil-water emulsion droplets leads to photo-cleavable microcontainers. This undoubtedly an interesting result because of its potential application as a controlled release system. However, the emulsion droplets we obtained showed a large polydispersity in size, which will in turn lead to polydispersity of the size and shell thickness of microcapsules, thus limiting the potential application of these microcapsules. We therefore need to optimize the condition of w/o/w emulsification and reduce the size polydispersity. First tests have shown that, using a pressure-homogenizer (Avestin C5), not only W/O/W-microdroplets with reduced polydispersity, but also much smaller microcapsules in diameter can be prepared.

a   **b**
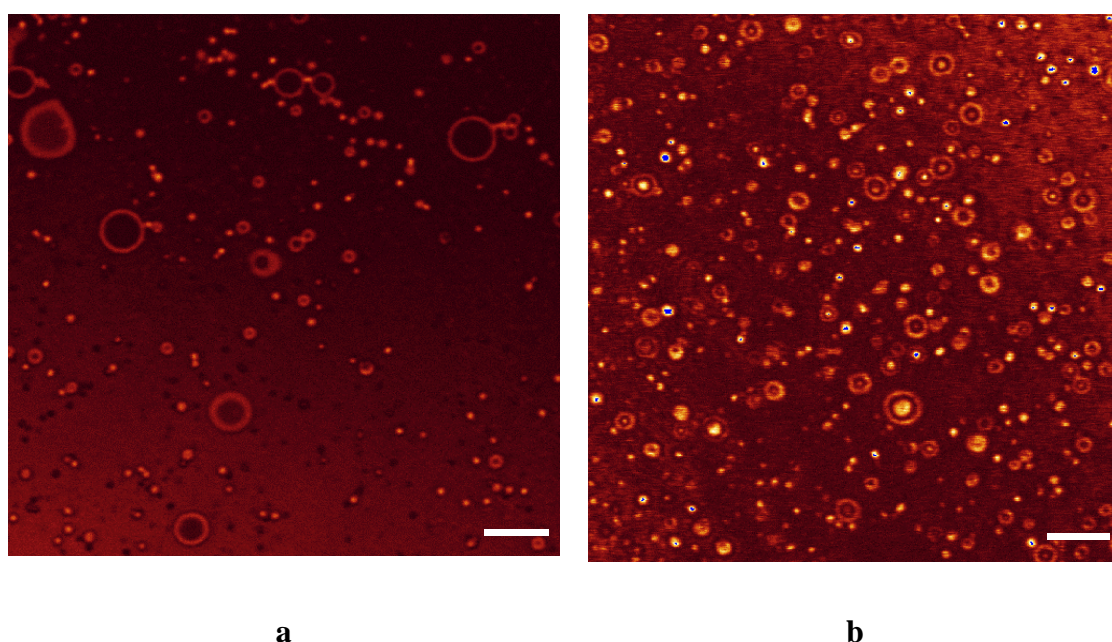
Fig. 5-8 Optical fluorescence micrographs for a typical w/o/w emulsion prepared using the standard procedure (a) and the Avestin C5 homogenizer (b) (scale bar 10 μm). The toluene shell of the microdroplets has been contrasted by fluorescent CdSe-Nanoparticles.

Finally, the controlled release behaviour of our new microcapsules should in principle be influenced by several factors, for example, the optical stability of the microcapsule, structure and size of the guest molecules, and so on. It will be interesting in the future to study the release behaviour by varying the dye content of the nanoparticles, shell thickness of microcapsules, and types of guest molecules in a systematic way.

8 EXPERIMENTAL

8.1 Materials

The silane compounds methyltrimethoxysilane(M1), trimethylmethoxysilane (M3) and hexamathyldisilazane (HMN), provided by Wacker Chemie/Burghausen, and (chlorobenzyl)trimethoxysilane (C1-M1) (ABCR, 97%) were used as supplied without further purification. The other chemicals, benzethonium chloride (Aldrich, 97%), NaOH (Aldrich, 97%), 18-crown-6 (Aldrich, 99%), cesium iodide (Fluka, 99.5+%), cesium carbonate (Aldrich, 99%), p-nitro cinnamic acid (Acros, 97%), 7-hydroxycoumarin (Acros, 99%), ethyl bromoacetate (Aldrich, 98%), K_2CO_3 anhydrous (Fluka, 99%), hydrochloric acid (Acros, 37%), Sodium dodecyl sulfate (SDS) (Fluka, 99.0% (GC)), Span85 (Fluka), Fluorescein Sodium (Fluka) Amylose from potatoes (Aldrich), Iodine solution, (Fishcer, 1% w/v in potassium iodide), 8-Quinolinol (Sigma, crystalline), Zinc chloride (Acros, 99.99%), β-Cyclodextrin (Sigma, 98%), 2-(p-Toluidino)-6-naphthalenesulfonic acid potassium salt (TNS) (Sigma) were also used as received.

The cesium salt of coumarin343 was synthesized and characterized by C. Graf. Oil-soluble and water-soluble CdSe nanocrystals were kindly provided by Mr. Xie from the Institute of Physical Chemistry of Mainz University.

The acetone used for synthesizing ethyl(7-coumaryloxy)acetate was distilled from potassium carbonate (anhydrous).

The water used for synthesis of polyorganosiloxane-μ-gels, preparation of w/o/w emulsion, as well as the dialysis process was deionized using a Milli-RO-purification system (Millipore).

The solvents THF, Toluene and Cyclohexane used for UV-Vis measurements were spectroscopy grade (Merck, UVASOL®).

All other solvents were used as supplied.

8.2 Synthesis

8.2.1 Chlorobenzyl-Functionalized Poly(organosiloxane) Nanoparticles

The chlorobenzyl-functionalized poly(organosiloxane) particles Cl-B1 were synthesized following the procedure described by Graf et al.[36, 37]. All reactions were carried out at room temperature. At first, a mixture of 21.8g methyltrimethoxysilane (M1) and 3.2g (chlorobenzyl)trimethoxysilane (Cl-M1) was added slowly (during 60 min) using a RAZEL syringe pump (Bioblock scientific) to a stirred (400rpm) solution of 2.5g (5.6mmol) of benzethonuim chloride in 125 mL of 6×10^{-3}M NaOH (in Milli-Q water). Then, the reaction mixture was stirred for 6 hours. Next, the functionalized particles were coated with a hydrophobic surface by a 2-step "endcapping reaction"[57, 58]: 5g trimethylmethoxysilane (M3) was added to 25 g aqueous dispersion (which has been filtered once before endcapping to remove microscopic clusters) and stirred overnight, then the same amount of M3 was added again and the mixture stirred for another 6 h. Finally, the dispersion was destabilized by addition of 100 mL methanol. The destabilized dispersion was centrifuged and the precipitate was washed 3 times with 50 ml of methanol to remove the residual surfactant. After that, the precipitate was redissolved in 50mL toluene and the remaining methanol was removed by rotatary evaporation. 5g hexamathyldisilazane (HMN) were then added to the toluene solution which was stirred overnight. After this 2-step endcapping procedure, the resulting nanoscopic spherical particles with hydrophobic surfaces were precipitated in 200mL of methanol and centrifuged. The precipitate was washed twice with methanol and filtered, and the resulting product was dried in vacuo for 12 h. A white powder was obtained.

The chlorobenzyl-functionalized poly(organosiloxane) particles Cl-B2 were synthesized following the modified procedure sketched in figure 3-3. At first, 24g M1 were added slowly (during 60 min) using a RAZEL syringe pump (Bioblock scientific) to a stirred (400rpm) solution of 2.5g (5.6mmol) of benzethonuim chloride in 125 mL of 6×10^{-3}M NaOH (in Milli-Q water). After the addition, the reaction mixture was stirred for 2 h, followed by slow addition (30 min) of a mixture of 0.5g M1 and 0.5g Cl-M1. Then, the reaction mixture was stirred for 6 hours. After this, the functionalized particles were endcapped by following the same procedure as described above.

For clarification, the chemicals used for the synthesis of polyorganosiloxane nanoparticles are listed in table 8-1. The dosage of NaOH, benzethonuim chloride, monomers, M3, toluene and HMN is valid for 25g aqueous dispersion.

Table 8-1 Synthesis of Chlorobenzyl functionalized polyorganosiloxane-μ-gels

Component \ Sample No.		Cl-B1	Cl-B2
NaOH (mol/L)		6×10^{-3}	6×10^{-3}
benzethonuim chloride (g)		0.5	0.5
Core Monomer	M1 (g)	4.36	4.8
	C1-M1 (g)	0.64	
Shell Monomer	M1 (g)		0.1
	C1-M1 (g)		0.1
Endcapping Reagent	M3 (g)	10	10
	Toluene (mL)	50	50
	HMN (g)	5	5

8.2.2 Labeling reaction

The dye labels (Coumarin 343, Coumarin, Cinnamate, see figure 3-8) were chemically attached to the chlorobenzyl-functionalized particles by a S_N2 reaction of the cesium salt of the chromophores with the chlorobenzyl groups. This coupling reaction is carried out under argon and exclusion of light. 2 ml of 18-crown-6 were dissolved in 100mL of THF. 2g of chlorobenzyl-functionalized poly(organosiloxane) particles, stoichiometric cesium salt of the chromophore (see table 8-2) and cesium iodide were added. The mixture was stirred under reflux at T=55°C for 48 hours.

After the coupling reaction, the labeled poly(organosiloxane) particles were precipitated in methanol. Nonreacted dye was removed by washing the precipitate several times with methanol. Finally, the labeled particles were dried in vacuo at room temperature for 12h. Yellow (coumarin 343), light yellow (cinnamate) and white (coumarin) solids were obtained. The whole procedure for preparation of dye-labeled poly(organosiloxane) nanoparticles is summarized in figure 3-4 or figure 3-5 based on different Chlorobenzyl polyorganosiloxane-μ-gels Cl-B1 and Cl-B2, respectively.

Table 8-2 gives the details for the different dyes used for labelling 2g polyorganosiloxane-μ-gels to obtain the dye-labeled nanoparticles described in this thesis. It is very important to note that all steps of the dye-labelling reaction had to be conducted under exclusion of light.

Table 8-2 Synthesis of dye-labeled polyorganosiloxane-μ-gels

Sample No	Polyorganosiloxane-μ-gel (1 g)	Dye	Dosage for labelling (mmol)
Cou343p	Cl-B2	Coumarin343	0.33
Cou0303	Cl-B2	Coumarin	0.33
Cin01	Cl-B1	Cinnamate	1.8
Cin02	Cl-B1	Cinnamate	1.4
Cin03	Cl-B1	Cinnamate	0.48
Cin04	Cl-B2	Cinnamate	0.33

8.2.2.1 Cesium salt of p-nitro cinnamate[36]

To prepare the Cesium salt of p-nitro cinnamate, 20 mmol p-nitro cinnamic acid and 10 mmol Cesium carbonate were dissolved in 400 mL DMF. The reaction mixture was stirred for 48 h at room temperature and then filtered. The solvent was removed under reduced pressure at 50 °C and the product was dried in vacuo for 24h.

A brown solid was obtained. The reactions had to be conducted under exclusion of light.
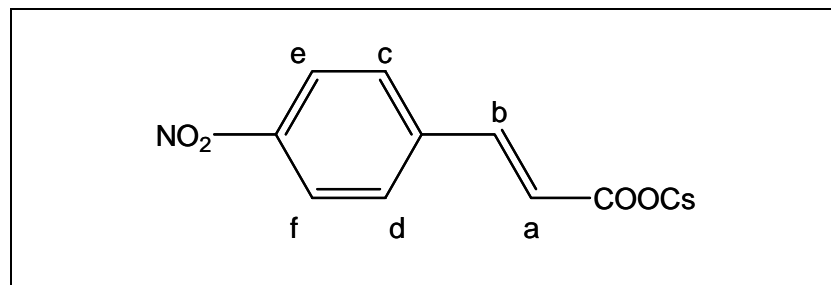
Fig. 8-1a Cesium salt of p-nitro cinnamate, a, b, c, d, e, f indicate the position of H.

Fig. 8-1b 300 MHz ^{1}H NMR spectrum of p-nitro cinnamate cesium salt in DMSO-d_6.

8.2.2.2 Cesium salt of (7-coumaryloxy)acetate[36, 81]

(1) To a solution of 9.826g (60.6 mmol) of 7-hydroxycoumain and 7.2 mL (64.6 mmol) of ethyl bromoacetate in 270 mL of freshly distilled acetone, 8.75g of potassium carbonate (anhydrous) were added, and the reaction mixture was boiled

under reflux for 2 h. After removal of the salt by filtration, the solvent was removed under reduced pressure and the product was dried in vacuo. The pale yellow solid (ethyl(7-coumaryloxy)acetate) obtained was recrystallized from ethanol.
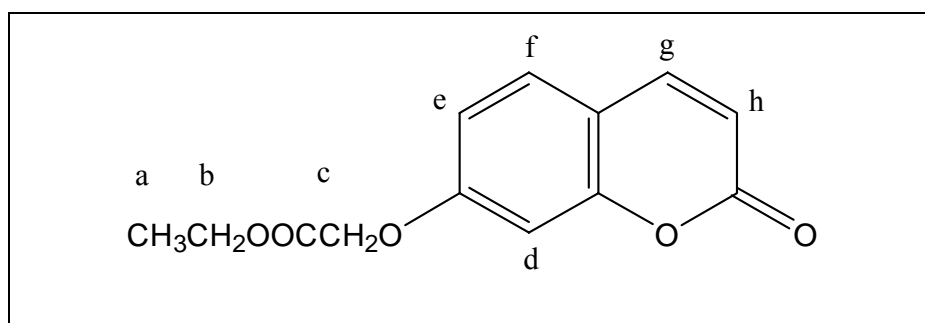
Fig. 8-2a ethyl(7-coumaryloxy) acetate, a, b, c, d, e, f, g, h indicate the position of H.
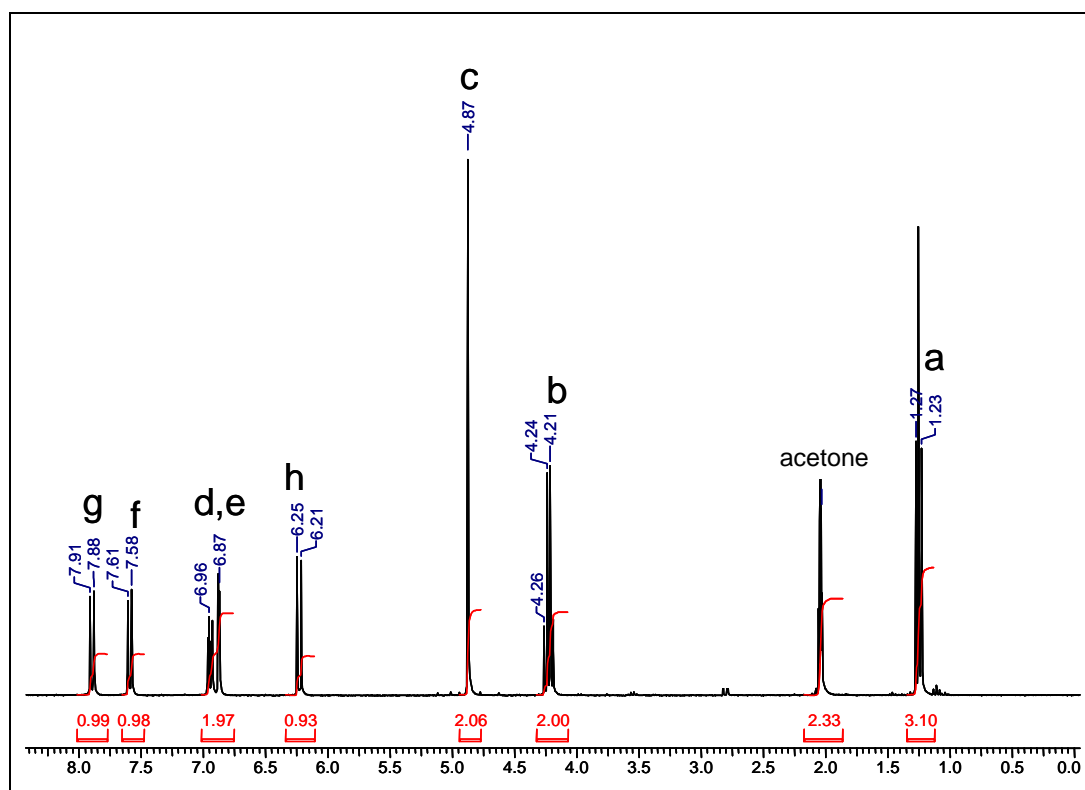
Fig. 8-2b 300 MHz ^{1}H NMR spectrum of ethyl(7-coumaryloxy) acetate in acetone-d$_6$.

(2) To cleave the ester, a mixture of 2.16 g of ethyl(7-coumaryloxy)acetate and 5 g of sodium hydroxide was dissolved in 200 mL of water/dioxane (1:1). After the solution was stirred overnight, the solvent was removed under reduced pressure. The yellow residue was dissolved in 20 mL of distilled water and acidified with

concentrated hydrochloric acid under ice cooling. The white precipitate was collected by filtration, washed thoroughly with cooled water, and dried in vacuo to obtain (7-coumaryloxy) acetic acid.
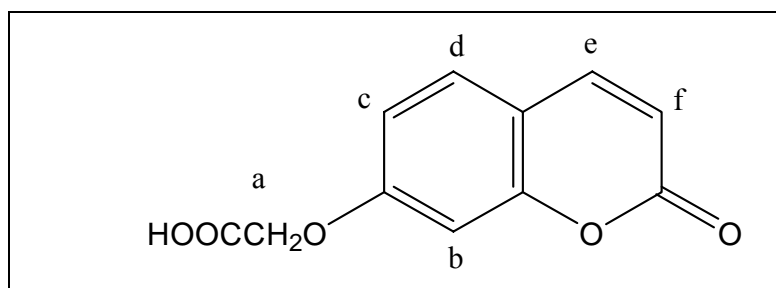
Fig. 8-3a (7-coumaryloxy) acetic acid, a, b, c, d, e, f indicate the position of H.
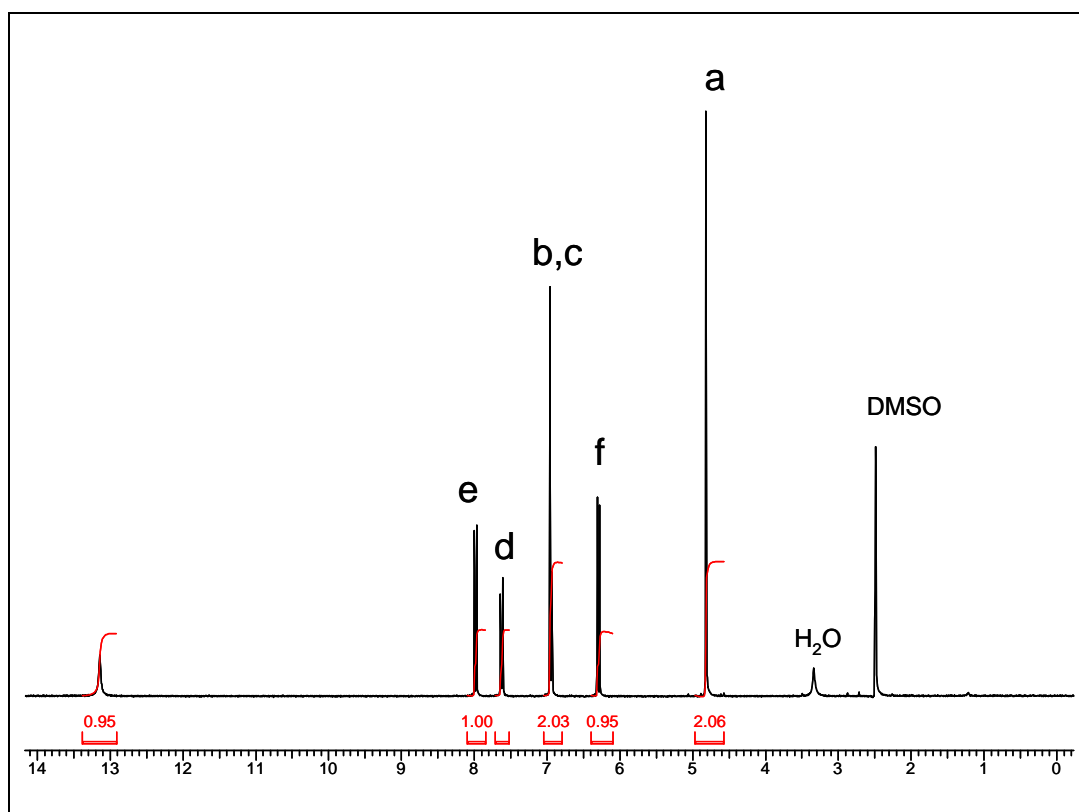
Fig. 8-3b 300 MHz ^{1}H NMR spectrum of (7-coumaryloxy) acetic acid in DMSO-d$_6$.

(3) 1.685 g (7.02 mmol) (7-coumaryloxy) acetic acid and 1.144 g (3.51 mmol) Cesium carbonate were dissolved in 400 mL DMF. The mixture was stirred for 48h at room temperature and then filtered. The solvent was removed under reduced pressure at 50°C and then the product was dried in a vacuum oven for 24h. A hoar solid was

obtained. Importantly, all reactions related to the dye labels had to be conducted under exclusion of light.

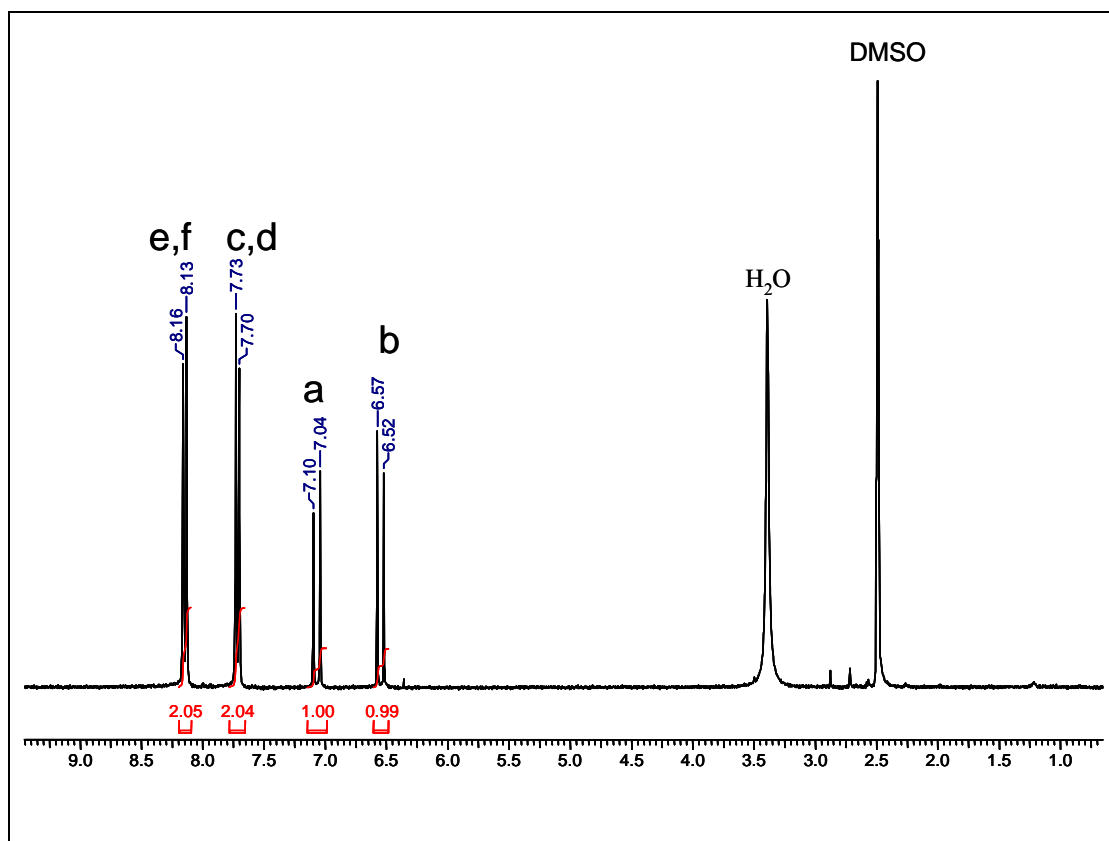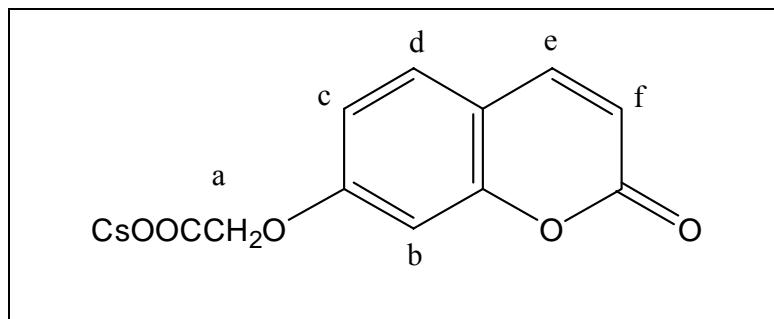**Fig. 8-4a** Cesium salt of (7-coumaryloxy) acetate, a, b, c, d, e, f indicate the position of H.
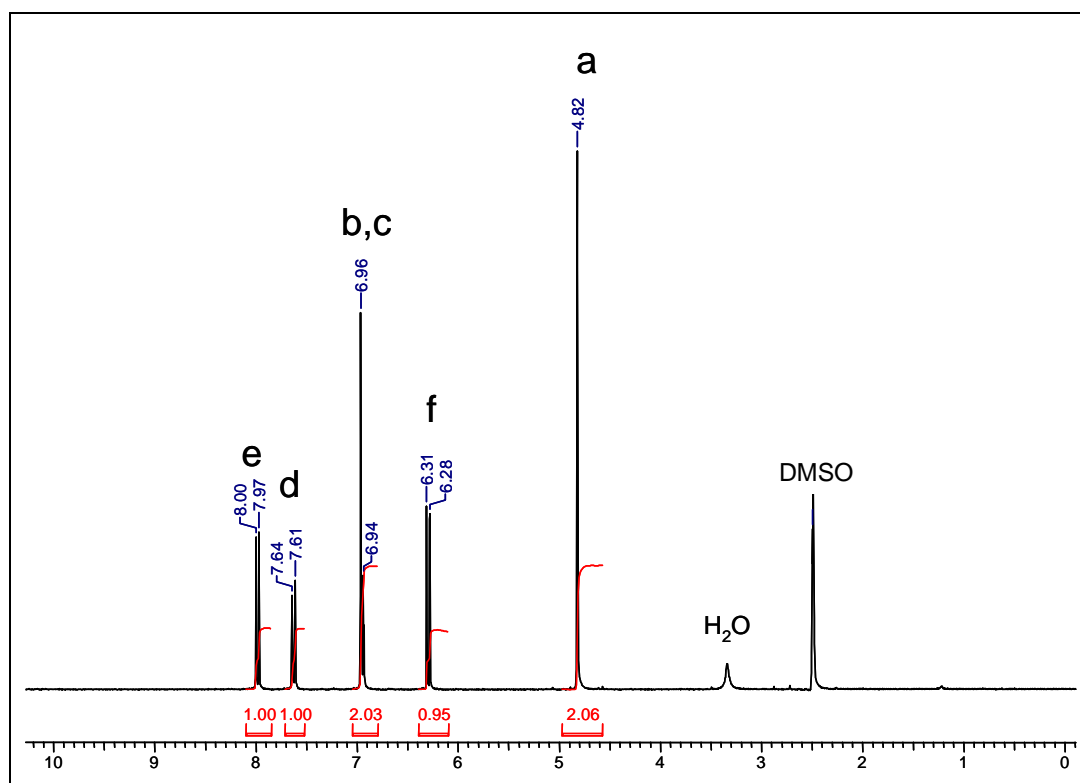
Figure 8-4b 300 MHz ^{1}H NMR spectrum of Cesium salt of (7-coumaryloxy) acetate in DMSO-d$_6$.

8.2.3 Photodimerization

Dye-labeled poly(organosiloxane) particles were dissolved in THF at a typical concentration of 10 g/l. The solutions were filtered into cylindrical suprasil light-scattering cuvettes (Hellma) of diameter 1 cm, using 0.2 μm Millipore dimex-13

filters. There is no obvious difference in sample concentration before and after filtration as deduced from the respective UV spectra. These samples were irradiated with a 200 Watts Hg-Xe lamp (USHIO UXM-200H) upto several hours, employing several different optical filters (Schott) to cut off uv-light of wavelengths below 275nm, 325nm and 365nm, respectively. (Figure 4-21) The spectral density distribution of the radiation output of our lamp has been shown in figure 4-21. Here, the reader should recall the discontinuous radiation spectrum of our light source, which, using appropriate high-pass filters, nevertheless yielded satisfying results concerning the efficience of the photodimerization process. The progress of the photodimeriazation, i.e. the increase of the average hydrodynamic radius (R_h) of the particle clusters with irradiation time, was monitored by dynamic light scattering.

For optimized photo-dimerization, the sample solution was placed in a 1 cm cylindrical quartz cuvette (Suprasil glass, Hellma), which itself was placed within a 2 cm quartz cuvette (Suprasil glass, Hellma) filled with toluene used as an optical filter. This setup was placed on a rotating plate to assure homogeneous irradiation of the whole sample, and irradiated with a 200 W Hg-Xe lamp (USHIO UXM-200H). This set up is schematically shown in figure 4-23a, the rotating speed of the rotating plate is about 2 rpm.

8.2.4 Photocleavage Reaction

Solutions with clusters formed by photodimerizaton were irradiated again with the 150 Watts Hg-Xe lamp, this time without any optical filters (therefore, also UV-light of very short wavelengths was illuminating the sample). The resulting change of the hydrodynamic radius of the clusters was again monitored by dynamic light scattering.

The photocleavage by using a dichroic mirror avoided the very short (< 250 nm) and harmful UV light, so it is an optimized method to photocleave the clusters. To correctly use the dichroic mirror, the angle between the incident light and dichroic mirror should be 45º (Figure 8-5), and the reflected light perpendicular to the incident light is the UV light (254±10 nm) we used to photocleave our sample. To produce a homogenous irradiation, the samples were placed on the rotating plate.
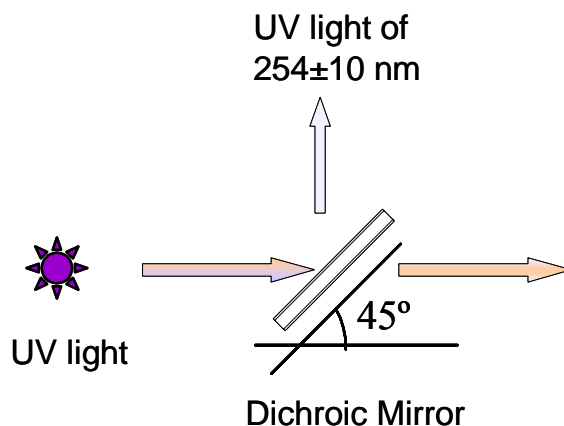
Fig. 8-5 Scheme of the dichroic mirror setup for less harmful photocleavage

The photodimerization leading to the formation of particle clusters and the photo cleavage leading to a break-up of these clusters were sketched schematically in figure 4-9.

8.2.5 Preparation of the water/oil/water-emulsion

The W/O/W emulsion was prepared following the prescription described by Matsumoto [169]: first, a W/O emulsion was produced by dropping 1 g MilliQ water into 1 g toluene (Aldrich) solution containing the surfactant Span85 (Aldrich) (12 wt%) and 10 wt% (or 5 wt%) of our cinnamate-labeled nanoparticles, and about 10^{-8} mol/l of self-made hydrophobic fluorescent CdSe nanoparticles (Mr. R. Xie). This water/oil mixture was homogenized with an Ultra-Turrax T10 (IKA Works, Inc.) at 1.0×10^4 rpm for 10 min at room temperature to produce a milky and viscous homogeneous emulsion. Next, 0.2 g of this W/O emulsion was added to 1.8 g of water containing 0.33 wt% of the surfactant sodiumdodecylsulfate (SDS) (Aldrich). The resulting solution was stirred at 500 rpm for 30 min at room temperature. The ingredients for emulsions with different composition were shown in the respective chapters of the thesis. The homogeneous W/O/W emulsion was then immediately irradiated with UV light to fix the shell of the microcapsules.

8.2.6 Fixing the microcapsules by photodimerization of the photoreactive nanoparticles

The W/O/W emulsion was placed in a 1 cm cylindrical quartz cuvette (Suprasil glass, Hellma), which itself was placed within a 2 cm quartz cuvette

(Suprasil glass, Hellma) filled with toluene used as an optical filter. This setup was placed on a rotating plate to assure homogeneous irradiation of the whole sample, and irradiated with a 200 W Hg-Xe lamp (USHIO UXM-200H) for 2 hours.

8.2.7 Destroying the microcapsules by photocleavage

After the photodimerization, the outer toluene cuvette was removed, and the 1 cm sample cuvette was irradiated with the 200 Watts Hg-Xe lamp using a dichroic mirror as an optical filter (wavelength of transmitted light 254 +/- 10 nm). Since free of dust is not so essential for emulsion as for light scattering measurement, here a magnetic stirrer were used to stir the sample under irradiation for higher efficacy of the photocleavage.

8.2.8 Preparation of cyclodextrin-filled microcapsules and quantification of release after photocleavage

1 g aqueous solution of cyclodextrin (c = 6 g/l) was used for preparation of the W/O-emulsion. To determine the release properties of the microcapsules, 3 different samples have been dialyzed (dialysis membrane: celluloseacetate, exclusion molar mass M = 5.000 g/mol) versus an outer phase of 40 ml of pure MilliQ water: 1.) 10 ml of a pure cyclodextrin solution (c = 0.03 g/l), 2.) 10 ml of the microcapsule dispersion (diluted from 1 ml original W/O/W dispersion) before photocleavage and 3.) 10 ml of the microcapsule dispersion after photocleavage (irradiation with UV-light = 254 nm for 20 hours). The amount of cyclodextrin which passed the dialysis membrane has been determined via the enhancement of the fluorescence emission of the fluorescent dye 2-(p-Toluidino)-6-naphthalenesulfonic acid potassium salt (TNS) due to formation of a cyclodextrin-TNS-complex.

8.3 Characterization

In this thesis, UV-Vis Spectroscopy, dynamic and static light scattering, Confocal Fluorescence Microscopy, NMR, GPC, FFF, AFM, TEM, SEM, Fluorescence Sepctroscopy and Rheology were employed to characterize the size and structure of the single particles, the clusters formed by photodimerization and the microcapsules built from photereactive nanoparticles.

8.3.1 Dynamic and Static Light Scattering

Average hydrodynamic radii (R_h) of the dye-labeled polyorganosiloxane nanoparticles and the clusters formed have been determined by dynamic light scattering (DLS) using an experimental setup consisting of a He-Ne laser (JDS Uniphase 1145p-3083, JDS Uniphase, 632.8 nm, 25 mW output power), goniometer SP-86(ALV), and an ALV-3000 digital correlator/structurator. The same instrument was used to determine the radius of gyration R_g and the mass-averaged particle molar mass Mw by static light scattering (SLS). All light scattering measurements have been carried out with filtered samples (Millipore dimex-13 filter, pore size 0.2μm). The refractive index increment necessary for the SLS experiments was measured with a home-built interferometer using a laser diode (613nm wavelength).

All measurements were carried out at 20 ºC.

8.3.2 Gel Permeation Chromatography (GPC)

The size distribution of the nanoparticles was measured by GPC at 20 ºC. Measurements were carried out with a 515-HPLC pump (Waters) equipped with three columns of different porosities (PSS Mainz ; 10^5, 10^4, 10^3 Å), using a Waters 2410-Differential refractometer or a Waters 486-UV-Vis dectector with variable wavelength for detection. For the dye-labeled polyorganosiloxane-μ-gels, the UV detection wavelength was the same as the respective UV absorption maxium of the photo labels (Coumarin 343 : 429 nm, Coumarin: 318 nm, Cinnamate: 302 nm). All samples were measured in toluene, using polystyrene standards from PSS (Molecular weight from 18100 to 2470000 g/mol) for calibration.

8.3.3 Field-Flow-Fractionation (FFF)

FFF measurements in this thesis were obtained using an Asymmetric Flow Field Flow Fractionation (AF-FFF) system from Consenxus, Ober-Hilbersheim, Germany, equipped with an AF-FFF channel with glass cover plate, a 190 μm Mylar spacer, a Thermoseparation TSP constametric 3200 flow pump running at 3 mL/min, a Knauer K501 injection pump operating at 0.1 mL/min, a Bronkhorst Hi-Tec Liqui-Flow delivering a cross-flow of 2 mL/min, a degasser Gastorr 152, valve box, and controller. An evaporative light scattering detector (PL-ELS 1000) was used and THF was used as eluent.

8.3.4 NMR Spectroscopy

The ^{1}H-NMR in solution was measured by Bruker AC 200, using Acetone-d$_6$ or DMSO-d$_6$ as solvent.

8.3.5 UV-Vis Absorption Spectroscopy

UV-Vis absorption spectroscopy measurements were conducted with a Varian Cary 100 Bio UV-Vis spectrometer at room temperature.

8.3.5.1 Determination of the chlorobenzyl content

The chlorobenzyl content of the poly(organosiloxane)-   -gels was determined via uv-absorption in cyclohexane, using a calibration curve obtained from standard solutions of the monomer C1-M1 for quantitative determination.

8.3.5.2 Determination of the coumarin343 label content

The dye content of the coumarin343 labeled poly(organosiloxane)-μ-gels was determined by comparison of the absorption of THF solutions of the particles with the absorption of a standard THF solution of the dye label precursor (benzyl ester of coumarin 343). This molecular dye has been confirmed to show identical absorption spectra as the coumarin-labeled particles. (see figure 3-10)

8.3.5.3 Determination of the coumarin label content

The dye content of the coumarin labeled poly(organosiloxane)-μ-gels was determined by comparison of the absorption of THF solutions of the particles with the absorption of a standard THF solution of the dye label precursor ethyl(7-coumaryloxy)acetate. This molecular dye has been confirmed to show the same absorption spectra as the coumarin-labeled particles. (see figure 3-12)

8.3.5.4 Investigation of dye-labeled polyorganosiloxane-μ-gels under irradiation

Cinnamate-labeled poly(organosiloxane) particles (cin04) were dissolved in THF at a concentration of 1 g/l. The sample solutions were placed in a 10mm×10mm suprasil UV cell. For photodimerization, these samples were irradiated with a 200 Watts Hg-Xe lamp upto several hours, employing optical filters BG 39 (Schott) to cut off UV-light of wavelengths below 325nm (figure 4-13b). For photocleavage, the

optical filter was removed and samples were irradiated directly by the Hg-Xe lamp. Various UV-Vis spectra of these samples were recorded in dependence of irradiation time.

The UV-Vis spectra of such a 2 g/l Cinnamate-labeled poly(organosiloxane) particles (cin04) solution in THF were also recorded under optimized irradiation conditions (Toluene bath and dichroic mirror).

8.3.6 Fluorescence Spectroscopy

The Fluorescence spectra of the complex of cyclodextrin and 2-(p-Toluidino)-6-naphthalenesulfonic acid potassium salt (TNS) were measured using a Hitachi F-4000 fluorescence spectrometer. The concentration of the fluorescence dye TNS was 1×10^{-5} mol/L in aqueous solution. The fluorescence dye was excited at 380 nm.

8.3.7 AFM

Atomic force microscopy (AFM) was used to characterize the size and shape of the single particles and the clusters. Samples were spin coated from highly diluted THF solutions of the poly(organosiloxane) particles (C=0.05g/l) onto freshly cleaved graphite. These surfaces were scanned with a nanoscope IIIa, Digital Instruments (Santa Barbara, CA), operating in tapping mode.

8.3.8 Confocal Fluorescence Microscopy

The fluorescence images of the water-in-oil-in-water emulsion were studied with a CLSM Leica TCS SP2 containing Leica miscroscope stand DM IRE2 and electronics box Leica CTR MIC (Leica Microsystems Heidelberg GmbH, Germany). Light sources used were a Ar/ArKr laser using λ_{ex} = 488 nm and a HeNe laser using λ_{ex} = 594 nm. The emission wavelength between 550-650 nm was collected by a photomultiplier tube. During acquisition, images were line-averaged to obtain the final computer-generated confocal images.

The water-in-oil-in-water emulsions were dropped directly onto microscope slides without dilution, and sandwiched between the microscope slide and a cover glass to prevent the solvent from evaporation. The oil phase of the w/o/w emulsion was contrasted using oil soluble fluorescent CdSe nanocrystals, and the inner water phase of the double emulsion was contrasted with water-soluble fluorescent CdSe

nanocrystals or fluorescein sodium. The concentration of the dye in all case was around 1×10^{-8} mol/L.

8.3.9 Transmission Electronic Microscopy (TEM)

A Philips EM-420 transmission electron microscope operating at an acceleration voltage of 120 kV was used to analyze the size and size distribution of the polyorganosiloxane-μ-gels. The nanoparticles were deposited from diluted solutions onto copper grids with carbon support, and observed after they had been dried in air overnight.

8.3.10 Scanning Electronic Microscopy (SEM)

The morphology and strucure of the polyorganosiloxane microcapsules was observed using a scanning electronic microscope (LEO 1530 Gemini, Max-Planck Institute for Polymer Research). The microcapsules or photocleaved microcapsules were cast from solution onto the surface of a purified silicon wafer. The cleaning of this silicon wafter followed a standard procedure:

1) Pre-clean the silicon wafer by using organic solvents like ethanol to remove the organic impurity ;

2) Prepare the cleanning solution in a teflon beaker. This cleaning solution consisted of 5 volumes Milli-Q water, 1 volume of concentrated ammonium solution (29% w/w NH_3, elctronic grade) and 1 volume of Hydroperoxide (30% w/w H_2O_2, electronic grade) ;

3) Stir the above solution and place the pre-cleaned silicon wafer into this cold solution ;

4) Heat the solution to 75 – 80 ˚C and let the solution stand at 80 ˚C for 10 mins. (Note : Never allow the solution temperature to get higher than 85 ˚C.)

5) Rinse the silicon wafer by using Milli-Q water for 5 mins after the above procedure. Always keep the wafter under water and never expose the silicon wafter to the air during rinsing. The cleaned silicon wafer should be used freshly.

8.3.11 Rheometer

The rheological behavior of the particle solution and the cluster solutions were measured with a stress controlled rheometer (AR 1000 (TA Instrument)) using a double gap geometry. The measurements were carried out at 20 ˚C. The concentration of the particle or cluster solution in toluene was 10 g/l. The cluster solution was formed by irradiating the cinnamate-labeled polyorganosiloxane-μ-gels (Cin04)/toluene solution for 3 hours using the 200w Hg-Xe lamp.

9 REFERENCES

[1] Evans, D. F., Wennerström, H, "The Colloidal Domain", Wiley-VCH, New York (1999)

[2] Eastoe, J., "Surfactant Chemistry", Dissertation, University of Bristol, (2003)

[3] Hunter, R. J., "Foundation of Colloid Science", I, Clarendon Press, oxford (1993)

[4] Graf, C., "Farbstoffmarkierte Polyorganosiloxan-μ-gele als neuartige Sondensysteme", Dissertation, Mainz University, Mainz (1999)

[5] Everett, D. H., "Basic Principle s of Colloid Science", The Royal Society of Chemistry, London (1988)

[6] Caruso, F., "Colloids and Colloid Assemblies", WILEY-VCH, weinheim (2003)

[7] Takeo, M., "Disperse System", WILEY-VCH, Weinheim (1999)

[8] Derjaguin, B. V., Landau, L., *Acta Physicochem. URSS*, **14**, 633 (1941)

[9] Derjaguin, B. V., Churaev, N. V., Muller, V. M., "Surface Forces", Consultants Bureau, New York (1987)

[10] Venvey, E. J. W., Overbeek, J. Th. G., "Theory of the Stability of Lyophobic Colloids", Elsevier, Amsterdam (1948)

[11] Napper, D. H., "Polymeric stabilization of Colloidal Dispersions", Academic Press, London (1983)

[12] Stradner, A., Sedgwick, H, Cardinaux, F., Poon, W. C. K., Egelhaaf, S. U., Schurtenberger, Peter, *Nature*, **432**, 492 (2004)

[13] Poon, W., *Science*, **304**, 830 (2004)

[14] Blaaderen, A. v., *Science*, **301**, 470 (2003)

[15] Yi, G.-R., Manoharan, V. N., Michel, E., Elsesser, M. T., Yang, Seung-Man, Pine, D. J., *Adv.Mater.*, **16**, 1204 (2004)

[16] Manoharan, V. N., Elsesser, M. T., Pine, David. J., *Science*, **301**, 483 (2003)

[17] Meakin, P., *Phys.Rev.A*, **27**, 1495 (1983)

[18] Starr, F. W., Douglas, J. F., Glotzer. S. C., *J. of Chem. Phys.*, **119**, 1777 (2003)

[19] Terao, T., Nakayama, T., *J.Phys.Cond.Mat.*, **11**, 7071 **(1999)**

[20] Terao, T., Nakayama, T., *Phys.Rev.E*, **58**, 3490 (**1998**)

[21] Kolb, M., *J. Phys. A: Math. Gen*, **19**, L263 (1986)

[22] Chen, D. H., Doi, M., *J.Coll.Int.Sci.*, **212**, 286 (1999)

[23] Xia, Y., Fudouzi, H., Lu, Y., Yin, Y., "Colloidal Crystals: Recent Developments and Niche Application" (p284), in "Colloids and Colloid Assemblies", ed., F. Caruso, WILEY-VCH, Weinheim (2003)

[24] Hammond, P. T., "Surface-directed Colloid Patterning: Selective Deposition vis Electrostatic and Secondary Interactions" (p317), in "Colloids and Colloid Assemblies", ed., F. Caruso, WILEY-VCH, Weinheim (2003)

[25] Cassagneau, T. P., "Layer-by-layer Self-assembly of Metal Nanoparticles on planar Substrates: Fabrication and Properties" (p398), in "Colloids and Colloid Assemblies", ed., F. Caruso, WILEY-VCH, Weinheim (2003)

[26] Sastry, M., "Nanoparticle Organization at the Air-water Interface and in Langmuir-Blodgett Films" (p369), in "Colloids and Colloid Assemblies", ed., F. Caruso, WILEY-VCH, Weinheim (2003)

[27] Li, F. B., X.; Linnros, J.; Wiley, J. B., *J. Am. Chem. Soc.*, **127**, (2005)

[28] Dinsmore, A. D., Hsu, M, F., Nikolaides, M. G., Marquez, M., Bausch, A. R., Weitz, D. A., *Science*, **298**, 1006 (2002)

[29] Caruso, F., Caruso, R. A., Möhwald, Helmuth, *Science*, **282**, 1111 (1998)

[30] Wilcox, D. L., Berg, Sr. M., Bernat, T., Kellerman, D., Cochran, J. K., "Hollow and Solid Spheres and Microspheres: Science and Technology Associated with Their Fabrication and Application; MRS Proceedings " in ed., 372, Materials Research Society, Pittsburgh,PA (1995)

[31] Caruso, F., *Chem. Eur. J.*, **6**, 413 (2000)

[32] Hoffmann, A. S., Afrassiabi, A., Dong, L. C., *J. Controlled Release*, **4**, 213 and 223 (1986)

[33] Chen, G., Hoffmann, A. S., *Nature*, **373**, 49 (1995)

[34] Radt, B., Smith, T. A., Caruso, F., *Adv. Mater.*, **16**, 2184 (2004)

[35] Yuk, S. H., Cho, S. H., Lee, H. B., *Pharm. Res.*, **9**, 955 (1992)

[36] Graf, C., Schärtl, W., Fischer, K., Hugenberg, N., Schmidt, M., *Langmuir*, **15**, 6170 (1999)

[37] Graf, C., Schaertl, W., Hugenberg, N., *Adv.Mater.*, **12**, 1353 (**2000**)

[38] Chu, B., "Laser Light Scattering", Sec. Eds., Oxford (1987)

[39] Schmidt, M., "*Simultanous static and dynamic light scattering: application to structure analysis*" in "*Dynamic Light Scattering: The Method and Some Applications*", ed., W.Brown, Oxford University Press, Oxford, UK (1993)

[40] Sears, e. a., "University Physics", Addison-Wesley, (1976)

[41] Minsky, M., *Scanning*, **10**, 128-138 (1988)

[42] Herman, B., "Fluorescence Microscopy," 2nd. edn., Springer-Verlag, New York (1998)

[43] Knoll, M., Ruska, E. Z., *Physik*, **78**, 318 (1932)

[44] Butt, H.-J., Graf, Karlheinz, Kappl, Michael, "Physics and Chemistry of Interfaces", WILEY-VCH, Berlin (2003)

[45] Binnig, G., Rohrer, H., Geber, C., *Appl. Phys. Lett.*, **40**, 178 (1982)

[46] Amelinckx, A., Dyck, D. van, Landuyt, J. van, "Electron Microscopy", Wiley-VCH, Weinheim (1997)

[47] Binnig, G., Quate, C. F., Geber, C., *Phys.Rev.Lett.*, **56**, 930 (1986)

[48] "An introduction to Fluorescence Spectroscopy", PerkinElmer Ltd., (2000)

[49] Lakowicz, J. R., "Principles of Fluorescence Spectroscopy", Plenum Press, New York (1983)

[50] Barth, H. G., Boyes, B. E., Jackson, C., *Anal. Chem.*, **68**, 445R (1996)

[51] Cantow, M. J. R., Porter, R. S., "Analytical Gel Permeation Chromatography", Wiley, New York (1968)

[52] Grubisic, Z., Rempp, P., Benoit, H., *J Polym Sci Part B: Polymer Letter*, **5**, 753 (1967)

[53] Giddings, J. C., *Sep. Sci.*, **1**, 123 (1966)

[54] Cölfen, H., Antonietti, M., *Advances in Polymer Sci.*, **150**, 67-187 (2000)

[55] Wahlund, K. G., Giddings, J. C., *Anal. Chem.*, **59**, 1332 (1987)

[56] Clarson, S. J., Semlyen, J. A., "Siloxane Polymers", PTR Prentice Hall, Englewood Cliffs (1993)

[57] Baumann, F., "Synthese und Charakterisierung von molekular redispergierbaren Polyorganosiloxan-μ-Gelen durch Polykondensation in μ-Emulsion", Dissertation, University Bayreuth, Bayreuth (1995)

[58] Baumann, F., Deubzer, B., Geck, M., Dauth, J., Sheiko, S., Schimidt, M., *Adv.Mater.*, **12**, 955 (1997)

[59] Funke, W., Okay, O., Müller, B. J., *Advances in Polymer Sci.*, **136**, 142-234 (1997)

[60] *IUPAC Macromolecular Division*, **Commission on Macromolecular Nomenclature**, (1995)

[61] Schumann, J. H., Stockennius, W., Prince, L. M., *J. Phys. Chem.*, **63**, 1677 (1959)

[62] Becker, A., Köhler, W., Müller, B., *Ber.Bunsenges.Phys.Chem.*, **99**, 660 (1995)

[63] Bremser, W., Antonietti, M., Schmidt, M., *Macromolecules*, **23**, 3796 (1990)

[64] Wu, C., *Macromolecules*, **27**, 298 (1994)

[65] Baumann, F., Schimidt, M., Deubzer, B., Geck, M., Dauth, J., *Macromolecules*, **27**, 6102 (1994)

[66] Stöber, W., Fink, A., Bohn, E., *J. Colloid Interface Sci.*, **26**, 62 (1968)

[67] Blaaderen, A. v., Vrij, A., *J. Colloid Interface Sci.*, **156**, 1-18 (1993)

[68] Baumann, F., Deubzer, B., Geck, M., Dauth, J., Schimidt, M., *Macromolecules*, **30**, 7568 (1997)

[69] Lindenblatt, G., Schärtl, W., Pakula, T., Schmidt, M., *Macromolecules*, **33**, 9340 (2000)

[70] Roos, C., Schmidt, M., Ebenhoch, J., Baumann, F., Deubzer, B., Weis, J., *Adv. Mater.*, **11**, 761 (1999)

[71] Schmidt, M., Emmerich, O., Roos, C., Fischer, K., Baumann, F. Deubzer,B., Weis, J., ""Molecular Reactors Based on Organosilicon µ-Networks"" (p726), in "Organosilicon Chemistry: From Molecules to Materials", ed., N. Auner, Weis, J., Wiley-VCH, Weinheim (2000)

[72] Emmerich, O., Hugenberg, N., Schmidt, M., Sheiko, S. S., Baumann, F., Deubzer, B., Weis, J., Ebenhoch, J., *Adv.Mater.*, **11**, 1299 (1999)

[73] Zheng, Y., Andreopoulos, F., Micic, M., Huo, Q., Pham, S., Lebanc, R., *Adv.Funct.Mater.*, **11**, 37 (2001)

[74] Meakin, P., *Phys. Rev. Lett.*, **51**, 1119 (1983)

[75] Kolb, M., Botet, R., Jullien, R., *Phys. Rev. Lett.*, **51**, 1123 (1983)

[76] Gardner, K. H. T., T.L., Young, T.C., *Coll.Surf.A Phys.Eng.*, **141**, 237 (1998)

[77] Ihara, T., Kurohara, K., Jyo, A., *Chem.Lett.*, **10**, 1041 (1999)

[78] Chen, Y., Geh, J.L., *Polymer*, **37**, 4481 (1996)

[79] Imai, Y., Naka, K., Chujo, Y., *Polym.J.*, **30**, 990 (1998)

[80] Chen, Y., Tsai, C.H., *J.Appl.Polym.Sci.*, **70**, 605 (**1998**)

[81] Chujo, Y., Sada, K., Saegusa, T., *Macromolecules*, **23**, 2693 (**1990**)

[82] Mccullough, J. J., *Chem. Rev.*, **87**, 811 (1987)

[83] Tokumaru, K., Coyle, J. D., *Pure & Appl. Chem.*, **64**, 1343 (1992)

[84]   Mustafa, A., *Chem. Rev.*, **52**, 1 (1952)

[85]   Herndon, W. C., *Chem. Rev.*, **72**, 157 (1972)

[86]   Fritzsche, J. J., *Prakt. Chem.*, **101**, 337 (1867)

[87]   Fritzsche, J. J., *(Z) Angew. Chemie*, **10**, 290 (1867)

[88]   Linebarger, C. E., *Am. Chem. J.*, **17**, 616 (1895)

[89]   Woodward R. B., H., R., "The Conservation of Orbital Symmetry", Verlag Chemie, Weinheim (1970)

[90]   Turro, N. J., "Modern Molecular Photochemistry", Benjamin/Cummings, Menio Park (1978)

[91]   Penn, J. H., Cox, E. D., *Pure & Appl. Chem.*, **64**, 1367 (1992)

[92]   Schreiber, S. L., *Science*, **227**, 857 (1985)

[93]   Hammond, G. S., Stout, C. A., Lamola. A. A., *J. Am. Chem. Soc.*, **86**, 3103 (1964)

[94]   Mizuno, K., Murakami, K., Kaizama, N., Ostuji, Y. J., *J. Chem. Soc., chemi. commun.*, 462 (1983)

[95]   Muthuramu, K., Ramamurthy, V., *J. Org. Chem.*, **47**, 3976 (1982)

[96]   Nikolova, R. D., Vayssilov, G. N., Rodios, N., Bojilova, A., *Molecules*, **7**, 420 (2000)

[97]   Murray, R. D. H., Mendez, J., Brown, S. A., "The Natural Coumarins: Occurrence, Chemistry and Biochemistry", John Wiley & sons, New York (1982)

[98]   Ciamician, G., Silber, P., *Ber. Dtsch. chem. Ges. Berlin*, **35**, 4128 (1902)

[99]   Nakayama, Y., Matsuda, T., *J. Polym. Sci., Part A: Polym. Chem.*, **31**, 977 (1993)

[100] Nakayama, Y., Matsuda, T., *J. Polym. Sci., Part A: Polym. Chem.*, **50**, 2451 (1992)

[101] Reiser, A., "Photoreactive Polymers", Wiley, New York (1989)

[102] Lewis, F. D., Quillen, S. L., Hale, P. D., Oxman, J. D., *J. Am. Chem. Soc.*, **110**, 1261 (1988)

[103] Lewis, F. D., Oxman, J. D., Gibson, L. L., Hampsch, H. L., Quillen, S. J., *J. Am. Chem. Soc.*, **108**, 3005 (1986)

[104] Tanaka, H., Tsuda, M., *US Patent 3767415*, (1973)

[105] Bantle, S., Schmidt, M., Burchart, W., *Macromolecules*, **15**, 1604 (1982)

[106] Jungmann, N., Schmidt, M., Maskos, M., *Macromolecules*, **34**, 8347 (2001)

[107] Blanchard, C. R., *The Chemical Educator*, **1**, 1-8 (1996)

[108] Mal, N., Fujiwara, M. and Tanaka, Y., *Nature*, **421**, 350 (2003)

[109] Hino, T., Shimabayashi, S., Tanaka, M., Nakano, M. and Okochi, H., *Journal of Microencapsulation*, **18**, 19-28 (2001)

[110] Thomas, J. A., Seton, L., Davey, R. J. and DeWolf, C. E., *Chemical Communications*, 1072-1073 (2002)

[111] Kiyoyama, S., Shiomori, K., Kawano, Y. and Hatate, Y., *Journal of Microencapsulation*, **20**, 497-508 (2003)

[112] Hettler, D., Andry, M. C. and Levy, M. C., *Journal of Microencapsulation*, **11**, 213-224 (1994)

[113] Parthasarathy, R. V. and Martin, C. R., *Nature*, **369**, 298-301 (1994)

[114] Parthasarathy, R. V. and Martin, C. R., *Journal of Applied Polymer Science*, **62**, 875-886 (1996)

[115] Bachtsi, A. R. and Kiparissides, C., *Journal of Controlled Release*, **38**, 49-58 (1996)

[116] Aiedeh, K., Gianasi, E., Orienti, I. and Zecchi, V., *Journal of Microencapsulation*, **14**, 567-576 (1997)

[117] Duarte, M. G., Brunnel, D., Gil, M. H. and Schacht, E., *Journal of Materials Science-Materials in Medicine*, **8**, 321-323 (1997)

[118] Esen, C., Kaiser, T., Borchers, M. A. and Schweiger, G., *Colloid and Polymer Science*, **275**, 131-137 (1997)

[119] Frere, W., Danicher, L. and Gramain, P., *European Polymer Journal*, **34**, 193-199 (1998)

[120] Danicher, L., Frere, Y. and Le Calve, A., *Macromolecular Symposia*, **151**, 387-392 (2000)

[121] Yeom, C. K., Oh, S. B., Rhim, J. W. and Lee, J. M., *Journal of Applied Polymer Science*, **78**, 1645-1655 (2000)

[122] Putlitz, B. Z., Landfester, K., Fischer, H. and Antonietti, M., *Advanced Materials*, **13**, 500-+ (2001)

[123] Chu, L. Y., Park, S. H., Yamaguchi, T. and Nakao, S., *Langmuir*, **18**, 1856-1864 (2002)

[124] Holl, R. J. and Chambers, R. P., *Journal of Microencapsulation*, **19**, 699-724 (2002)

[125] Radtchenko, I. L., Giersig, M. and Sukhorukov, G. B., *Langmuir*, **18**, 8204-8208 (2002)

[126] Glinel, K., Sukhorukov, G. B., Mohwald, H., Khrenov, V. and Tauer, K., *Macromolecular Chemistry and Physics*, **204**, 1784-1790 (2003)

[127] Yuan, X., Fischer, K. and Schärtl, W., *Adv.Funct.Mater.*, **14**, 457-463 (2004)

[128] Seifriz, W., *J. Phys. Chem.*, **29**, 738 (1925)

[129] Matsumoto, S., *ACS symposium series*, **26**, 415-436 (1985)

[130] Florence, A. t., Whitehill, D., *ACS symposium series*, **23**, 359 (1985)

[131] Edris, A., Bergnstahl, B. N, *Nahrung/Food*, **45**, 133 (2001)

[132] Dokic, P., Sherman, P., *Coll. Polym. Sci.*, **258**, 1159 (1980)

[133] Matsumoto, S., Makino. H. Ueno, Y., *J. Japan Oil Chem. Soc.*, **87**, 320 (1987)

[134] Kim, J. W., Ko, J. Y., Jun. J. B., Chang, I. S., Kang, H. H., Suh, K. D., *Colloid and Polymer Science*, **281**, 157 (2003)

[135] Ma, G.-H., Sone, H., Omi, S., *Macromolecules*, **37**, 2954 (2004)

[136] Xie, R., Kolb, U., Li, J., Basche, T., Mews, A., *J. Am. Chem. Soc.*, **127**, 7480 (2005)

[137] Mokari, T., Banin, U., *Chem. Mater.*, **15**, 3955 (2003)

[138] Dabbousi, B. O., Rodriguez-Viejo, J., Mikulec, F. V., Heine, J. R., Mattoussi, H., Ober, R., Jensen, K. F., Bawendi, M. G., *J. Phys. Chem. B.*, **101**, 9463 (1997)

[139] Yuan, X., Fischer, K., Schärtl, W., *Adv.Funct.Mater.*, **14**, 457-463 (2004)

[140] Vladisavljevic, G. T. and Schubert, H., *Journal of Dispersion Science and Technology*, **24**, 811-819 (2003)

[141] Chu, L. Y., Xie, R., Zhu, J. H., Chen, W. M., Yamaguchi, T. and Nakao, S., *Journal of Colloid and Interface Science*, **265**, 187-196 (2003)

[142] Yasuno, M., Nakajima, M., Iwamoto, S., Maruyama, T., Sugiura, S., Kobayashi, I., Shono, A. and Satoh, K., *Journal of Membrane Science*, **210**, 29-37 (2002)

[143] Yamazaki, N., Yuyama, H., Nagai, M., Ma, G. H. and Omi, S., *Journal of Dispersion Science and Technology*, **23**, 279-292 (2002)

[144] Sugiura, S., Nakajima, M., Itou, H. and Seki, M., *Macromolecular Rapid Communications*, **22**, 773-778 (2001)

[145] Omi, S., Senba, T., Nagai, M. and Ma, G. H., *Journal of Applied Polymer Science*, **79**, 2200-2220 (2001)

[146] Omi, S., Katami, K., Taguchi, T., Kaneko, K. and Iso, M., *Macromolecular Symposia*, **92**, 309-320 (1995)

[147] Omi, S., Katami, K., Yamamoto, A. and Iso, M., *Journal of Applied Polymer Science*, **51**, 1-11 (1994)

[148] Baumann, F., Deubzer, B., Geck, M., Dauth, J., Sheiko, S. and Schimidt, M., *Adv.Mater.*, **12**, 955 (1997)

[149] Graf, C., Schärtl, W., Fischer, K., Hugenberg, N. and Schmidt, M., *Langmuir*, **15**, 6170 (1999)

[150] Graf, C., Schaertl, W. and Hugenberg, N., *Adv.Mater.*, **12**, 1353 (2000)

[151] Uhrich, K. E., Cannizzaro, S. M., Langer, R. S., Shakesheff, K. M., *Chem. Rev.*, **99**, 3181 (1999)

[152] Ehtzazi, T., Washington, C., *J. of Controlled Release*, **68**, 361 (2000)

[153] Pedley, D. G., Skelly, P. J., Tighe, B. J., *Br. Polym. J.*, **12**, 99 (1980)

[154] Ratner, B. D., Hoffmann, A. S., "Synthetic Hydrogels for Biomedical Applications, Ch. 1" (p1-35), in "Hydrogels for Medical and Related Applications", ed., ACS Sympo. Ser.(31), (1976)

[155] Davis, S., *Chemistry and Industry*, **3**, 683 (1981)

[156] Engel, R. S., Riggi, S., Fahrenbach, J., *Nature*, **219**, 856 (1968)

[157] Mahanand, D., Houck, J. C., *Clin.Chem*, **14**, 6 (1968)

[158] White, C. E., Weissler, A., *Anal. Chem.*, **42**, 57R-76r (1970)

[159] Harada, A., Furue, M., Nozakura, S., *Macromolecules*, **10**, 676-681 (1977)

[160] Kalyanasundaram, K., "Photochemistry in Microheterogeneous Systems", Academic Press, Inc., London (1987)

[161] Bender, M. L., Komiyama, M., "Cyclodextrin Chemistry" in "React. Struct. Concepts Org. Chem." ed., Vol. 16, Springer-Verlag, Berlin and New York (1978)

[162] Wang, J. L., Edelman, G. M., *J. Biol. Chem.*, **246**, 1185 (1971)

[163] Stryer, L., *Science*, **171**, 799 (1971)

[164] Cramer, F., Saenger, W., Spatz, H. C., *J. Am. Chem. Soc.*, **89**, 14 (1967)

[165] Seliskar, C. J., Brand, L., *J. Am. Chem. Soc.*, **93**, 5405 (1971)

[166] Nithipatikom, K. and McGown, L. B., *Anal.Chem.*, **58**, 3145 (1986)

[167] Trkula, M. and Keller, R. A., *Anal.Chem.*, **57**, 1663 (1985)

[168] Sau, S., Solanki, B., Orprecio, R., Van Stam, J. and Evans, C. H., *Journal of Inclusion Phenomena and Macrocyclic Chemistry*, **48**, 173-180 (2004)

[169] Matsumoto, S., *ACS symposium series*, **27**, 415 (1985)